Laboratory study on the efficiency of water injection dredging

An analysis on the influence of different dredge settings on the density current and production rate.

S.J.S. Ma

Delft University of Technology

TU Delft Port of Rotterdam Deltares

Laboratory study on the efficiency of water injection dredging

An analysis on the influence of different dredge settings on the density current and production rate.

by

S.J.S. Ma

to obtain the degree of Master of Science
at the Delft University of Technology,
to be defended publicly on Monday June 20, 2022 at 2:00 PM.

Student number:	4455193	
Project duration:	January 25, 2021 – June 20, 2022	
Thesis committee:	Prof. dr. ir. C. van Rhee,	TU Delft, chair
	Dr. ir. A. M. Talmon,	TU Delft/Deltares, supervisor
	Dr. ir. L. de Wit,	Deltares
	Dr. A. Kirichek,	TU Delft
	Dr. C. Chassagne,	TU Delft
Company supervisors:	E. Hupkes	Port of Rotterdam
	Ir. J. Smits	Port of Rotterdam

Cover: WID vessel Airset opperating in the Calandkanaal by Sebastiaan Ma.

An electronic version of this thesis is available at http://repository.tudelft.nl/.

TU Delft Port of Rotterdam Deltares

Preface

Before you lies my master thesis on ”Laboratory study on the efficiency of water injection dredging”, which performs an analysis of experimental data to optimize the production of port mud. It has been written as the final step to finishing my master's Civil Engineering at the TU Delft. The project was undertaken at the request of the Port of Rotterdam since they want to apply water injection dredging over a large area of the port. Furthermore, this is complementary research within the PRISMA programme.

I would like to thank my supervisors for their excellent guidance and support during this process. I enjoyed the fruitful discussions and was happy to be able to be open to them about my ideas. I would also like to thank the staff of Deltares for their contribution during the execution of the experiments. Their creative solutions to the practical problems we faced definitely contributed to the quality of this study. Furthermore, I would like to express my gratitude towards the Port of Rotterdam for providing me with this opportunity and I hope that my report will contribute to the ongoing challenges of keeping the port globally attractive.

Finally, I would like to thank all my friends and family for their love and support during the whole of my time in Delft. Without them, I would not have been able to achieve the milestones seen today.

Sebastiaan Ma
Delft, June 2022

Abstract

The Port of Rotterdam experiences large amounts of siltation from the upstream rivers in its basins and canals every year. Furthermore, container vessels increase in size every decade and therefore require a larger navigational depth. These two factors cause the yearly amount of dredged material to increase. Currently, mainly trailing suction hopper dredgers are used to remove the large amounts of sediment, but these vessels come with high costs and operational time. A more time and cost-efficient dredging method is therefore desired.

A potential solution to the increasing problems of costs and operational time by dredgers is the technique of water injection dredging. To make this technique as efficient and effective as possible, this thesis has the objective to measure and analyze flow and sediment properties for different parameter settings of water injection dredging and find the optimal parameter settings of this dredging technique on mud from the Port of Rotterdam. Large scale experiments have been conducted in the water-soil flume of Deltares, where a jetbar was trailed (or *run*) over a bed 27 meters long and 0.5 meters deep of port mud while injecting it multiple times with water. The traverse velocity, nozzle pressure, nozzle diameter, and stand-off distance (SOD) were varied. The created density current flowed towards a measuring frame where the flow velocity and density at different heights were measured in time. This results in flow velocity and density profiles of the density current. The intrusion depth by the jets, the jet settings, density of the current behind the jetbar, and the rheology of the mud were measured as well. Through this data, the production rate and behaviour of the density current are determined and described as a function of the jet settings.

A positive correlation is observed between the production rate and jet momentum when considering the data of the intrusion depth and analyzed samples of the bed, together with the data of the measured jet settings. The production is related linearly with the jet momentum using the Vlasblom equation combined with a non-dimensionless empirical fitting parameter per run per traverse velocity.

What is remarkable from the disk measurements is that the intrusion depth produced by the jets increases with ascending runs while the jet parameter settings stay the same. The data shows that the difference between the mass flux by the density current and the mass flux stirred up by the jets when the sediment concentration of an undisturbed bed is assumed, increases between runs when an increased intrusion depth between those runs is observed as well. This indicates that the volume penetrated by the jets contains a smaller amount of sediment than was initially assumed, thus is disturbed by the previous run and is therefore decreased in strength. This decrease in strength results in a larger intrusion depth during the run itself in comparison to the previous run.

Furthermore, the analysis of the production rates shows that the density current transports more sediment when a high jet momentum is applied. The velocity and density measurements at the ramp present a super-critical density current for a jet momentum > 500 N/m ($Fr_2 > 1$). For a super-critical density current relatively more horizontal momentum at the ramp is measured as well.

Next to the jet momentum, the influence of the SOD of the jets is analyzed by comparing runs with a SOD to runs without a SOD but with similar remaining jetting parameter settings. When a SOD is applied, the jet pressure applied to the bed is outside the flow development region and therefore the jet pressure decreases with distance from the jet nozzle. The data shows that the mass of sediment stirred up by the jets, for a SOD of 300 mm, is lower in comparison to a SOD of 0 mm. The density current transports relatively more sediment, however, when a SOD of 300 mm is applied. This is attributed to the observation that sediment is stirred up higher in the water column and therefore has more time to settle, in combination with high flow velocities also measured at these higher positions in the water column and entrainment. So, if a large amount of sediment needs to be stirred up, and therefore a large intrusion depth is required, no SOD should be applied and when large horizontal transport by the density current is desired, a SOD outside the flow development region of the jets should be used.

Contents

Nomenclature

α_s	non-dimensionless empirical fitting parameter	s m^{-1}
$\alpha_{s,r}$	shape factor	–
β	angular slope of the bed	°
$\beta_{s,r}$	shape factor	–
$\dot{\gamma}$	shear rate	s^{-1}
η	viscosity	Pa s
η_∞	viscosity index at build-down (= Bingham plastic viscosity if n=1)	Pa s
η_a	apparent viscosity	Pa s
η_d	dynamic viscosity	Pa s
κ	Von Karman constant	0.41 –
λ	state of built up of links between flocs	–
λ_0	Kolmogorov micro-scale of turbulence	m
μ	contraction coefficient	–
Φ_s	volume fraction of solids	–
ρ_f	density of mud flocs	kg m^{-3}
ρ_m	mixture density	kg m^{-3}
ρ_s	density of sediment	kg m^{-3}
ρ_w	density of water	kg m^{-3}
ρ_{d1}	density of upper layer of density current	kg m^{-3}
ρ_{d2}	density of lower layer of density current	kg m^{-3}
σ	conductivity	S m^{-1}
σ_m	conductivity of a medium	S m^{-1}
σ_w	conductivity of water	S m^{-1}
τ_0	yield stress at complete build-up (λ = 1)	N m^{-2}
τ_∞	yield stress at complete build-down (λ = 0)	N m^{-2}
τ_B	Bingham yield stress	Pa
τ_b	bed shear stress	N m^{-2}
τ_f	flow point stress	N m^{-2}
τ_i	shear stress at interface	N m^{-2}
τ_m	critical shear stress for mass erosion	N m^{-2}
τ_y	yield stress	N m^{-2}
τ_{cr}	apparent critical shear stress for erosion of a floc	N m^{-2}
ε	turbulent dissipation rate per unit mass	J kg^{-1}
ζ	relative elevation above the bed	–
a	empirical coefficient	–
a_λ	empirical constants	–
b	empirical coefficient	–
b_λ	empirical constants	–
c_m	mass concentration of sediment	kg m^{-3}
c_s	speed of sound in water	m s^{-1}
c_u	undrained shear strength	Pa
c_v	volumetric concentration of sediment	–
c_{dil}	diluted mass concentration of sediment	kg m^{-3}

c_{fm}	mass concentration of fluid mud layer	kg m^{-3}
c_{init}	initial mass concentration of sediment	kg m^{-3}
D_f	floc size	m
D_n	nozzle diameter	m
D_p	size of primary particles	m
d_w	water depth	m
d_{cr}	depth when the flow of the lower region is critical (Fr = 1)	m
d_{d1}	height of upper layer of density current	m
d_{d2}	height of lower layer of density current	m
$d_{eq,lam}$	the equilibrium depth for a laminar flow	m
$d_{eq,turb}$	the equilibrium depth for a turbulent flow	m
d_{init}	initial thickness of the mud bed	m
D_{max}	maximum diameter	m
E	rate of erosion	kg m^{-2} s^{-1}
e	efficiency coefficient	–
f_b	bottom fraction factor	–
f_i	interface fraction factor	–
Fr	Froude number	–
Fr_2	densimetric Froude number	–
Fr_i	internal Froude number	–
G	turbulent shear rate parameter	s^{-1}
g	gravitational acceleration	9.81 m s^{-2}
g'	buoyancyreduced gravitational acceleration	m s^{-2}
h_2	height of u_2 with respect to the bottom	m
h_{fm}	height of fluid mud layer	m
h_{ramp}	height of the ramp	m
I	current	A
I_j	jet momentum per meter width	N m^{-1}
$I_{j,t}$	total momentum of the jetbar	N
I_{ramp}	momentum at the ramp per meter width	N m^{-1}
k_1	entrainment coefficient	–
k_2	entrainment coefficient	–
L	characteristic length scale	m
m	empirical exponent	–
M_s	mass flux of eroded sediment	kg s^{-1}
N	number of primary particles	–
n	number of nozzles	–
n_f	fractal dimension of mud flocs	–
P_a	actual production	kg s^{-1}
P_i	initial production	kg s^{-1}
p_j	jet nozzle pressure	bar
p_{intr}	jet pressure at intrusion depth	bar
Q_j	jet discharge	m^3 s^{-1}
q_j	jet discharge	m^2 s^{-1}
Q_t	total discharge	m^3 s^{-1}
r	radial distance from the centre line of a nozzle	m
Re_p	Reynolds number of a particle	–
Ri	Richardson number	–

S	slope of the bed	m
s	distance from the nozzle	m
s_j	distance between the jets	m
s_s	salinity	‰
$s_{av,intr}$	average representative intrusion depth	m
s_{intr}	intrusion depth	m
SOD_b	Stand-off distance relative to level of the bed	mm
SOD_r	Stand-off distance relative to crest level of the ramp	mm
T	temperature	°C
u'	turbulent velocity fluctuations	$m\,s^{-1}$
U	horizontal flow velocity	$m\,s^{-1}$
u_2	maximum velocity of the density current	$m\,s^{-1}$
u_j	jet flow velocity	$m\,s^{-1}$
u_*	shear velocity	$m\,s^{-1}$
u_{d1}	flow velocity of upper layer of density current	$m\,s^{-1}$
u_{d2}	flow velocity of lower layer of density current	$m\,s^{-1}$
$u_{s,r}$	flow velocity in axial direction of a nozzle	$m\,s^{-1}$
V	voltage	V
v	kinematic viscosity	$m^2\,s^{-1}$
V_A	ionic attractive force	N
V_R	ionic repelling force	N
V_r	sum of the attractive and repelling force	N
v_t	traverse velocity	$m\,s^{-1}$
V_{intr}	intruded volume	m^3
W	vertical flow velocity	$m\,s^{-1}$
w	width of the flume	m
w_s	actual settling velocity of a floc	$m\,s^{-1}$
w_t	terminal settling velocity of a floc	$m\,s^{-1}$
$w_{s,h}$	hindered settling velocity of a floc	$m\,s^{-1}$
$w_{s,r}$	reference settling velocity of a floc	$m\,s^{-1}$
ws_c	weight of a cup	g
ws_d	weight of cup filled with dried mud	g
ws_s	weight of a cup filled with wet mud	g
z	flow index	–

1 | Introduction

This chapter provides a brief introduction to the study conducted for this thesis. The introduction consists of the problem definition (1.1), objective (1.2) and relevancy (1.3) of the study.

1.1. Problem definition

The Port of Rotterdam is one of the largest ports in the world and experiences large amounts of siltation every year. Silt is brought downstream by the rivers Rhine and Meuse and settles near the mouth of the river, which is also where the Port of Rotterdam is situated, because of reduced hydrodynamic conditions. From the west side of the port sand and marine silts are transported from the southern part of the North Sea. The silt deposits on the bottom and results in a decrease in navigational depth.

To keep the port attractive for shipowners of large vessels the minimum required navigation depth needs to be maintained and thus millions of cubes of silt need to be dredged every year, as illustrated in Figure 1.1. The yearly volumes to be dredged have increased over the last couple of years. As vessels keep growing in size every decade the volume of dredged material therefore grows as well (Baird (2002); Sánchez et al. (2020)). Ports all over the world are trying to find more cost-effective solutions to this problem.

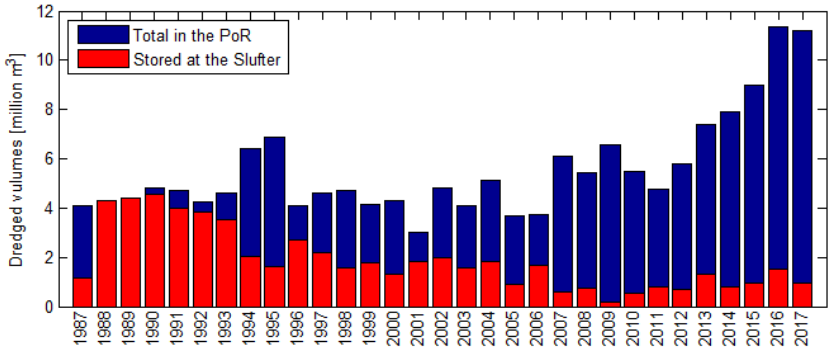

Figure 1.1: Yearly dredged volumes of sediment from the channels from the Port of Rotterdam (Kirichek et al., 2018).

The port basins are regularly dredged by the Port of Rotterdam. The main waterways to enter these basins are dredged by Rijkswaterstaat, which is the Directorate-General for Public Works and Water Management in The Netherlands. Over the last decades, maintenance dredging was mainly, and still is, carried out by Trailing Suction Hopper Dredgers (TSHD) and partly by Bed Levelers and Grab Dredgers. For example, in 2017 these types of vessels contributed each 80%, 5%, and 14% respectively (Kirichek et al., 2018). The remaining 1% was debris removal.

TSHDs pump the material from the bed into the hopper, sail to a dumping location and dump the material through its bottom doors. It then has to sail back to the location to be dredged and repeat this process. Because the dredged material cannot immediately be disposed of, operational times are high. This causes hindrances to other vessels in the basins and waterways and high costs since a large part of the costs consist of daily wages per vessel. An alternative dredging technique in terms of operational times and costs is therefore desirable.

1.2. Objective

This thesis is part of the PRogramm Innovative Sediment MAnagement (PRISMA) project, which aims to optimize dredging operations and better characterization of different types of sediment. The PRISMA project is a collaboration between TU Delft, Deltares, MARIN, Port of Rotterdam and Port of Hamburg. As part of PRISMA, this thesis performs an optimization study on the parameter settings for water

injection dredging (WID) on mud originating from the Port of Rotterdam. Experiments for different parameter settings of WID are conducted in the water-soil flume at Deltares. The density currents and production rates created during these experiments are measured and analyzed. From this analysis, an optimal set of parameters for WID operations is recommended at the end.

Objectives

This thesis contains two objectives:

- **Measure and analyze flow and sediment properties during the experiments in the water-soil flume for different parameter settings of water injection dredging.**

  For this goal the following properties are measured:

  - Bi-directional flow profile (U, W).
  - Suspended sediment concentration profile.
  - Bathymetry before and after runs over the whole length of the flume.
  - Rheological properties of the bed before the start of the experiments.

- **Find the optimal parameter settings of water injection dredging to maximize production.**

  The parameters of the WID process which are varied during the experiments:

  - Traverse velocity (v_t)
  - Jet nozzle pressure (p_j)
  - Nozzle diameter (D_n)
  - Stand-off distance (SOD)

Additional research question

From the Port of Rotterdam an additional question is which are of interest are added to this study:

- What is the influence of the SOD on the behaviour of the density current and the production rate?

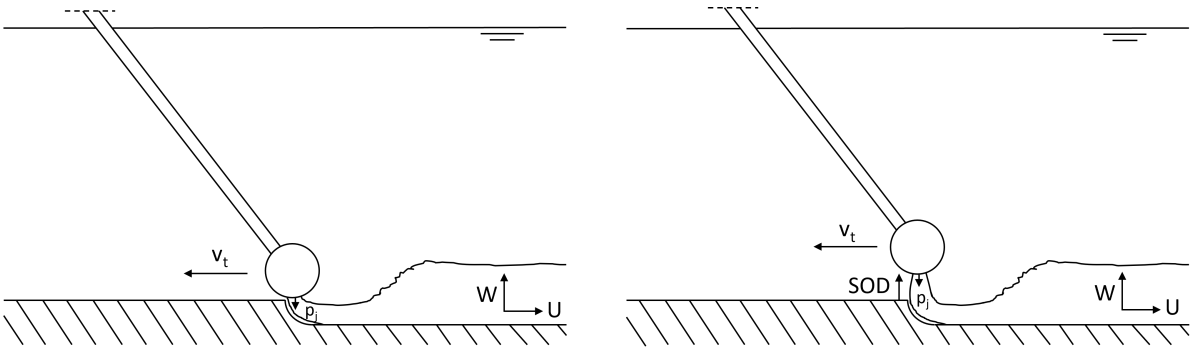

Figure 1.2: Schematization of WID with and without a SOD (right and left respectively).

1.3. Relevancy

The application of WID has been widely used and investigated for the last 30 years and there is already a lot of experience with this method within many different dredging companies (Wilson, 2007). Despite this, the influence of different WID parameters on the rate of erosion of cohesive sediments is still poorly understood and no general theory on an optimal set of parameters can be found in the literature. Comparable studies like Kortmann (1994), Swart (2015), Verhagen (2000) and van Rijn (n.d.) only give rough estimates of jet penetration and height of density currents or contain censored information on these subjects.

Computational models like Jet3D, TUDflow3D, and 2 Layer Fluid Mud Models can be used to model the behaviour of turbidity currents but need to be provided and verified with data. These models only give partially fair representations of reality because simplifications are embedded in them.

2 | Water injection dredging

Chapters 2 to 4 provide background information for those who are unfamiliar with the concept of WID. Chapter 2 explains and elaborates on the principle of WID and its variable parameters. Chapter 3 describes cohesive sediments from the marine environment, particularly the one to which the process of WID is applied during this study. Chapter 4 treats the specific form of cohesive sediment caused by WID, which is fluid mud transported as a density current.

2.1. General description

During the process of WID, water is injected under low pressure into the soil. The water is pumped through vertical jets lined up in a horizontal bar, also called a jetbar. The injected water fluidizes the soil into suspension and creates a fluid mud layer near the bed with a higher density of the water on top (PIANC, 2013). The difference in density between the fluid mud and water on top under the influence of gravity or a dynamic environment caused by waves or a tide, causes the mud to flow as a density current.

WID causes several processes after penetration of the jets into the soil. Kortmann (1994) identified three sub-processes that are caused after jetting. After penetration of the jets, the soil is loosened and becomes highly turbulent. It runs off at high speed in a very small layer as a super-critical flow, which only occurs for a small distance. The second process is whirling up in a hydraulic jump during which water from the upper layer is entrained in the suspended flow and the volume of the density current increases. At the same time, the flow velocity decreases, and the flow transforms toward a sub-critical state. After whirling up, the density current flows as a run-off towards deeper areas in the bathymetry, i.e. down the slope. These processes are schematized in Figure 2.1. The concept of a density current is further explained in Section 4.3.

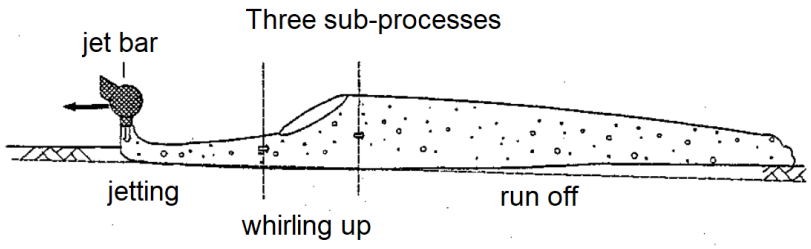

Figure 2.1: The different sub-processes during WID (Kortmann, 1994).

2.2. Production rate

The production of WID is defined as the amount of dry mass removed per unit of time (in kg/s) and is calculated as

$$\text{production} = s_{intr} \cdot v_t \cdot c_m \cdot w \tag{2.1}$$

with s_{intr} the intrusion depth, c_m the concentration of sediment and w the width of the jetbar. To predict the production of WID a proper theory can not be found in the literature. Several studies (Schuurman (1997); Schulting (1998); Kortmann (1994)) looked at methods to determine s_{intr} of WID vessels. Unfortunately, these formulas are censored for confidentiality reasons. The formulas were specifically derived from data of the WID vessel Jetsed.

Though no satisfactory method for determining the production can be found, an approximation can

be made with a mass balance. Verhagen (2000) provides a simple set of equations for the process of intrusion of water jets into mud and run-off of fluid mud. The combination consists of a production relation (2.2), velocity of the density current (2.3) and a continuity equation (2.4):

$$q_j = h_{fm}\,(U + v_t) - s_{intr} v_t \tag{2.2}$$

$$U = \alpha \sqrt{g \frac{\Delta\rho}{\rho_w} h_{fm}} \tag{2.3}$$

$$s_{intr} v_t c_m = h_{fm}\,(U + v_t)\, c_{fm} \tag{2.4}$$

The definitions of the parameters is visualized in Figure 2.2. The parameters are defined as:

α	[-]	=	correction factor for the friction (is in the order of 0.9)
$\Delta\rho$	[kg/m^3]	=	density difference between water and the fluid mud
q_j	[m^2/s]	=	discharge from jets per meter width
h_{fm}	[m]	=	height of the created fluid mud layer
U	[m/s]	=	horizontal flow velocity of the fluid mud layer
c_{fm}	[kg/m^3]	=	concentration of the fluid mud layer

To be able to make an approximation of the production, three relevant output parameters need to be chosen. Which parameters are known beforehand can be used as input.

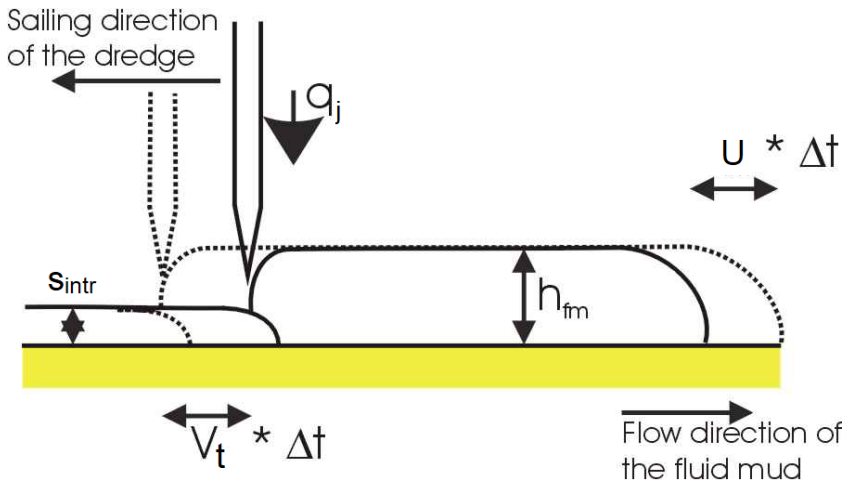

Figure 2.2: Adapted from Verhagen (2000)

Using this approach, a rough estimation can be made of the production of different sets of parameters. This set of equations contains the following simplifications: the concentration of the bed and fluid mud layer is homogeneous, the situation is 2D and assumes no variations in the third dimension, and the discharge of the jet in combination with the intrusion depth is known. A (simple) relationship between discharge from the jet and intrusion depth in mud is needed. A formula for s_{intr} of a single jet was derived by Swart (2015):

$$s_{intr} = \sqrt{\frac{3\rho u_j^2 D_n^2}{c_u}} \tag{2.5}$$

u_j is the outflow velocity of the jet, c_u is the undrained shear strength of the soil, and D_n is the nozzle diameter. In the derivation of this equation, it is assumed that the jet intrudes into the soil up to a depth where the thrust pressure is equal to about 6 times the cohesion of the soil as is explained in Section 3.4.2 as a criterion for mass erosion.

2.3. Operational parameters and fluid mud conditions

In this section, the conditions and some typical values of the parameters of WID are given from literature. These details are given to the reader to get a feeling of the conditions during normal WID operations in the field and to show the resemblance with the experiments.

Fluid mud concentration

In general, a density current can be divided into an upper turbulent layer with a concentration in the range of 10 - 100 kg/m^3 and a laminar (viscous) lower layer in the range of 100 - 300 kg/m^3. The structure of a density current is explained further in Section 4.3. According to van Rijn (n.d.), the concentration of fluid mud in the harbour basin of Hansweert along the Westerschelde Estuary, The Netherlands, can be in the range of 20 to 100 kg/m^3 when WID is applied. In the Haringvliet basin, the range is 25 to 120 kg/m^3.

Sigwald et al. (2015) gives an overview of suspended sediment concentrations at different sites. For the Elbe Estuary, 100 g/m^3 max was measured in the water column. At Bayonne, 32-190 g/m^3 at mid-depth and 32-580 g/m^3 at the bottom were measured. At the Ems Estuary, 500 g/m^3 at 2.50 m above the bottom was found and at Antwerp (Scheldt) a range of 30-1500 g/m^3 for a range in measured depth of -10 to -16 m from the surface at a distance of 5 to 40 meters from the dredger.

To sail through the mud the density may not exceed 1200 kg/m^3 ($\approx$ 300 g/m^3 concentration) (Kirichek et al., 2018). This was concluded based on full-scale experiments in the Port of Rotterdam, Bangkok, and Suriname. The depth at which this concentration is reached is defined as the nautical depth. It is expected that the density of the fluid mud after WID is lower than the density criteria, so the occurrence of a density current does not influence the nautical depth.

Traverse velocity

During WID operations the traverse velocity v_t is often in the range of 0.5 - 1.5 m/s (PIANC, 2013). v_t determines the intrusion depth and thus production. Assuming the discharge from the nozzle is constant, the higher v_t the smaller the intrusion depth. When a jet is in one place only for a short time, it has no time to develop and penetrate fully into the cohesive sediment. This was observed during the experiments of Schulting (1998) as well. In Figure 2.3 the volume of the run-off of the fluid mud during 4 runs is visualized (black bar). One can see that for low v_t the run-off, especially during the last run, is high. For higher values of v_t, the run-off is lower. Schulting also observed that, for a constant velocity, the run-off increased for mud with a lower cohesion (vertical graphs in the middle). The top graph is for mud with a high cohesion value and the lower graph is for mud with a lower cohesion value.

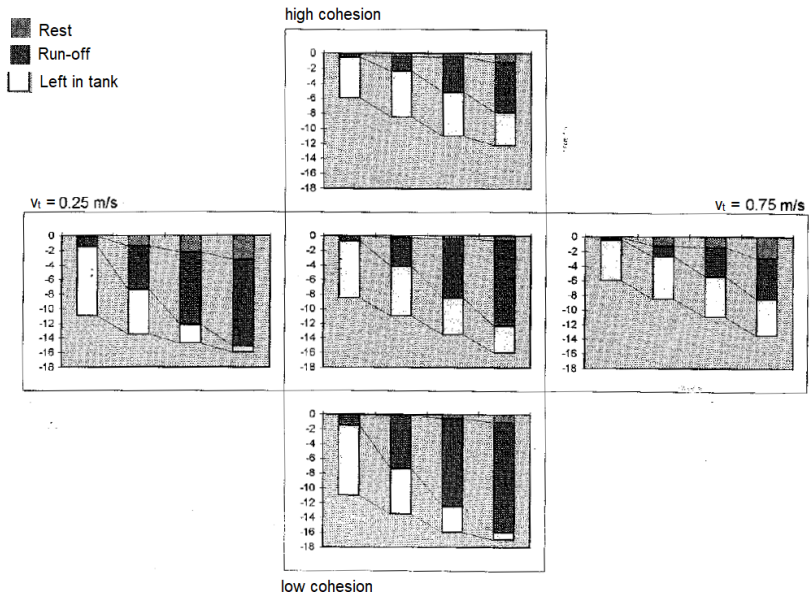

Figure 2.3: The production results from run-off experiments caused by WID. In every graph the left bar is the first run and right bar is the fourth run. Nozzle pressure for all tests was 0.8 bar. (Adapted from Schulting (1998)).

Nozzle pressure

The nozzle pressure p_j is given as relative pressure to the surrounding hydraulic pressure. During WID, large volumes of water are injected under low pressure: 1 - 1.5 bar (Sigwald et al., 2015). During the experiments of Schuurman (1997) three tests with p_j = 83.6 kPa (= 0.836 bar) were conducted. Schulting (1998) uses p_j = 0.8 and 1.4 bar. So the typical nozzle pressure lies around 1 bar.

Distance between nozzles

The distance between the nozzles s_j can influence the production of WID. If the nozzles are too far apart the cavity width of the jet will not be able to erode all the mud and leave so-called *lanes* in the bathymetry. For sand, it is known that ideally, the cavity width should be equal to s_j (Miedema, 2019). The literature does not provide any information on clay or silt. No (experimental) research on s_j for clay or mud could be found.

Schulting (1998) discusses briefly the plane jet theory (*vlakke straaltheorie*). It is the understanding of the author that s_j should be chosen as such that at a penetration depth of $p_{stag} = 6c_u$ (Section 3.4) the jets should create a flat plane. The width of the flat plane is 0.8 times the diameter of the jet. Where this number originates from is not explained. Because c_u depends on the rheology of the mud, s_j thus varies for different types of mud.

From analyzing photos of WID vessels in the field it was observed that s_j can vary from 20 to 40 cm. For WID vessel Jetsed s_j is approximately 35 cm with D_j = 90 mm. Unfortunately, most companies that possess WID vessels do not publish information regarding their vessels publicly.

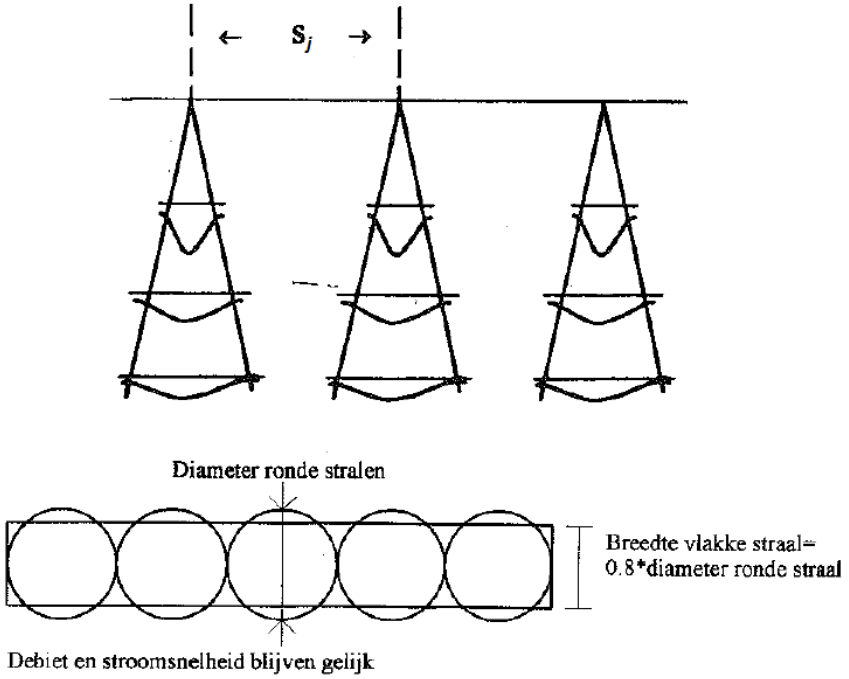

Figure 2.4: Schematization of jet dispersion (top) and top view of the plane jet where the dispersion of the jets meet (bottom) (Adapted from Schulting (1998)).

3 | Cohesive sediment characteristics

The material used for this study concerns the bed of a port. Therefore, this chapter solely describes the characteristics of cohesive sediment from the marine environment.

3.1. Composition

As is often found in the marine environment, cohesive sediment, in general, is a mixture of clay, silt, sand, organic material, water and sometimes gas (Winterwerp & Van Kesteren, 2004). The ratio between these different components defines, among other things, the behaviour and variability in time and space. The cohesive behaviour of the sediment is mainly determined by the clay particles and organic material, in relation to the chemical properties of the liquid phase. An example of a typical particle size distribution of port mud is given in Figure 3.1. This mud originates from the Port of IJmuiden in The Netherlands. This figure shows that the largest part of mud from a port consists of silt and clay.

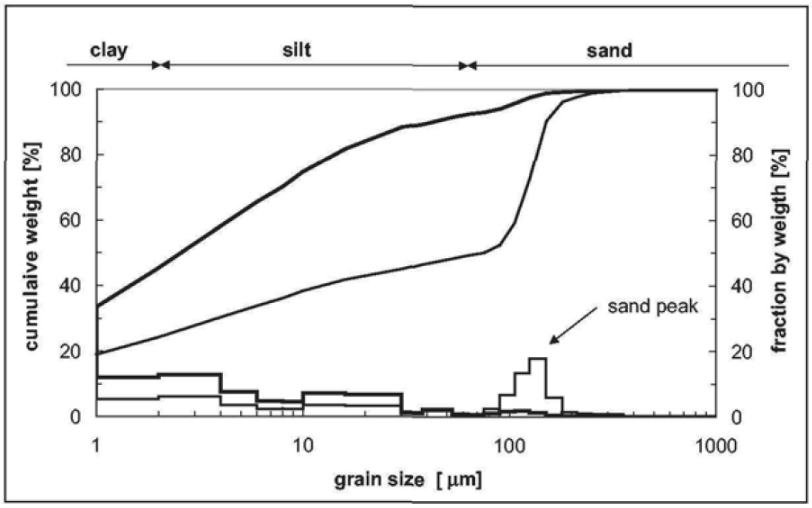

Figure 3.1: Particle size distribution of port mud from the Port of IJmuiden in The Netherlands (Van Kesteren, 2004). The thick line corresponds to the cumulative weight and the thin line to the fraction by weight.

3.2. Cohesion

Cohesion is the soil strength that depends on interparticle friction. To erode cohesive sediment, shear stresses need to be applied which are larger than the cohesion. As is further explained in Section 3.4, cohesion is an important property of the sediment to understand the erosive behaviour.
As the process of WID causes high deformation rates, it is assumed that the failure of the mud is an undrained process. Therefore, the undrained shear strength c_u is an important parameter. According to PIANC (2013), silt which is typically encountered in maintenance dredging projects has a shear strength far below 5 kPa. Typical values of c_u for the Port of IJmuiden are in the range of 0.017 - 0.069 kPa and 0.022 - 0.154 kPa for Lake Ketel (Winterwerp & Van Kesteren, 2004).

3.3. Flocculation and settling velocity

The process of flocculation influences the settling velocity and is at the same time influenced by the salinity of the water and organic matter. At high-concentration conditions in seawater or with high organic matter content, flocculation is important and results in variations in floc size over the water depth. With this knowledge, the process and theories of the settling velocity of cohesive sediments of

the marine environment can be used to determine the deposition rate. Deposition within the fluid mud decreases the production of the WID process. Thus, one should know what causes the sediment to settle and how to minimize it.

According to Winterwerp & Van Kesteren (2004) almost all cohesive sediments in the marine environment are flocculated. When sediment is flocculated it has formed so-called flocs when the sediment is in contact with saline water. The flocs have a very open structure made of clay particles and have a high water content. The electric charge between the flocs characterizes the strength between flocs, which is further elaborated in Section 3.3.4.

Flocculation is governed by three processes: Brownian motion, particle size and turbulent motion. According to McCave (1984) and Van Leussen (1994) Brownian motion that causes aggregation is negligible in coastal environments and thus also for the situation simulated in this study. The particles in the Brownian range may coagulate fast after erosion but cannot hold an equilibrium position.

3.3.1. Turbulence

First, the contribution of turbulence to aggregation and break up of flocs and thus the influence on the settling velocity is assessed from the approach taken from the book of Winterwerp & Van Kesteren (2004). Van Leussen (1988) described the influence of turbulence on the settling velocity in the following way:

$$w_s = w_{s,r}\frac{1 + aG}{1 + bG^2} \tag{3.1}$$

with w_s and $w_{s,r}$ the actual and reference settling velocities, respectively. The settling velocity may vary due to flocculation and/or hindered settling effects. a and b are empirical coefficients and G is the turbulent shear rate parameter

$$G = \sqrt{\frac{\varepsilon}{v}} = \frac{v}{\lambda_0^2} \tag{3.2}$$

with ε the turbulent dissipation rate per unit mass, v the kinematic viscosity of the suspension, and λ_0 is the Kolmogorov micro-scale of turbulence: $\lambda_0 = (v/\varepsilon)^{1/4}$. What theory for ε should be used depends on the behaviour of the density current. If the turbulence is isotropic then

$$\varepsilon \approx 15v\left(\partial u'/\partial x\right)^2 \tag{3.3}$$

with u' the turbulent velocity fluctuation in downstream direction. Now G is a measure of the turbulent shear rate of the flow at the smallest turbulent length scales. If the turbulence is not isotropic then G is a function of the water depth $G(h)$. The formula of Nezu & Nakagawa (2017) applies in that case:

$$\varepsilon \approx \frac{u_*^3}{\kappa h}\frac{1 - \zeta}{\zeta} \tag{3.4}$$

with u_* is the shear velocity ($u_*^2 = \tau_{bed}/\rho$), κ the Von Karman constant, and $\zeta = z/h$ the relative elevation above the bed.

3.3.2. Particle size

Large flocs settle faster than small flocs and thus collide with small flocs, thereby enhancing flocculation. In general the settling velocity of sediment particles is governed by the size of the particle (in this case floc) D_f, the shape and the difference in density from the water $\Delta\rho_f$ (Winterwerp & Van Kesteren, 2004):

$$\Delta\rho_f = \rho_f - \rho_w = (\rho_s - \rho_w)\left[\frac{D_p}{D_f}\right]^{3-n_f} \tag{3.5}$$

ρ_f, ρ_w and ρ_s are the densities of the mud flocs, water and sediment respectively, and D_p is the diameter of the primary particles. n_f is the fractal dimension of mud flocs from the particle size distribution. n_f is defined as

$$n_f = \lim_{L \to \infty}\frac{\ln(N(L))}{\ln(L)} \tag{3.6}$$

with N the number of primary particles and L the length-scale of the particles. Particles of a larger size settle at a higher velocity than smaller particles. This is seen in the result of a balance between the gravitational and drag forces for a single floc in a homogeneous fluid for the settling velocity $w_{s,r}$:

$$w_{s,r} = \frac{\alpha_{s,r}}{18\beta_{s,r}} \frac{(\rho_s - \rho_w)\, g}{\eta_d} D_p^{3-n_f} \frac{D_f^{n_f-1}}{1 + 0.15 Re_f^{0.687}} \tag{3.7}$$

$\alpha_{s,r}$ and $\beta_{s,r}$ are shape factors, g is the gravitational acceleration, η_d is the dynamic viscosity and Re_p is the Reynolds number of the particle ($Re_p = w_{s,r} D_f / v$). Formula 3.7 can be simplified to the well-known Stokes' formula:

$$w_{s,r} = \frac{(\rho_s - \rho_w)\, g D_f^2}{18\eta_d} \tag{3.8}$$

In the Stokes' formula a spherical ($\alpha_{s,r}$ = $\beta_{s,r}$ = 1), Euclidean (n_f = 3) particle in the Stokes' regime is assumed for a very small Reynolds number (Re « 1).

In Figure 3.2 Winterwerp summarizes the data of different studies and experiments on the influence of particle size on the settling velocity. One can see a positive correlation with D_f which is in accordance with equation 3.8.

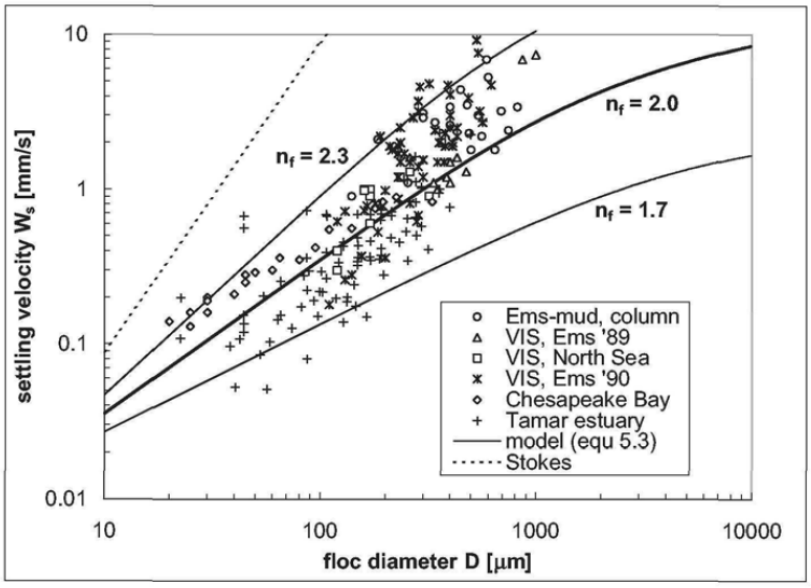

Figure 3.2: Relation between settling velocity and size of a floc (Winterwerp & Van Kesteren, 2004).

3.3.3. Hindered settling

The formulas mentioned in the sections before are only applicable for low concentrations i.e. where individual particles of the suspension do not influence each other during settling and thus are completely unaware of each other's existence. During the conditions of the experiments of this study, high sediment concentrations occur. Concentrations of the fluid mud up to 250 g/m^3 are not unusual for WID operations as is explained in section 2.3. Therefore hindered settling is important to take into account.

The formula of Richardson & Zaki (1954) is popular and widely used:

$$w_{s,h} = w_t\, (1 - C_v)^m \tag{3.9}$$

$w_{s,h}$ is the hindered settling velocity, C_v is the volumetric concentration in the cloud, w_t is the terminal settling velocity of the solid particle and m is the empirical exponent related to the particle Reynolds number Re_p = $w_t \cdot D_f / v_t$. The values of m are given in Table 3.1.

Re_p	m
$Re_p \leq 0.2$	4.6
$0.2 < Re_p < 1$	$4.4Re_p^{-0.03}$
$1 < Re_p < 500$	$4.4Re_p^{-0.1}$
$500 \leq Re_p$	2.4

Table 3.1: Value of m depending of Re_p for the Richardson & Zaki formula.

3.3.4. Salinity

Clay particles are mainly negatively charged. Depending on the number of positive ions present in the water, the clay particles attract or repel each other. The attractive force is due to Van der Waals bond interactions (V_A). The repulsive force (V_R) is due to the ion clouds around the particles of a similar charge. Depending on the number of positive ions in the cloud and the distance between the particles, the force is either attractive or repelling (see Figure 3.3).

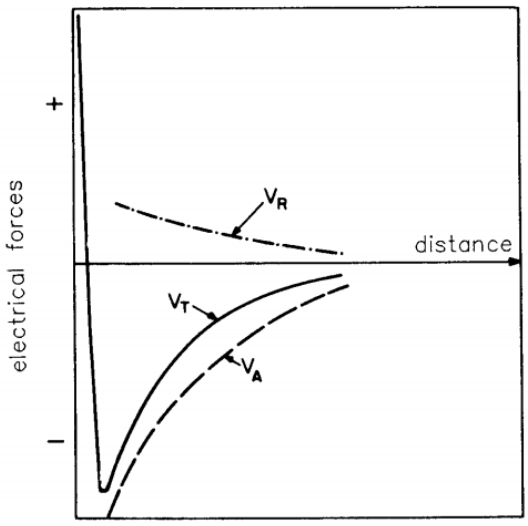

Figure 3.3: Attractive force (V_A), repelling force (V_R) and the sum of the two forces (V_r) as function of the distance between particles (Van Rijn, 1993).

Fresh water suspensions contain few positive ions, so their repulsive forces dominate. In salt water, the amount of positive sodium-ions dominates and thus the attractive forces between clay particles as well. This is caused by the positive ion cloud around the negative clay particles leading to enhanced floc formation.

Experimental research done by Owen (1970), Krone (1986) and Allersma et al. (1984) shows that salt has a significant effect on the settling velocity (Figure 3.4). Owen (1970) and Allersma et al. (1984) found for salt concentrations higher than 1000 ppm (= mg/L) the settling velocity of flocs increases almost linearly with salinity. Unfortunately, no general mathematical relations regarding the settling velocity over the salinity can be found in literature.

3.4. Erosion

The rate of erosion of the mud by the vertical jets determines the initial production of the process of WID. When water is jetted into the cohesive soil, the flow is highly turbulent and highly deformations the soil. This causes mass erosion. During run-off of the density current, shear stresses on the bed might be high enough for additional erosion of individual flocs. It is expected, however, not to contribute significantly to production (Kortmann, 1994) but is briefly mentioned.

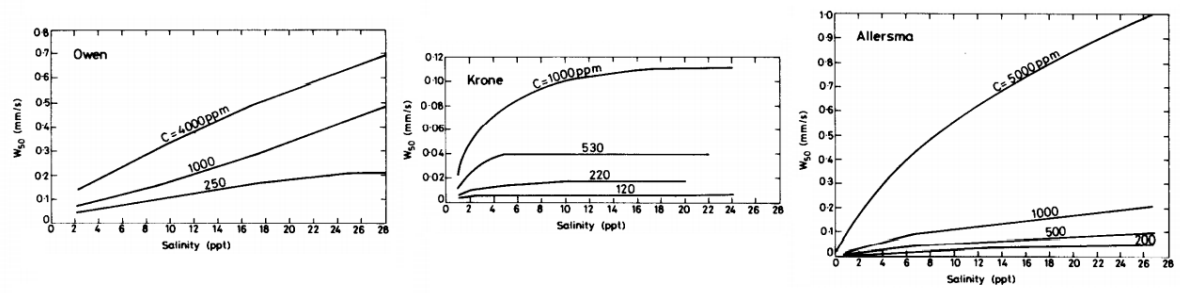

Figure 3.4: Settling velocity as a function of salinity for different studies (Van Rijn, 1993).

3.4.1. Floc erosion

During floc erosion, individual flocs are disrupted from the bed (Winterwerp & Van Kesteren, 2004). Flocs are disrupted when the shear stress applied to the bed (τ_b) is larger than the apparent critical shear stress for erosion of a floc (τ_{cr}). A well known approach is the formula of Partheniades for the erosion rate E

$$E = M\left(\frac{\tau_b - \tau_e}{\tau_e}\right) \quad \text{for} \quad \tau_b > \tau_{cr} \tag{3.10}$$

with M an erosion rate parameter with a value in the range of $0.01 \cdot 10^3$ - $0.5 \cdot 10^3$ kg/m^2/s.

3.4.2. Mass erosion

During WID, large amounts of sediment are deformed and eroded in a small amount of time (Schuurman, 1997). The erosive behaviour of WID is therefore identified as mass erosion. As is mentioned before in Section 3.2, mass erosion is an undrained process. The sediment deforms so fast that the pore water pressure cannot compensate for the pressure gradients induced by the deformation. Mass erosion occurs when the pressure applied to the mud is in the order of c_u or larger and much higher than the true critical shear stress for erosion τ_{cr}. According to Van Kesteren (2004) the criteria for mass erosion is

$$\tau_m \equiv \frac{1}{2}\rho u_j^2 > (2 \text{ to } 5)c_u \tag{3.11}$$

but only holds for flows parallel to the bed. Schuurman (1997) suggests for mass erosion the following criteria:

$$p_{intr} \approx 6c_u \tag{3.12}$$

with p_{intr} jet pressure at intrusion depth in [Pa].

4 | Fluid mud

Within the field of cohesive sediments, fluid mud is one of the forms in which it occurs but is treated as a separate chapter because the main process which is caused by WID is the fluidization and flow of mud. The properties of fluid mud and its behaviour as a density current are therefore described here in more detail.

4.1. Definition and characteristics

Fluid mud can be described as a suspension of cohesive sediment which has a concentration at or beyond the gelling point and where hindered settling dominates (Van Rijn, 2016). The gelling point is the boundary after which the structural density of the suspension is lost, i.e. the inter-particle stresses are close to zero (Winterwerp & Van Kesteren, 2004). If let to rest, fluid mud consolidates and forms a solid bed. The timeframe for consolidation can be days to years.

Fluid mud in general consists mainly of clay (fraction > 40%) and silt as was shown in Section 3.1. Mud from high-energy environments and subaqueous deltas does not contain a lot of organic matter (< 5%). Furthermore, fluid mud generally behaves like a viscoplastic fluid, as is further described in the next section. It is found that fluid mud has a yield stress and flow point stress.

4.2. Rheology

The rheological properties of fluid mud are the viscosity η, yield stress τ_y and flow point stress τ_f. τ_y is the stress threshold for mud to deform and τ_f is the stress threshold for mud to flow. Fluid mud has visco-plastic properties and is a shear-thinning material, which means that the viscosity decreases with increasing shear rate (Winterwerp & Van Kesteren, 2004). This behaviour is typical for non-Newtonian fluids, which is a fluid that is not following Newton's law of viscosity. For a non-Newtonian fluid, the viscosity changes with changing shear rate. The viscosity is not constant anymore. The behaviour of viscoplastic fluids and other kinds of non-Newtonian fluids is given in Figure 4.1.

Visco-plastic fluids often exhibit time-dependent effects, called thixotropy. The viscosity decreases with time at a constant shear rate and recovers back to its beginning state. This is illustrated in Figure 4.1 as a kind of loop. The solid line represents the ramp-up curve during which the structure of the flocs is broken down. After a period of constant shear stress, the vertical arrow, the ramp-down curve is illustrated by the dotted line. During ramp-down, the floc structure is built back up again if given sufficient time. The size of the area between the ramp-up and -down can be used as a measure for thixotropy.

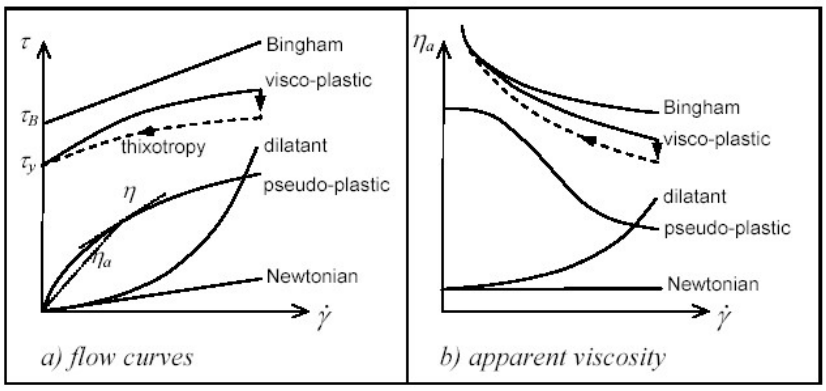

Figure 4.1: Flow curve and apparent viscosity of different rheological models (Winterwerp & Van Kesteren, 2004).

The thixotropic effects can be modelled as a time-dependent structural model with a rheological model.

During thixotropy, the ”links” within the skeleton structure of the soil are built-up and broken down. Moore (1959) suggests the quantity λ as an indication of the state of build-up. It is the number of links formed divided by the total number of links in the complete built-up state. It represents the state of flocculation. The rate of flocculation is given as

$$\frac{\mathrm{d}\lambda}{\mathrm{d}t} = a_\lambda (1 - \lambda) - b_\lambda \lambda \dot{\gamma} \tag{4.1}$$

with a_λ and b_λ constants for a particular mud which are to be empirically derived and $\dot{\gamma}$ is the shear rate. A rheological model which can be used to express the time dependent behaviour of fluid mud is the Houska model (Sesták et al., 1982):

$$\tau = \tau_\infty + \lambda (\tau_0 - \tau_\infty) + (\eta_\infty + \lambda c)\, \dot{\gamma}^z \tag{4.2}$$

τ_0 = yield stress at complete build-up (λ = 1)
τ_∞ = yield stress at complete build-down (λ = 0)
z = flow index
c = surplus viscosity index of fully structured fluid
η_∞ = viscosity index at build-down (= Bingham plastic viscosity if n=1)

4.3. Density current

Mobile fluid mud behaves as a density current (also called turbidity or gravity current). Due to the difference in density between fluid mud near the bed and water on top, the density current can be set in motion by gravity or a dynamic environment, e.g. by a current in the upper layer of the water column or waves. For this study, only the effect of gravity is taken into account. In the flume used for this study, no currents or waves are simulated and it is assumed WID maintenance dredging in the Port of Rotterdam solely depends on slopes in the bottom or sediment traps. Using the tide can help make WID more efficient by dredging during high water slack. When the tide becomes ebb, water flows out of the port and the tidal energy can be used additionally to transport fluid mud, but it is not investigated here.

Middleton (1993) and Van Rijn (2016) identified the characteristics of a density current. A sketch of the structure of the front of a density current is given in Figure 4.2 where the body and head of a density current are identified. For this study, only the behaviour of the body is of interest. In general, but not necessarily, the body exists of a sub-critical laminar flow with height d and more or less uniform flow velocity U and an upper layer that consists of turbulent ”wakes” or eddies with a size in the range of d. Between the upper layer and the water above, entrainment and the sub-critical flow and the bed entrainment takes place, which is treated in Section 4.5.

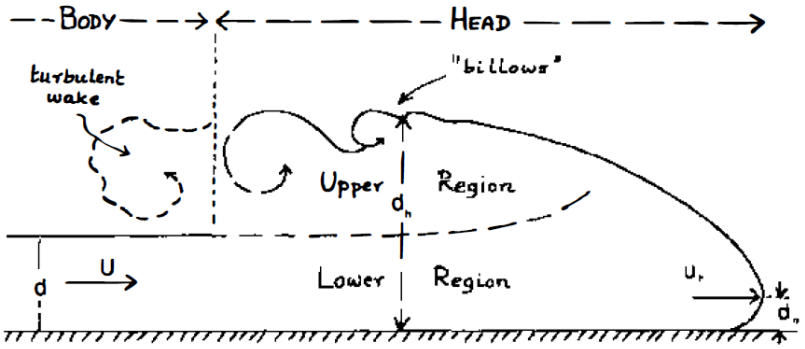

Figure 4.2: The structure of a density current (Middleton, 1993).

In the review of Middleton it is assumed that the density current is fully turbulent when the concentrations are sufficiently low. At high concentrations, the flow becomes laminar, which is the lower layer according to Van Rijn. From videos made by Mastbergen (1995) of density currents in flumes during WID experiments and from Figure 4.3 it is observed that density currents are mostly fully turbulent.

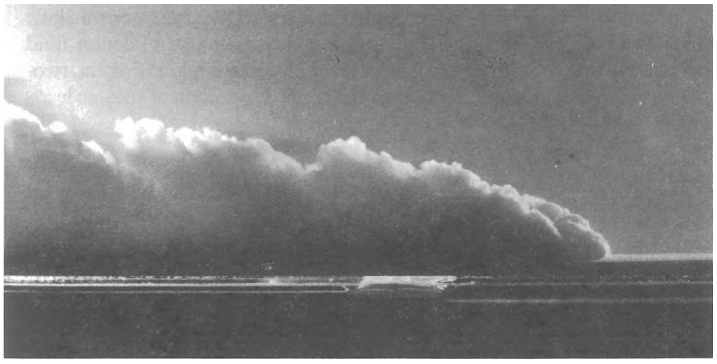

Figure 4.3: Side view of an experiment where a density current was produced (Middleton, 1993).

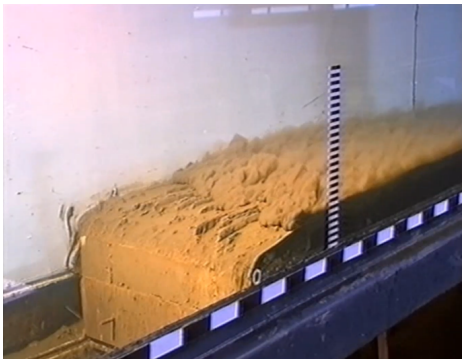

Figure 4.4: WID demonstration in a small scale flume at Deltares (Mastbergen, 1995).

4.4. Froude number and flow velocity

Some basic hydraulic principles are given here. The Froude and Reynolds number are defined as

$$Fr = \frac{U}{\sqrt{gL}} \tag{4.3}$$

$$Re = \frac{UL}{\eta} = \frac{\rho UL}{\mu} \tag{4.4}$$

L = characteristic length scale
η = kinematic viscosity (m^2/s)
μ = dynamic viscosity (Pa·s or N·s/m^2 or kg/(m·s))
g = gravitational acceleration

van Rijn (n.d.) defined Fr for a density current as follows (see Figure 4.5 as well):

$$Fr_2 = \frac{u_2}{\sqrt{\frac{\Delta\rho_m}{\rho_m} g h_2}} \tag{4.5}$$

with

$$\Delta\rho_m = \rho_m - \rho_w \tag{4.6}$$

Fr_2 = densimetric Froude number of the lower region of the density current
u_2 = maximum flow velocity within the lower region
h_2 = height of the maximum velocity with respect to the bottom
ρ_m = density of the mixture

To determine the flow velocity of the density current for a 2D case the Chézy equation can be applied for a density current with a shear stress at the top and bottom interface of the current (Middleton, 1993):

$$U = \sqrt{\frac{8g'}{f_b + f_i}} \sqrt{dS} \tag{4.7}$$

$$\tau_b = \frac{f_b}{4} \frac{\rho_m U^2}{2} \tag{4.8}$$

$$\tau_i = \frac{f_i}{4} \frac{\rho_m U^2}{2} \tag{4.9}$$

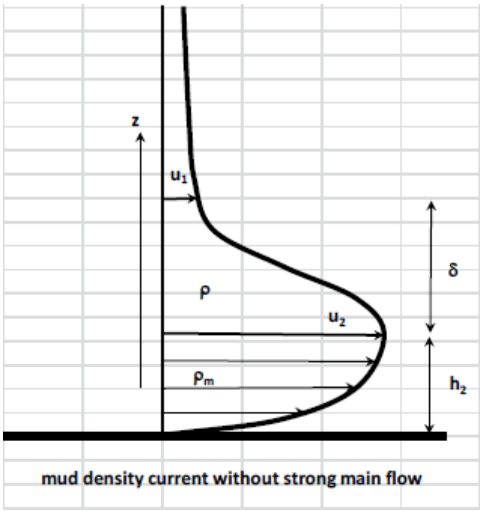

Figure 4.5: Schematization of the velocity profile of a density current without a flow on top van Rijn (n.d.).

S = slope of the bed
g' = buoyancy-reduced gravitational acceleration
f_b = friction factor at bottom
f_i = friction factor at interface
τ_i = shear stress at interface

$$g' = \frac{\rho_m - \rho_w}{\rho_m} g \tag{4.10}$$

The ratio between f_b and f_i is the same as the ratio of the respective shear stresses. When assumed that the bulk density of the current is uniform, the shear stress varies linearly with depth. At a distance of middle depth of the lower region, the ratio between the two friction coefficients is also equal to the ratio of the thicknesses of the part of the flow below the velocity maximum (at which the average shear stress is zero) d_b and the thickness of the part of the flow above the velocity maximum d_j.

van Rijn (n.d.) provides formulas to determine the critical and equilibrium depth of the lower region. d_{cr} is the depth when the flow of the lower region is critical (Fr = 1). $d_{eq,turb}$ is the equilibrium depth for a turbulent flow and $d_{eq,lam}$ for a laminar flow.

$$d_{cr} = \left(\frac{q^2}{((\rho_s - \rho_w)/q_d) c_m \; g \; \cos\beta} \right)^{1/3} \tag{4.11}$$

$$d_{eq,turb} = \left(\frac{(f_b + f_i) q^2}{((\rho_s - \rho_w)/\rho_m) c_m \; g \; \sin\beta} \right)^{1/3} \tag{4.12}$$

$$d_{eq,lam} = \left(\frac{(\tau_i + \tau_b) d^2}{(\rho_s - \rho_w) c_m \; g \; \sin\beta} \right)^{1/3} \tag{4.13}$$

q = $U \cdot d$
β = bed slope

4.5. Entrainment

Entrainment in hydraulics is described as the dynamics of a fluid caused by the dynamics of another fluid. For a density current, this happens on top, within and underneath the density current.

Upper layer
As is shown in Figure 4.3, the height of the density current increases just after travelling of the head. As the water stays clear above the current, this means water from the upper part entrains into the density current caused by the Kelvin-Helmholtz instabilities.

According to Winterwerp (1998), when WID is deployed in still water, the fluid mud layer is not eroded and no entrainment takes place from mud to water column. The thickness is not affected and is in a quasi-steady equilibrium.

Lower layer
In density currents which flow down a slope, some particles settle towards the bed and cause the bulk density to decrease. According to Middleton (1993) the question is whether these particles stay there or erode again. As was discussed in Section 3.4.1, the bed shear stress needs to be larger than the critical shear stress for the motion for the particles to erode. Erosion due to density current motion, i.e. entrainment from consolidated bed to fluid mud, is not expected to have a significant impact.

Entrainment between the upper and lower layer is mainly downwards and happens during the first couple of seconds when the upper layer has a relatively high concentration, i.e. the density gradient is small. Afterwards, a clear distinction occurs between the upper and lower regions and (almost) no entrainment between the two layers occurs.

4.6. State and stability
The stability of a density current is defined as a stable interface between the fluid mud and water layer on top. No extensive entrainment takes place between the two layers (Mastbergen & Pennekamp, 1994). If the concentration gradient over the depth at the interface is large, an unstable flow can occur. A mixing layer can be created which can be recognized by Kelvin-Helmholtz instabilities. This is a phenomenon which is often observed in density currents created by WID (Middleton, 1993). From videos of experiments done by Mastbergen (1995) this is also observed. The stability of the boundary layer of a density current can be quantified by the Richardson number Ri:

$$Ri = \frac{-g\frac{d\rho}{dz}}{\rho\left(\frac{du}{dz}\right)^2} \tag{4.14}$$

z is the relative position from the bed (positive upwards) and $u(z)$ is the flow velocity in the flow direction of the density current at height z. $\rho(z)$ is the density at height z. The nominator has a minus sign because the gradient in density is negative and thus makes Ri a positive number. Ri gives the ratio between the stabilizing and destabilizing effects, i.e. the effects of gravity and density against the velocity gradient which forms shear stresses on the interface. Experiments suggest $Ri > \beta$ for β = 0.3 - 0.4 for stability. The final stability criterion according to Mastbergen (1986) is:

$$\beta \cdot Fr_i^2 < \frac{\delta}{h_2} < 2 \tag{4.15}$$

with δ is the boundary thickness layer (see Figure 4.5) and Fr_i the internal Froude number

$$Fr_i = \frac{U}{\sqrt{2\frac{\Delta\rho}{\rho_m}gh_2}} \tag{4.16}$$

For a derivation and elaboration of this stability criterion, the reader is referred to Mastbergen & Pennekamp (1994).

4.7. Numerical models
Up to now, CFD models have been the only source of in-depth information on density currents. To be able to make a visual interpretation, some CFD modelling on density currents is presented here.

In Figure 4.6, the result of a simple 1DV model simulation is shown for a plume height of 2 meters. The left figure shows a thick layer with a high concentration and a thin layer with a low concentration

of sediment. The right figure shows that the maximum velocity occurs at the interface between the low and high concentration layer. The flow velocity near the bed is close to the velocity of the water on top.

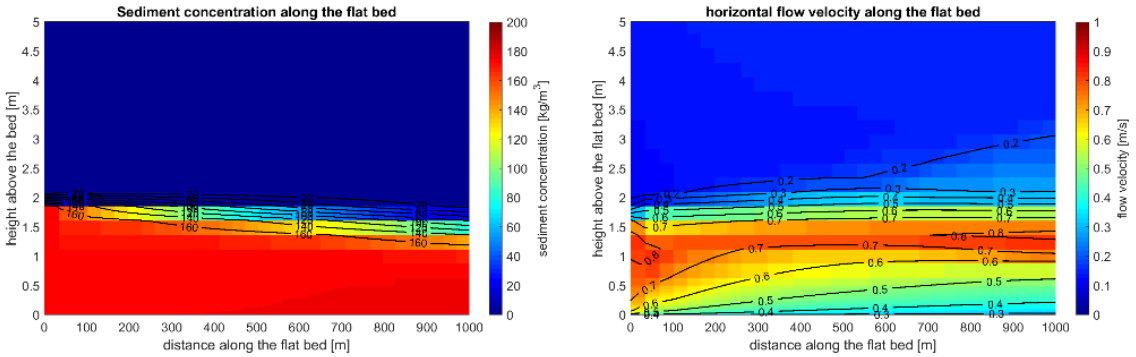

Figure 4.6: 1DV model simulation of WID with a plume height of 2 m and an initial sediment concentration of 170 kg/m^3 and 0.7 m/s flow velocity (Kirichek et al., 2021).

A 3D simulation is shown here to provide a more detailed view of the current (Figure 4.7). In the bottom figure, it can be observed that high concentrations occur near the bottom with a more or less constant height and at the upper interface turbulence occurs. Again, Kelvin-Helmholtz instabilities are visible. Furthermore, the density current has a head and body, as is explained in Section 4.3.

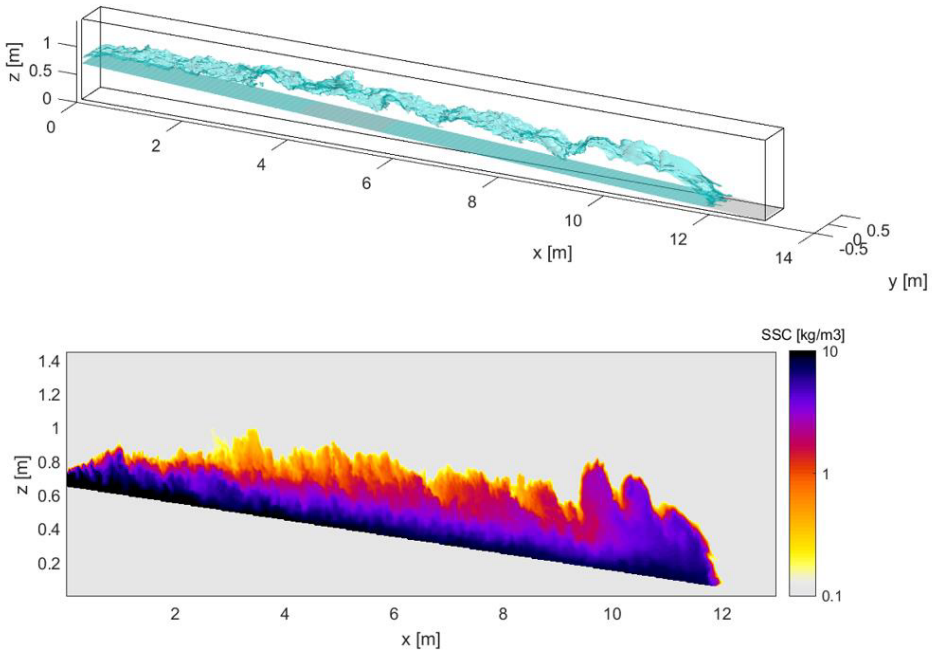

Figure 4.7: LES CFD simulation of a density current down a slope with TUDflow3D (Kirichek et al., 2021).

4.8. Laminar-Turbulent transition

In the lecture notes of Talmon (2020), the transition from laminar to turbulent flow in open channels of homogeneous, non-Newtonian mixtures is discussed. From the data collected during experiments, it was observed that for Re = 700 the data started to deviate from the laminar trend ($16/Re$). Haldenwang et al. (2010) found an empirical relation for the onset of the laminar-turbulent transition:

$$\mathrm{Re}_{cr} = 853.1\left(\frac{\eta_{\text{water}}}{\eta_a(100s^{-1})}\right)^{0.21} Fr + 12630\left(\frac{\eta_{\text{water}}}{\eta_a(100s^{-1})}\right)^{0.75} \tag{4.17}$$

The range from which this empirical relation was derived is 1.1 < Fr < 5 and 600 < Re_{cr} < 2400. η_{water} is the viscosity of water and $\eta_a(100s^{-1})$ the apparent viscosity at a shear rate of 100 s^{-1}. When the onset of turbulence can be predicted, the necessary flow velocity U (embedded in Fr) can be determined and the turbulence can be used as a potential anti-settling mechanism (Section 4.9).

4.9. Anti-settling mechanism

Turbulence can be used to keep particles in suspension for a longer time due to the turbulent eddies which occur in the flow. This is also known as autosuspension (Middleton, 1993). According to Bagnold, the particles contain the gravitational energy to sustain the turbulence which keeps the particles in suspension and overcomes friction at the upper and lower interfaces. The condition for autosuspension is

$$w_s \leq eSU \tag{4.18}$$

with e an efficiency coefficient. Whether this criterion works or not is still debated, but if it does work, then Seymour (1986) suggests e < 0.1. U and/or S need(s) to be large enough to generate enough turbulence, hence counteract the gravitational pull on the particles. As S is often small in ports in Europe, and during the experiments of this study, U must be large for the condition to work.

5 | Experimental setup

This chapter describes the setup and methodology of the experiments conducted for this study. The materials, design of the different components of the tests, the layout of the flume, the methodology of measuring and the execution of the experiments are described.

5.1. General description

For the experiments of this study the process of WID is simulated for different parameter settings of WID on a 0.5 meter thick bed of mud from the Port of Rotterdam. The WID experiments are carried out in the water-soil flume of Deltares. This flume is 50 meters long, 2.5 meters deep and 5 meters wide. For this study the test section of the flume is 33 meters long, 2.5 meters deep and 2.4 meters wide.

The jetbar passes over the bed of mud injecting it with water, bringing the mud in suspension and create a density current. At the end of the bed the fluid mud flows into a steep slope, or an abyss, like is done during the experiments of Mastbergen (1995) (see Figure 4.4) to make sure the sediment is removed from the injected stretch of mud like in the field. At the abyss the properties of the density current are measured. Furthermore, the difference in height of the bed is measured during and after the process with an echo sounder and a disk. From the difference in bed level and properties of the density current after each run the production can be determined in two ways. At last, physical samples of the density current at the abyss were intended to be collected to determine the rheology, in particular the Bingham yieldstress (τ_B) and dynamic viscosity. However, during the execution of the experiments, this did not succeed because of clogging of the pump tubes.

Definition: tests and runs
In this report a *test* is defined as a set of runs with the same operational parameters. A *run* is the passing of the jetbar over the bed of mud. During each test it is the goal to do at least three runs.

5.2. Scaling

In the previous section it was mentioned that the water-soil flume is used to conduct the experiments in, but initially it had to be decided whether the water-soil flume or a smaller one was going to be used. The difference and consideration between the two is given below. Here the water-soil flume is referred to as the ”large scale” flume.

	Large scale flume	**Small scale flume**
Dimensions (L x W x H)	33 x 2.4 x 2.5 m	9.5 x 0.5 x 0.6 m
Scaling	Close to 1:1	1:5 to 1:10
Number of tests	6 tests on 0.5 m mud consisting of 4 trials each	6 or more tests on 0.1 m mud consisting of 4 trials each
Relative costs	High costs for small amount of tests	Low costs and more tests possible
Results	High quality results because of realistic situation	Debatable quality of results because relation of unclear effect of down-scaling on non-Newtonian behaviour

Table 5.1: Comparison between the large scale and small scale flume.

When down-scaling the dimensions of the flume, the properties of the mud need to be scaled as well in order to down-scale the dimensions of the density current. Whether down-scaling of non-Newtonian properties of fluids is possible is still under debate. A non-trivial scaling theory for non-Newtonian fluids is even considered impossible (Astarita, 1979). Scaling laws for rheology can not be found in literature,

but Liard et al. (2014) describes how the viscosity of non-Newtonian fluids can be influenced by means of the concentration and provides some scaling formulas for this.

In order to get the most reliable results, it was decided not to scale down, i.e. to use scaling close to 1:1 and thus conduct the experiments in the large scale flume. In this way, the resulting non-Newtonian density current flow is very close to the prototype scale. It is worth noting that the 1:1 scaling concerns the density current height, flow velocity and density and mud characteristics, but not the jetbar dimensions. In Section 5.7 it is shown that the dimensions of the nozzles of the jetbar are scaled down by a factor 3 to 4. Despite this, the scaling of the overall experiments is still close to 1:1 because the density current and production properties as a function of the momentum applied by the jetbar are the same as would be observed in the field.

5.3. Testmatrix

The experimental period consists of a trial week and the official tests. During the trial week the setup and all instrumentation were tested. Moreover, a couple of runs were done over the bed with 4 nozzles in the jetbar with a D_n of 20 and 30 mm to see what the intrusion depth is. Theories to determine the intrusion depth were mentioned in Section 2.2, e.g. Equation 2.5 produced by Swart (2015). The outcome of Equation 2.5, however, is in the order of meters for the settings of the experiments. Furthermore, v_t is not taken into account in this equation and it is therefore concluded that predicting the outcomes of the experiments with these formulas is very difficult. The predictions used in this report are based on experiences of experts from Deltares. The settings of the runs during the trial week are given in Table 5.2. v_t is kept constant to be able to compare the different runs. From these results it is decided what D_n is used during the official tests.

The official experiments consist of 6 tests with each (preferably) 4 runs. The settings which change between the tests are v_t, p_j, D_n and SOD. v_t is 0.25 and 0.40 m/s. These values are chosen such that the density current has sufficient time to develop during traversing. As the bed is only 27.1 meters long, a velocity of 0.40 m/s would make the traversing time around 1 minute.

p_j is 0.5 or 1 bar. In practice, a pressure of 1 bar is usually applied. To compare the results with another pressure a lower value is chosen because it is expected that a higher p_j blows too much sediment away. It is the goal to do at least 3 runs on a 0.5 m thick bed. The testmatrix for the official tests with the target settings is given in Table 5.3.

		Run 1	**Run 2**	**Run 3**	**Run 4**	**Run 5**	**Run 6**
v_t	m/s	0.25	0.25	0.25	0.25	0.25	0.25
D_n	mm	20	20	20	30	30	30
p_j	bar	0.5	1	1.5	0.5	1	1.5

Table 5.2: Testmatrix: trial week.

		Test 1	**Test 2**	**Test 3**	**Test 4**	**Test 5**	**Test 6**
v_t	m/s	0.25	0.40	0.25	0.40	0.25	0.40
D_n	mm	30	30	30	30	30	30
p_j	bar	1	1	0.5	0.5	1	1
SOD	m	0	0	0	0	0.40	0.40

Table 5.3: Testmatrix: target settings. Actual settings of the experimental tests can be found in Table 6.15

.

The testmatrix changes during the execution of the experiments because the results from the trial week did not repeat themselves during the actual tests. These changes are given and explained in the test results (Chapter 6).

5.4. Flume layout

As was mentioned before, the experiments for this study are conducted in the water-soil flume of Deltares. The dimensions of the whole flume are 50 m long, 9 meters wide and 2.5 m deep but for the

experiments a section of 33 m long, 2.4 m wide and 2.5 m deep is taken to conduct the experiments in. The bed of mud which is injected with water is 27.1 meters long.

A schematization of the setup of the flume is given in Figure 5.1. The bed with a height of 0.5 m of mud is held by a ramp at one end and by the wall of the flume at the other end. On top of the ramp a measuring frame is installed to measure the properties of the density current (velocity and density). Details of the measuring frame are given in Section 5.8. At the start of a run the jetbar is in position behind the ramp. At the same time the frame is tilted down so the jetbar can move over it. The jets are turned on by the pumps and the jetbar starts traversing towards the bed. When the jetbar passes the ramp with the frame on top, the frame is raised vertically.

Electromagnetic flow velocity meters and two conductivity bars are attached to the measuring frame on top of the ramp. Behind the jetbar are two conductivity bars as well attached to the cart combined with an echo sounder. Both pairs of conductivity bars provide a signal of the density for physical understanding of the density current and for model validation of Ten Brummelhuis (2021).

The water for the jetbar is pumped from a secondary basin of the flume next to it. The material which flows over the ramp is immediately pumped to the cellar but because the primary and secondary basin are connected by a hole in the wall, some suspended material and salt flows to the secondary basin. During the jetting process the pumps move away from the hole where the suspended material and salt enters the secondary basin. Together with the assumption that the concentrations of suspended material and salt entering this part of the flume stay low it can be assumed that the water jetted by the jetbar is close to 1000 kg/m^3.

After every run the jetbar removes a certain amount of material so the level of the bed is lowered. The bed is also held in place with a ramp made of steel bars (height of 50 mm each) so that it is held in place. To make sure the ramp does not obstruct the density current and measuring equipment during the next run, it is lowered by removing bars every time to the new level of the bed together with the measuring frame.

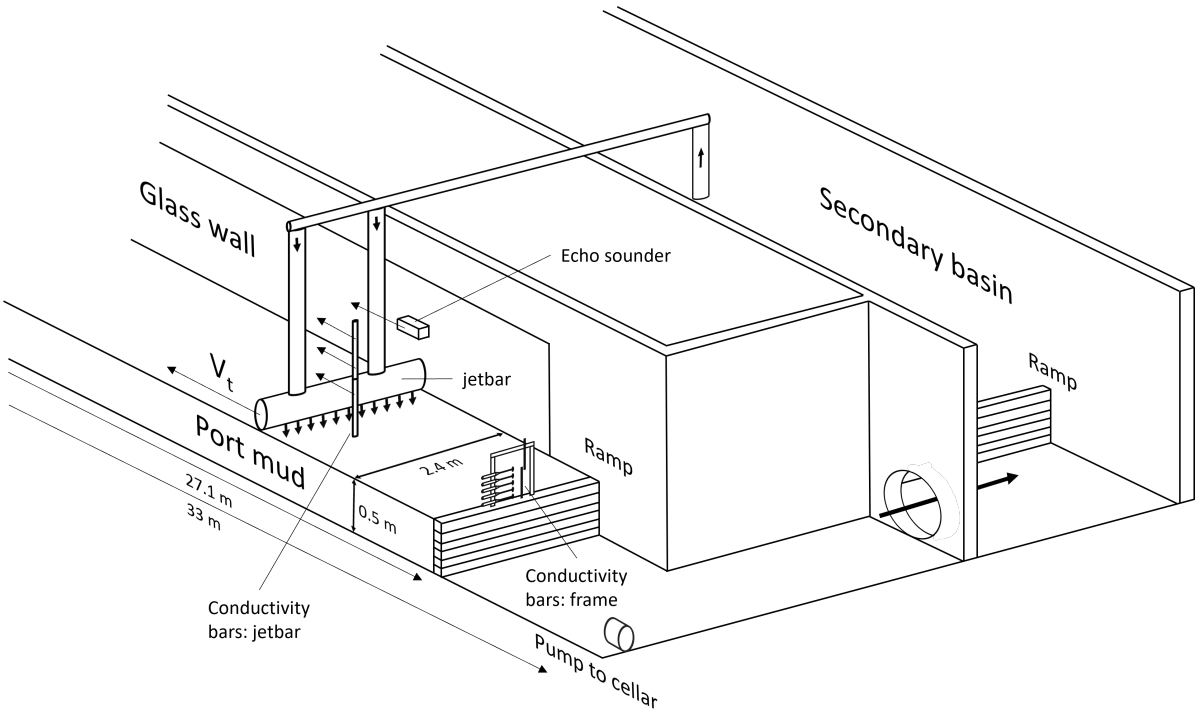

Figure 5.1: Schematization of the experimental setup in the water-soil flume.

Figure 5.2: Impression of the flume after preparation of the sediment before the start of a test.

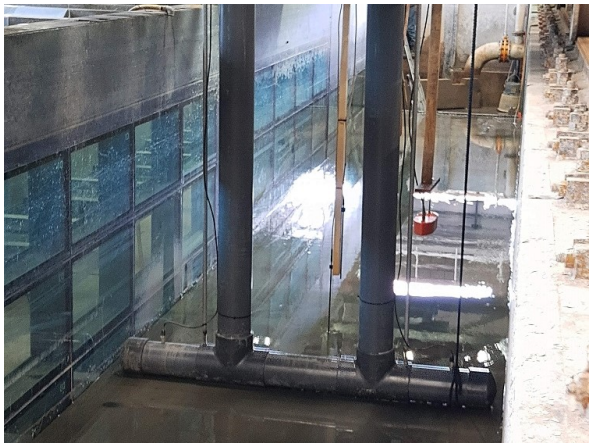

Figure 5.3: The set up of the jetbar on top of a mud bed with a row of conductivity bars and an echo sounder behind it.

5.5. Port mud

The flume is filled with 32.5 m^3 of mud from the Calandkanaal of the Port of Rotterdam in front of the Ertsoverslag Europoort CV (EECV) (Figure 5.4) for each test. This is the location where the technique of WID is currently performed for maintenance dredging. The green line in Figure 5.4 marks the berth where ore vessels dock to unload and the blue line marks the area where the mud had to be collected. Preferably the mud had to be collected as close to the berth as possible because there WID is preformed as well.

For each test fresh mud was collected at different locations in front of the berth. The numbers in Figure 5.4 correspond to the tests. The location of collection could not be kept constant because vessels were constantly (un)docking or there were ongoing WID operations.

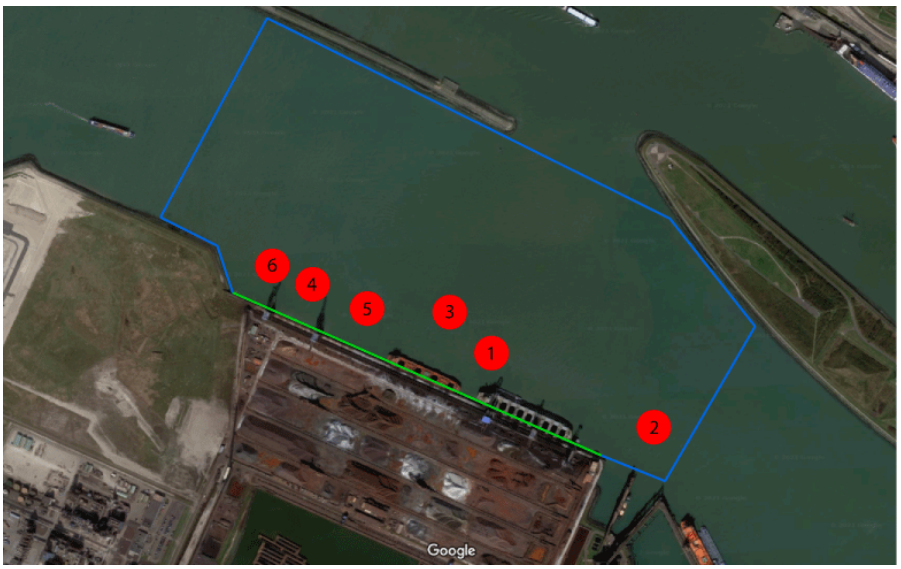

Figure 5.4: The location where the mud was located (indicated in blue). The location had to be as close to the berth of EECV (green line) (Google Maps).

For the tests it is assumed the mud is a Bingham fluid. The Bingham yield stress τ_B of the mud for the tests had to be in the order of 100 Pa (density of 1200 kg/m^3). During earlier collections of mud it was found that 0 - 20 m from the berth τ_B was in the order of 70 Pa. This was probably caused by previous WID operations. At a distance of 20 - 50 m from the berth τ_B was $\approx$ 100 - 150 Pa.

Parameter determination on site

During collection of the mud a portable rheometer (Fann 286) was used on site during the first two times (see Figure 5.5). The device measures the shear stress for different RMP speeds with a BOB-cup geometry. Via an excelsheet the shear stress is converted to a flow curve of the material from which the rheological parameters can be determined on site. It was unfortunately not possible to measure τ_B of the material above 80 Pa so the parameters had to be found from the rheometer at Deltares when the mud was already in the flume.

Determining the order of magnitude of the strength of the material on site was done based on experience after collection for test 2. When the material had a thick, creamy texture which would stick to the upside-down surface of a metal the strength was considered sufficient. This was later confirmed with rheotests at Deltares. The results of the parameters which were found for each test are given in the next chapter.

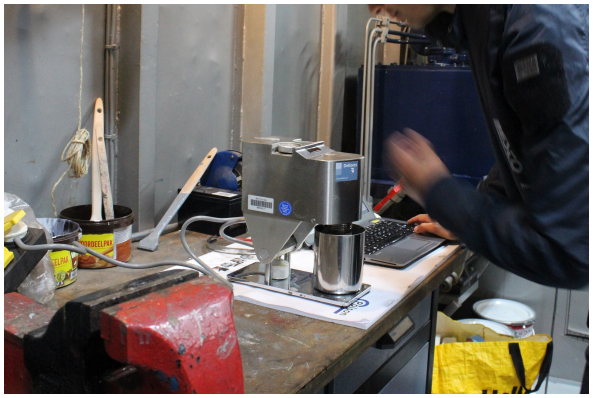

Figure 5.5: Usage of Fann 286 on board during the first time. Inside the cup is a BOB-geometry.

Figure 5.6: A mud balance to obtain a rough estimate of the density of a material, in this case harbour mud.

A rough estimation of the density of the mud also gave an indication of the material properties on site. For this a so called *mud balance* was used from Deltares (see Figure 5.6). This is simply a scale with a cup and the end which needs to be filled with mud. At the other end a weight needs to be moved over the bar to balance the scale. The eventual position of the weight indicates the density of the material inside the cup. If the density was 1200 kg/m^3 then τ_B was also between 100 and 150 Pa.

Collection and transportation

The mud was collected by a clam shell equipped dredging vessel and pumped into a pump truck. First, the top layer of the bed of the Calandkanaal was dredged by a crane and loaded into the hopper of the vessel. The hopper was filled to about 1/5 of its capacity together with some water. After loading, the vessel sailed to the Scheurhaven and mixed the mud with some of the water. Determining the quality of the mixture was done as explained in the previous section.

After mixing in the hopper the mud was pumped into a truck and transported to Deltares. After arrival the material was pumped into the flume and spread equally over the length. These steps are visualized in Figure 5.7a to 5.7d. As one can see from Figure 5.7b, the texture of the mud varied heavily in the hopper after dredging. Taking a sample from it and measuring it did not mean that the values found were the same for the whole dredged volume. The pumping into and out of the truck also caused

Trial week	21-6-2021
Test 1	28-6-2021
Test 2	5-7-2021
Test 3	8-7-2021
Test 4	13-7-2021
Test 5	16-7-2021
Test 6	21-7-2021

Table 5.4: Dates of the steps carried out from Figure 5.7 per test. Steps a to d were carried out in 1 day.

(a) Crane loading the mud into the hopper.

(b) Mud inside the hopper after dredging.

(c) Pumping the mud from the hopper into the truck for transport to Deltares.

(d) Pumping the mud from the truck into the flume.

Figure 5.7: Steps for collecting the mud from the port and transport to Deltares.

some degree of remolding. The eventual strength of the mud could only be determined after the flume was filled with the mud.

5.6. Salt versus fresh water

In this section, the difference in properties of salt and fresh water is discussed and is used to support the decision to use fresh water over salt water in the flume. In Section 3.3.4 the influence of salinity on flocculation was discussed. It was concluded that salt can have a significant influence on the attracting and repelling forces on flocs. For the experiments, it was decided to use fresh water (tap water) instead of salt water from the port. Although using salt water would give a more realistic situation, due to budget, time and logistic reasons, fresh water was used. To analyse the influence of fresh water on the behaviour of the density current, dilutions of mud with tap water and salt water from the port were analysed in different ways.

Rheological parameters

First the rheology of the two dilutions in volume on mud (from the Calandkanaal in the Port of Rotterdam) was analysed for a 1:1 and 1:0.6 dilution with a controlled shear-rate test (BOB-geometry). τ_B and dynamic viscosity for the suspensions were measured from the ramp-down curve and analysed. The results are given in Table 5.5. The flow curves obtained from the rheometer can be found in Appendix A.

The differences in viscosity from the table of salt and fresh water is in the order of 10% to 15% and the difference in yield stress is around 2 Pa. These differences are considered small enough not to have a significant influence on the rheological behaviour of the density current. The shear rates within the

Water type dilution	Dilution ratio	Density	τ_B	Plastic viscosity
Fresh	1:1	1.1359 g/cm^3	3.35 N/m^2	0.0096 Pa·s
Fresh	1:0.6	1.1653 g/cm^3	11.5 N/m^2	0.113 Pa·s
Salt	1:1	1.1336 g/cm^3	2.50 N/m^2	0.0081 Pa·s
Salt	1:0.6	1.1669 g/cm^3	9.60 N/m^2	0.1258 Pa·s
No dilution	-	1.2381 g/cm^3	150 N/m^2	2.85 Pa·s

Table 5.5: Rheology of different dilution ratios with salt and fresh water.

current are not large and the current only exists for no longer than 3 - 4 minutes.

Zeta potential

Another way to analyse the flocculation is a zeta potential (ZP or ζ-potential) analysis. ZP is defined as the electric potential at the slipping plane of a floc (Chassagne, 2019). It is the potential difference, in volts (V) or milivolts (mV), between the ambient fluid and the stationary layer of fluid attached to a floc. The ZP can be either positive, negative or (close to) zero. When a suspension contains a relative large amount positive ions in the ambient fluid (e.g. a suspension with salt water) the negatively charged particles will be drawn more closely to each other i.e. the attracting force becomes larger. The ZP becomes smaller, which means that the closer the ZP to zero the more potential for flocculation and the further from zero the less potential for flocculation. In this case, as flocs are slightly negatively charged, the ZP is negative for mud.

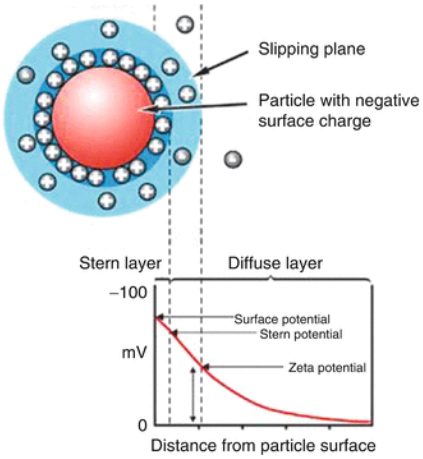

Figure 5.8: The potential difference as a function of the distance from the surface of a particle (Williams, 2016).

For this study a couple of 1:4 dilutions with fresh and salt water were made in the lab and after settling for 10 minutes the top, low concentration suspension was analysed. The ratio of dilution for a ZP analysis not is important because the suspension needs to contain only a couple of flocs. 3 samples where measured of which each was analysed 3 times, so each suspension was measured 9 times.

The difference in ZP between both dilutions is 2.1 mV and in comparison to a fresh water dilution 14.1%. The ZP is well below zero and is for both dilutions in the same order of magnitude. Also a difference of 14.1% is considered sufficiently small not to have a significant difference.

Type of dilution	ZP (mV)	Mobility (μmcm/Vs)	Conductivity (mS/cm)
Salt	Average : -12.8 SD: 0,917	Average: -0.9055 SD: 0.06531	Average: 20.9 SD: 0.963
Fresh	Average: -14.9 SD: 0.836	Average: -1.058 SD: 0.05918	Average: 9.39 SD: 0.299

Table 5.6: The measured zeta potential of a salt and fresh water dilution. SD = standard deviation.

Particle size distribution

A third method to show the difference in influence between salt and fresh water for the experiments is the particle size distribution (PSD) of both types of suspensions after a certain amount of time. In Figure 5.9 the PSD after 0.5, 3, 30 and 60 minutes after dilution is given for both fresh and salt water dilutions (blue and green respectively). Also, for this analysis, the ratio of dilution is not important because a tea spoon of suspension is dripped into a glass of clear water and then pumped through the PSD device.

For the first 30 minutes the peaks of the distributions are at almost equal positions for both dilutions, but the green peaks have a slight shift towards the right. The blue peak is at 15 μm and the green peak is at 20 μm. The peak is also a little bit lower and the curve is more distributed to the higher particle sizes, but it does not change during the first 30 minutes as well. The light green and blue lines represent

the distributions after 60 minutes and form a second peak at 91 and 79 μm respectively. Flocculation occurs after 30 minutes of mixing, so long after the end of a run.

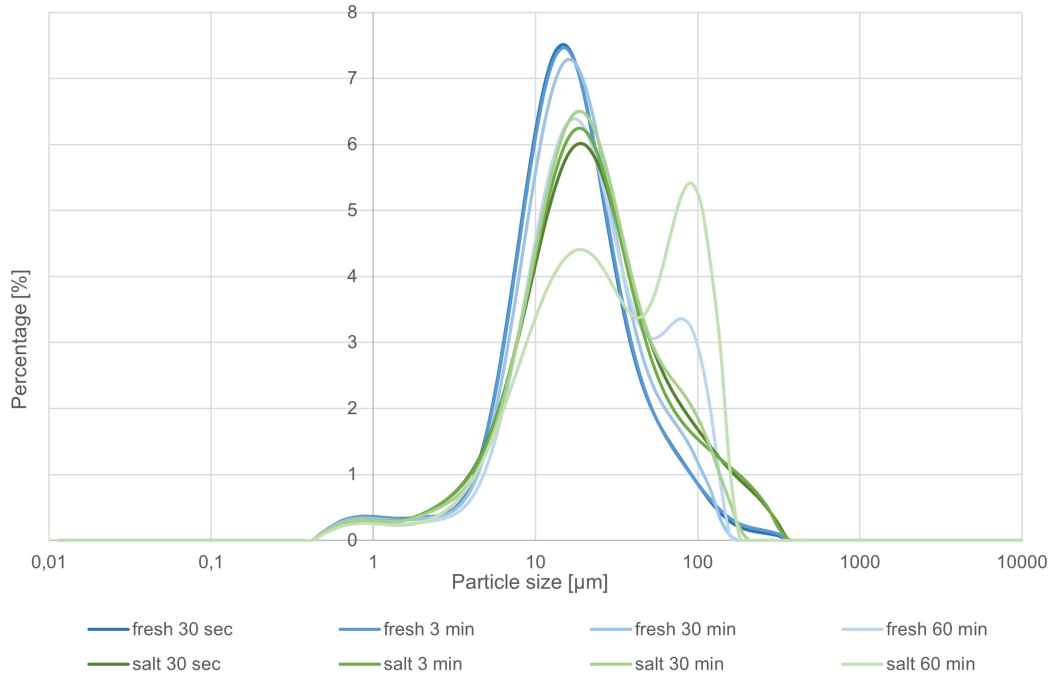

Figure 5.9: PSD of a salt (green) and fresh water (blue) dilution after 0.5, 3, 30 and 60 minutes.

According to the comparison of Winterwerp & Van Kesteren in Figure 3.2, Δw_s between D_f 15 and 20 μm is 0.02 mm/s and Δw_s between D_f 91 and 79 μm is 0.06 mm/s. Over the time span of a run this would lead to less than a couple of centimeters settling between a fresh and salt water dilution of the mud for a single floc.

Based on the analysis done on the rheological parameters, ZP and PSD for salt and fresh water dilutions on mud from the Port of Rotterdam it is concluded that the influence of fresh water in comparison to salt water is negligible on the time spans of a run of these experiments, which is in the order of 3 - 4 minutes. The difference in τ_B and ZP are small enough and in a range low enough not to have a significant or noticeable difference during the tests. A change in PSD is only noticed after 30 minutes, long after which the density current stops flowing.

5.7. Jetbar design

To simulate the jetting process correctly a proper design of the jetbar had to be in accordance to the size of the flume. The jetbar consists of PVC tubes with an inner diameter of 200 mm and 24 nozzles with an in-between distance of around 100 mm. A schematization of the jetbar can be found in Figure 5.10. The distance between the walls and the two ends of the bar is 50 mm in order not to hit the walls during traversing. The jetbar is initially designed for D_n = 30 mm. During the trial week the effect of different D_n on the intrusion depth is investigated.

According to Bernoulli, p_j as a function of u_j is

$$p_j = \frac{1}{2}\rho u_j^2 \tag{5.1}$$

and thus

$$u_j = \sqrt{\frac{2p_j}{\rho}} \tag{5.2}$$

The maximum pressure applied to the jetbar is 1 bar, which gives u_j = 14 m/s out of each nozzle. From photo's of WID activities online it was observed that a distance between nozzles was around 400 mm with D_n = 90 mm. For the purpose of this study an intrusion depth of around 10 to 15 cm was aimed for. This range is inside the flow development region, which ends at distance from the nozzle s = 6.2 · 30 mm = 18.6 cm. The slope of the turbulent cone of the jet within this region is around 1:10. With a heart to heart distance of 10 cm, the distance between two neighbouring cones ranges from 3.4 cm to 5 cm at s = 18.6 cm and 10 cm respectively.

The jetbar was initially designed with the formula of the velocity distribution for a fully developed flow region of a free flowing jet. Unfortunately, this mistake was noticed after the execution of the experiments.

During the experiments the pressure out of each nozzle over the length of the jetbar had to be equal. This was a requirement for the design so that the bed would be equally penetrated. If the pressure would differ over the length a difference in penetration depth over the width of the flume would occur and this would make post-processing more difficult. It was decided that the flow velocity within the horizontal tube could not be larger than 2 - 3 m/s in order to avoid pressure differences over the length of the bar.

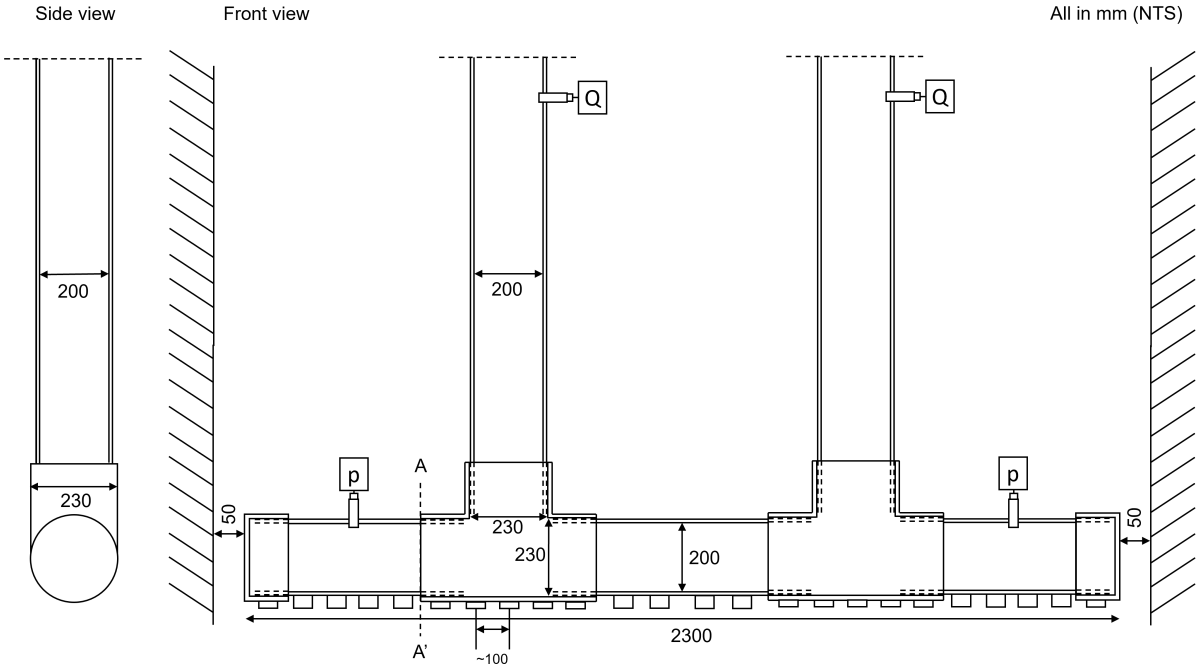

Figure 5.10: Schematization of the jetbar design.

With 24 nozzles, D_n = 30 mm and u_j = 14 m/s results in a total discharge of 166 l/s and thus each vertical pipe 83 l/s. Each vertical pipe splits up in two horizontal directions and has to supply 12 nozzles. The maximum discharge in horizontal direction would occur in cross section A-A'. The discharge there would be (5/12 * 83 l/s =) 34.6 l/s or the velocity would be 1.1 m/s (for 200 mm tubes). At all other intersects of the horizontal pipe the flow velocity is lower. So the pressure is equally divided over the horizontal length of the jetbar. Because of this and the practical dimensions of suppliers of Deltares, the 200 mm tubes were chosen.

At last, pressure and discharge meters are installed on the jetbar which are schematized in Figure 5.10 as p and Q respectively.

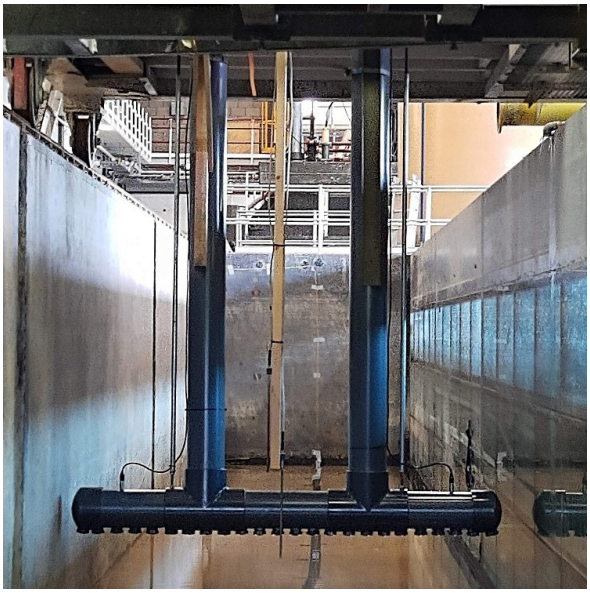

Figure 5.11: Final construction of the jetbar in the flume.

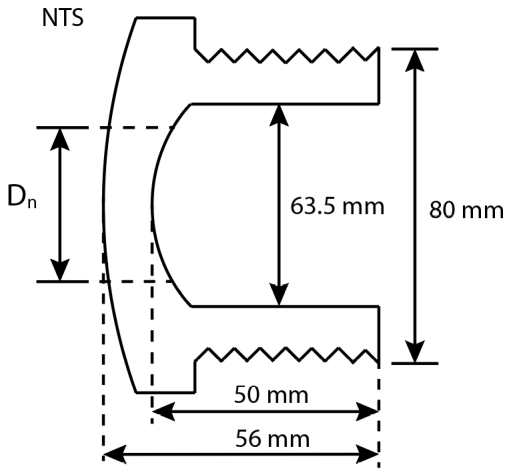

Figure 5.12: Technical drawing of PVC nozzle with variable D_n.

5.8. Measuring techniques

In this section different measuring techniques used for the experiments are summarized. Measurements were taken from three components of the experiments: the bed (rheology and bathymetry), the density current (concentration, velocity and rheology) and the jetbar (pressure and discharge).

5.8.1. Measuring positions

Measuring equipment is positioned at the measuring frame on top of the ramp and behind the jetbar. At the measuring frame probes for the bi-directional flow velocity and the conductivity of the medium are attached together with tubes to take samples for the rheology. The conductivity is later calibrated to density and concentrations. These concepts are more explained in Section 5.8.2 and 5.8.3 respectively. A photo of the frame is given in Figure 5.14 and is schematized in Figure 5.13.

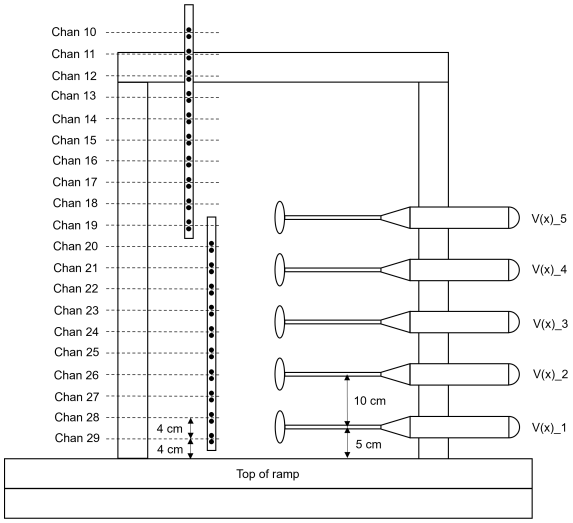

Figure 5.13: Schematization of the layout of the measuring frame at the end of the flume.

Figure 5.14: Photo of the measuring frame at the end of the flume.

On the left side of the frame, two conductivity bars are connected with each 10 probes. The distance between each probe is 4 cm, also between the upper probe of the lower bar and the lower probe of the upper bar. On the right side are five E40 probes with a distance of 10 cm between each. These are electromagnetic velocity meters.

Three tubes are connected to the E40 probes (top, middle and bottom). Through these tubes, physical samples are collected to measure the rheology of the density current. The samples are pumped up at the side of the flume by so-called tube pumps. These are wheels which press with a rotating movement along the tubes and push the liquid from one side of the pump to the other one.

Behind the jetbar the conductivity bars are placed at a distance of 1.4 meters from the jetbar and 1.2 meters from the wall (the wooden pole in Figure 5.11). The echo sounder is placed right next to the conductivity bars. The relative z-coordinate of the lowest probe behind the jetbar in comparison to the lowest probe of the bars at the frame is provided in Chapter 6.

5.8.2. Bi-directional flow velocity

The bi-directional flow velocity is measured by E40 probes from Deltares. These electromagnetic velocity meters (EMV) work with the principle of electromagnetic suspension (EMS). EMS is described as the magnetic levitation of a material in a magnetic field of a constantly changing strength. The charged particles of the flow experience a Lorentz force which acts in the direction perpendicular to the flow direction as well as the direction of the magnetic field (Leeungculsatien & Lucas, 2013).

The probes contain a magnetic core inside which produces a magnetic field through which the (conductive) liquid flows with velocity u (see Figure 5.15). The liquid passes around the exterior of the probe and cuts the lines of the magnetic induction (B). This generates a flow voltage (or induced electric field (E)) which is sensed by the electrodes on the outside (Cushing, 1976). The voltage is then converted to velocities with the vector equation

$$\mathbf{E} = \mathbf{u} \times \mathbf{B} \tag{5.3}$$

For more details the reader is referred to Cushing (1976). The EMV devices of Deltares produce magnetic fields in two directions with according electrodes around the probe. This results in flow velocity measurements in two directions. The E40 probe is fully waterproof so the water depth is not a limitation. The probes have a range up to 2.5 m/s and an accuracy of +/- 0.01 m/s.

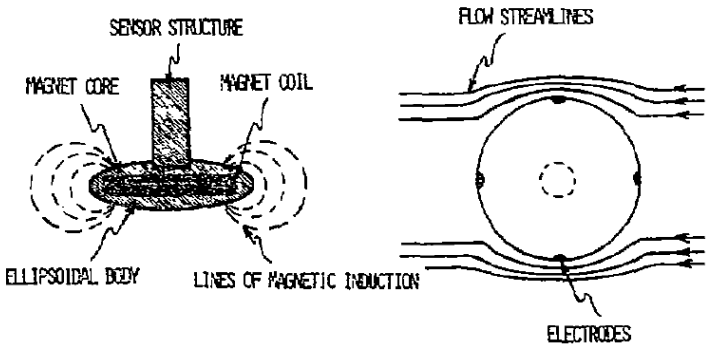

Figure 5.15: Schematization of a flow passing the magnatic field of an EMV (Cushing, 1976).

5.8.3. Sediment concentration and density

The concentration and density of the bed and density current can be determined with several techniques. The principles of these techniques are explained in this section. The densities of the density current were measured with the principle of conductivity. The calibration of the conductivity bars was done with help of a DMA 35. The density and concentration of the bed was determined with oven tests. Sometimes for a quick analysis the pyknometer was used as this techniques only takes a couple of minutes.

Conductivity
The sediment concentration at different heights in the density current is determined with conductivity probes. Conductivity of a material (σ) is the ability to conduct electricity and is given in Siemens per meter (S/m). In a suspension (or medium), σ_m depends on the conductivity of the water (σ_w) in which the solids are suspended and the volume fraction of the solids (Φ_s) and are related as

$$\sigma_m = \sigma_w \cdot (1 - \Phi_s)^n \tag{5.4}$$

with n an empirical constant fitted to the data. A material has a so called resistivity ρ (ρ is used here once to indicate resistivity) against an electrical current flowing through it, with SI unit ohm-meter ($\Omega \cdot m$).

$$\rho = \frac{1}{\sigma} = R\frac{l}{A} \tag{5.5}$$

$$R = \frac{V}{I} \tag{5.6}$$

with R the electrical resistance of a uniform specimen of the material, V the voltage through the material, I the current, l the length of the specimen and A the cross-sectional area of the specimen.

The pore water in the mud is salt, thus has a high conductivity, and is diluted with fresh water. The conductivity of the pore water therefore decreases and so σ_w is not constant. This imposes a problem to Equation 5.4 because now there is one equation with two unknowns. Φ_s cannot be determined from Equation 5.4 directly. In order to still be able to determine the concentration from a single value of σ_m a calibration was made.

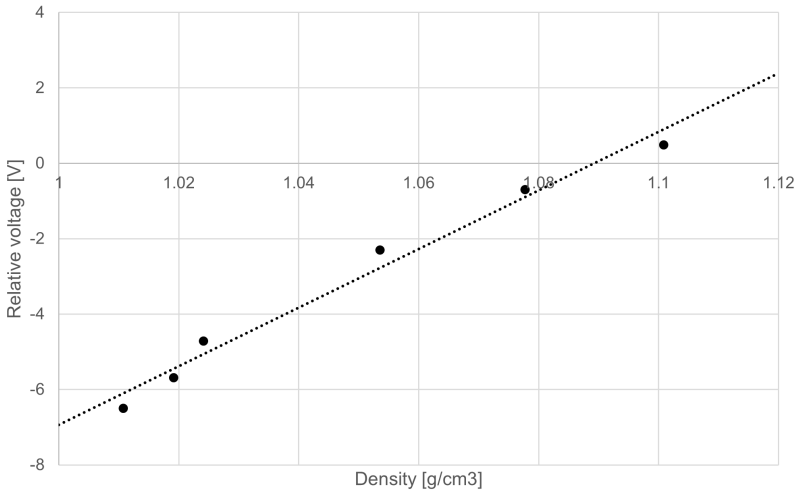

Figure 5.16: Voltage measured as function of the density for the top electrode Chan 10 (see Figure 5.13).

A column of mud was diluted several times with fresh water, after which the conductivity bars were put in and the voltage from the electrodes on the bar was measured. ρ of every dilution series ranges from 1.01 to 1.10 g/cm^3 and was measured with a DMA 35 (from here on ρ is indicated as density again). From this calibration a linear relation was found for ρ of the suspension. The relation of the voltage on the electrode produced by the dilution as a function of ρ for the top electrode of Chan 10 is given in Figure 5.16 as an example. In Appendix B the full calibration can be found in more detail. During the experiments the conductivity bars provide measurements in voltage. These measurements are then later converted to densities and concentrations.
Although the data in Figure 5.16 fits a second degree polynomial better (lower R^2 error), the calibration on the data has to be linear as is done in the figure. A second degree polynomial would flatten out horizontally between 1 and 2 volts but the data from the tests consists of point above 2 volts as well. Applying a second grade polynomial would never reach a large part of the measured data. Applying

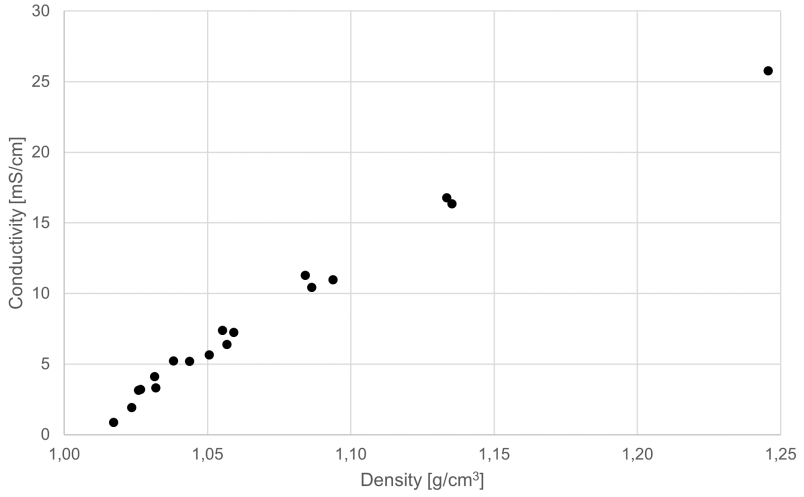

Figure 5.17: The conductivity of dilutions σ_m as a function of its density ρ.

a linear relation does not only fit the range of data, it shows also reasonable results. A second grade polynomial sometimes gave values of ρ_b higher than the density of the original bed as well.

Furthermore, it is usual to find a decrease of conductivity with increasing fluid density (i.e. increase in particle volume fraction), but Figure 5.17 shows an opposite trend in the experimental results. This is due to the fact that the clay that was used in the experiments came from a marine environment with high salinity. Therefore, by mixing the clay in fresh water a large amount of ions came free and led to an increase of electric conductivity.

DMA 35

The Anton Paar DMA 35 is a portable density meter which can be used on all kinds of materials. It is widely used in industry, not only for soils but also oil for example. The device requires only a small amount of sample and can be used in the field (Anton Paar, 2021). A sample of 2 ml is inserted and vibrated. From this vibration the eigen frequency is determined and converted to density. The viscosity of the sample cannot be too large, since the sample needs to sucked into the device. Thick mud therefore cannot be analysed with this device, but suspended mud is possible.

The measuring range is 0 - 3000 g/L with an accuracy of 1 g/L. The standard deviation for repeatability is 0.5 g/L. The big range of concentration of the DMA 35 is useful for this study but for the application of this device, samples need to be taken in-situ as the device cannot measure the suspension directly from the flow. Possible methods for in-situ sampling are discussed in the Section 5.8.4.

Pyknometer test

A pyknometer is a cup with a certain volume with which the density of mud can be determined. The one used for this study is the aluminium pyknometer with a volume of 100 ml. First the weight of the cup is measured and then filled with mud. Then the weight is again measured and the difference in weight is the weight of the soil inside the cup. The density can be determined as

$$\text{density} = \frac{\text{mass}}{\text{volume}} \tag{5.7}$$

This techniques only takes a couple of minutes and is therefore used when a quick analysis needs to be conducted for a thick material (high viscosity).

Oven test

During an oven test an empty cup (ws_c [g]) and a sample of mud in the cup is weighted (ws_s [g]) and dried in an oven for about 15 to 24 hours at a temperature of around 100 °C. During drying all the water evaporates and the dry mud, including the salt from the seawater, is weighted again (ws_D [g]). From the difference of this weight the density [kg/m^3] can be determined as

$$\rho_m = \frac{\rho_w \cdot (1 + c_w)}{\frac{\rho_w}{\rho_s} + c_w} \tag{5.8}$$

with the geo-water content as

$$c_w = \frac{ws_s - ws_d - ws_c}{ws_s} \tag{5.9}$$

and ρ_w the density of the water in the mud (can be salt), ρ_s the density of solids (measured at 2568.3 kg/m^3 for clay particles for the *Beerkanaal* in the Port of Rotterdam (Goda, 2021)). The concentration of solids c [g/L] is determined as

$$c = \frac{1}{\frac{c_w}{\rho_w} + \frac{1}{\rho_s}} \tag{5.10}$$

5.8.4. In-situ sampling

In-situ sampling is favoured in literature (Winterwerp & Van Kesteren (2004); Schulting (1998)) and is considered the most representative method to determine the concentration and density of the density current instead of indirect measuring with e.g. conductivity bars. During in-situ sampling a part of the suspension is brought outside the flow for analyzing. Three well known in-situ sampling methods exist: siphon sampling, bottle sampling and pump sampling (Wren et al., 2000).

Sampling via tubes can be done by means of *siphon sampling*. When the vertical position of sampling in the flow is higher than the end of the tube water flows through the tube to the lower position. Gravity pulls harder from the longer vertical side of the tube simply because it contains more mass. This causes an under-pressure at the top of the tube and thus pulling mass from the smaller vertical side of the tube.

During *bottle sampling* a sample is taken isokinetically by submerging container of an open tube in streamflow, closing it at the two end and removing it from the flow. An advantage of this technique is that, when done accordingly, it gives the best result because the flow is not disturbed during sampling.

During *pump sampling* a sample is pumped via a tube from the flow into a cup. When done right it should give the same result as bottle sampling. A disadvantage is that when pumping too hard too much larger particles are sucked into the tube. When pumping too softly only the smaller particles are pumped into the tubes. Determining what power the pump must apply is very difficult. The pumped flow into the tube most be equal to the outside flow to minimize this effect.

During the tests pump sampling is applied to take samples for the rheology. Siphon sampling would simply not work since the edge of the flume is higher than the bottom and bottle sampling is too complicated. For density measurements conductivity bars are preferred since they provide continuous measurements.

5.8.5. Bathymetry

To measure the bathymetry of the bed, two techniques are used: echo sounding and disk measuring. The principle of the these two techniques and its accuracy and limitations is described in this section.

Echo sounding

To measure the bathymetry a duo frequency echo sounder from the Port of Rotterdam is attached to the cart above the flume right behind the jetbar at a distance of 1.40 meters. This duo frequency echo sounder emits an acoustic signal with a frequency of 38 and 200 kHz which reflect at the interface of large gradients of density in the bed. The time it takes for the signal to emit and reflect back is combined with the speed of sound in water to determine the relative distance of the bed from the echo sounder. The high frequency cannot penetrate the mud and reflects back on the top of the soft layer. The low frequency penetrates the top layer up to a depth where the mud becomes 1200 kg/m^3 in density.

The duo frequency echo sounder provides a single point measurement in time. Using the known traverse velocity of the carriage of the water-soil flume, a 2D profile can be constructed and analysed. The

difference in depth from these profiles gives the production of WID. The accuracy of the echo sounder is 1 cm and needs a minimal water depth of 1 meter.

The speed of sound in water (c_s) is dependent on the temperature of the water (T) in °C, the salinity (s_s) in ‰ and the water depth (d_w) in m.

$$c_s = 1449.2 + 4.6T - 0.055T^2 + 0.00029T^3 + (1.34 - 0.01T)(s_s - 35) + 0.016d_w \quad (5.11)$$

It is assumed that the salinity at the beginning of a test is zero and does not change much during a test because the salt water remains closely to the bottom of the flume and ends up behind the ramp. d_w is set to 2 meters. T is measured before the start of each test and c_s is calculated as input value for the echo sounder.

Submersible disk

Besides echo sounding, the depth of the flume is measured with a submersible disk. This disk has the shape of a diamond and penetrates the mud up to its maximal diameter D_{max} (= 200 mm, see Figure 5.18 (left)). It is made of PVC and has a density of 1.5 g/cm^3. The height of the disk is 100 mm and the height from its maximal diameter to the top is 50 mm. Measuring the length of the rope from a certain reference point (top of the wall of the flume) plus 50 mm provides the vertical position of the top of the sediment layer.

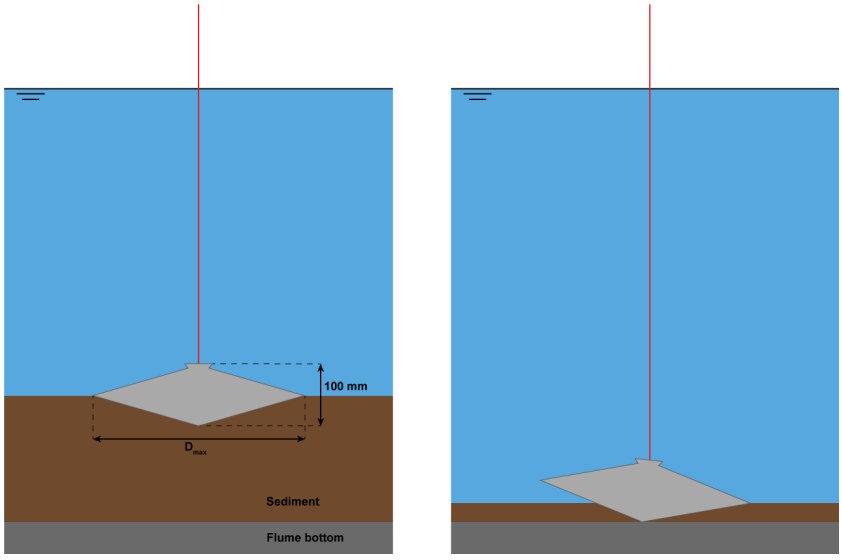

Figure 5.18: The principle of using a disk for depth measurement (left) and the situation when the layer of sediment is thinner than the height of the disk (right).

A disadvantage of this technique appears when the thickness of the sediment layer is thinner than 50 mm (see Figure 5.18 (right)). The disk will rotate a little and cannot provide an accurate measurement anymore. So, when the length of the rope + 50 mm is more than the actual depth of the flume, the measurement is not accurate anymore and it can only be said that the thickness of the layer is smaller than 50 mm.

5.8.6. Pressure and discharge

During the experiments, the pressure in the jetbar and the discharge in the pipes, that supply the jetbar with water, are measured. The measuring positions are schematized in Figure 5.10. Measuring the pressure and discharge provides insight into fluctuations and correctness of both parameters during a test.

The pressure transmitters installed on the jetbar transmit an electrical signal to a computer where the signal is converted to a pressure value. A calibration is not needed. The transmitters can measure a pressure up to 5 bar with an accuracy up to 0.001 bar. The measured pressure is used to set the pumps in the secondary basin to the right frequency and thus discharge.

The discharge is measured with electromagnetic flowmeters which work with the same principle as the EMV's explained in Section 5.8.2. The flow velocity u is now integrated over the area of the tube which provides the discharge.

5.8.7. Rheology

The rheological properties of the density current and the undisturbed bed that need to be determined are the yield stress and viscosity. The principles and basics of rheology are given in Section 4.2. In this section it is explained how rheology can be measured. The properties are determined with a controlled shear rate test in the HAAKE™ MARS™ Rheometer of Thermo Fisher Scientific. In this device, a stationary cup is filled with mud and a geometry is placed in it and rotates with a certain shear rate (Figure 5.19). Between the geometry and the cup, a thin layer of mud is being sheared and applies a counter acting force on the geometry because of its viscous behaviour. The torque on the geometry is measured and converted as shear stress. The software of the rheometer then plots the shear rate as a function of the shear stress. This results in a characteristic flow curve from which the rheological properties can be determined.

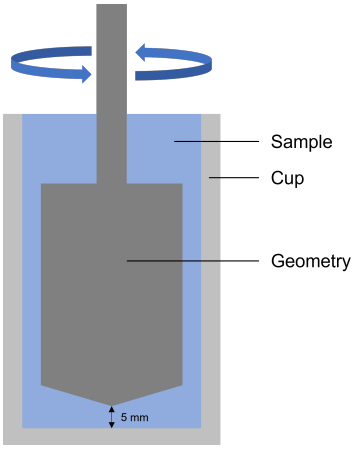

Figure 5.19: Rheometer setup with a cup and geometry. A BOB geometry is used here as example, although used many times during this study.

The type and quality of the flow curve depends on the geometry used. There are many geometries but only two were used during this study: the BOB- and vane geometry (element code: CC25 DIN and FL22 respectively, see Figure 5.20). The BOB geometry is used for high and low viscosity liquids, whereas a vane geometry can only be used for relative high viscosities. When a vane geometry is used in a material of low viscosity, turbulence between the blades of the vane can occur and disturb the measurements. A BOB geometry works for low viscosities because the distance between the geometry and the cup is very small (only a couple of mm) and produces a laminar flow in this small space. A disadvantage is that wall-slip may occur during shearing. A vane does not produce wall-slip and is therefore more accurate.

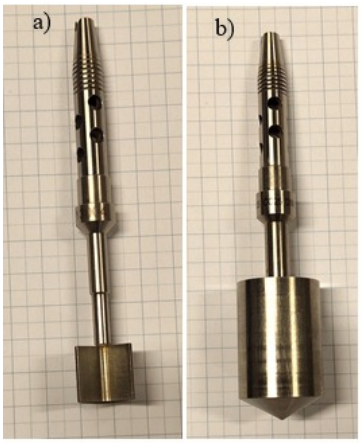

Figure 5.20: a) vane and b) bob geometry for the HAAKE™ MARS™ Rheometer (Goda, 2021)

6 | Test results

This chapter presents the results from the experimental setup described in Chapter 5. Section 6.1 presents the results from the trial week containing conclusions which are relevant to the actual tests. Sections 6.2 to 6.7 present the results of every test and starts with the jet settings of each run and end with the results combined with some preliminary observations. Section 6.8 presents an overview of all jet settings combined with the results. An elaboration on this chapter is given in Appendix C.

6.1. Trial week

The first week of the experiments was used to test the setup as described in Chapter 5. During this week, 5 runs were done to see what the influence was of different D_n and p_j on the production. The settings of each run are given in Table 6.1. Q_t is the total discharge measured at the pumps and Q_j is the jet discharge, i.e. Q_t divided by the number of nozzles used. The results from these runs are given in Table 6.2. $I_{j,t}$ is the total momentum coming from the jetbar and I_j is the momentum from the jetbar per meter width. μ is the contraction coefficient of the nozzles and SOD_r is the SOD relative to the crest of the ramp.

Properties of the mud:		
τ_B	109	Pa
ρ_b	1302	kg/m^3
c_m	489.5	g/L

τ_B is measured in the rheometer of Deltares with a BOB-geometry (element code: CC25 DIN). The rheocurves are given in Appendix C. ρ_b and c_m are the density and concentration of mass of the bed respectively and are determined with an oven test. These measuring methods for the properties of the mud are applied during every test.

		Run 1	**Run 2**	**Run 3**	**Run 4**	**Run 5**
Date		23-6-2021	23-6-2021	24-6-2021	24-6-2021	25-6-2021
Time		12:32:00	15:41:00	12:13:00	15:58:00	09:25:00
v_t	m/s	0.25	0.25	0.25	0.25	0.25
SOD_r	mm	10	10	10	10	10
D_n	mm	20	20	20	30	30
p_j	bar	0.54	1.07	1.06	0.49	1.03
Q_t	L/s	7.38	11.63	10.74	13.84	24.03
Q_j	L/s	1.85	2.91	2.69	3.46	6.01

Table 6.1: Measured parameters for each run in trial week.

		Run 1	**Run 2**	**Run 3**	**Run 4**	**Run 5**
s_{intr} (echo sounder)	m	0.03	0.06	0.06	0.09	0.11
s_{intr} (disk)	m	0.03	0.06	0.11	0.09	0.12
μ	-	0.563	0.632	0.586	0.490	0.591
$I_{j,t}$	N	76.89	170.41	156.73	138.18	345.23
I_j	N/m	192.22	426.04	391.84	345.46	863.08
Production	kg/s	9.39	18.87	18.87	28.31	34.57
Production	kg/s/m	3.75	7.54	7.54	11.32	13.82

Table 6.2: Results for each run in trial week.

During run 4 and 5, $s_{intr} \approx 10$ cm was reached for both 0.5 and 1 bar. From this it is concluded that D_n = 30 mm is needed for the following tests.

6.2. Test 1

The objective of the first test is to apply v_t = 0.25 m/s, p_j = 0.5 bar and SOD = 0 m. The properties of the mud are:

τ_B	118.2	Pa
ρ_b	1294	kg/m^3
c_m	448	g/L
d_{init}	0.57	m

d_{init} is the initial thickness of the mud bed at the beginning of a test and is measured with a ruler by hand in a dry flume. Table 6.3 presents the settings for each run. D_n is 35 mm due to a mistake made in the process of drilling the nozzles. The date is given in DD:MM:YY and the time is given in HH:MM:SS. h_{ramp} is the height of the ramp at the beginning of the run. The ramp is lowered after every run to align the measuring frame at the new level of the bed and is in proportion to s_{intr} from Table 6.4. SOD$_b$ is the relative SOD to the level of the bed of mud. An explanation for the distinction between SOD$_r$ and SOD$_b$ and visualization of the results is given in Appendix C. SOD$_b$ can be negative, which means that the jetbar is lower than the level of the bed and the jetbar is thus ploughing through the mud. Finally, Δh_c is the relative vertical distance between the probes of the conductivity bars behind the jetbar and those at the ramp. The probes at the ramp are the point of reference for this relative vertical distance and Δh_c is positive upwards.

		Run 1	**Run 2**	**Run 3**
Date		29-6-2021	29-6-2021	30-6-2021
Time		10:21:00	14:07:00	10:18:00
v_t	m/s	0.25	0.25	0.25
SOD$_r$	mm	10	10	50
SOD$_b$	mm	-60	-60	10
D_n	mm	35	35	35
Q_t	L/s	134	136	135
μ	-	0.58	0.59	0.57
p_j (left)	bar	0.50	0.48	0.52
p_j (right)	bar	0.51	0.52	0.53
h_{ramp}	m	0.50	0.40	0.25
Δh_c	mm	0	0	30
I_j	N/m	566.3	575.4	579.7

Table 6.3: (Measured) parameters during the runs of test 1.

Table 6.4 presents the intrusion and production results at different positions in the flume. During test 1 at five locations relative to the ramp, the bed level was measured with the disk after each run. The difference between these bed level measurements provides s_{intr} as given in the table. The location between which the difference is small is where the jetbar created a stationary situation during the jetting process. Between these points the average is determined and is characterized as the *average representative intrusion depth* ($s_{av,intr}$). For each test, it is determined what stretch of the flume is used to determine $s_{av,intr}$. The values used for $s_{av,intr}$ are marked in brown. A visualization and elaboration of these results are given in Appendix C.

	s$_{intr}$ at 5 m	**s$_{intr}$ at 10 m**	**s$_{intr}$ at 15 m**	**s$_{intr}$ at 20 m**	**s$_{intr}$ at 25 m**	**s$_{av,intr}$**	**Production**
Run 1	0.03 m	0.10 m	0.11 m	0.22 m	0.09 m	0.08 m	20.16 kg/s
Run 2	0.17 m	0.17 m	0.22 m	0.12 m	0.02 m	0.17 m	44.35 kg/s
Run 3	0.24 m	0.30 m	0.24 m	0.21 m	0.22 m	0.24 m	64.51 kg/s

Table 6.4: s_{intr} at different positions along the length of the flume together with $s_{av,intr}$ and corresponding production for test 1.

Figure 6.1 to 6.3 show the averaged horizontal flow velocity above the ramp and density profiles at the ramp and behind the jetbar. The time series and stretch over which is averaged are given in Appendix

C. The density profiles at the ramp and behind the jetbar are corrected for Δh_c if necessary. The height of the velocity profiles increases with ascending runs, while the maximum velocity is in the same order of magnitude. The density profile at the ramp becomes more homogeneously distributed over the height above the bed and decreases in magnitude with ascending runs.

Furthermore, the upper edge of the velocity profile follows the location of the upper edge of the density profile behind the jetbar instead of the upper edge of the density profile measured at the ramp. Especially for runs 2 and 3, the upper edge of the density profile measured at the ramp is higher than the upper edge of the density profile behind the jetbar.

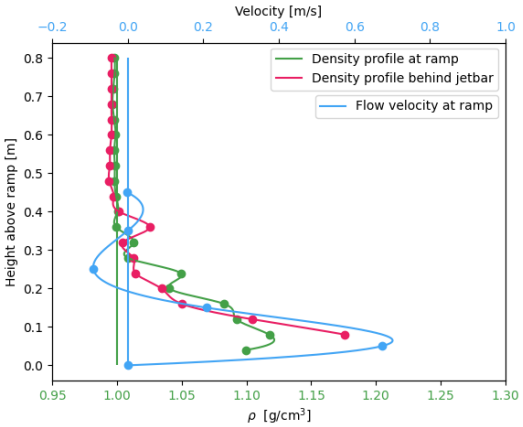

Figure 6.1: Flow velocity and density profiles for test 1 run 1.

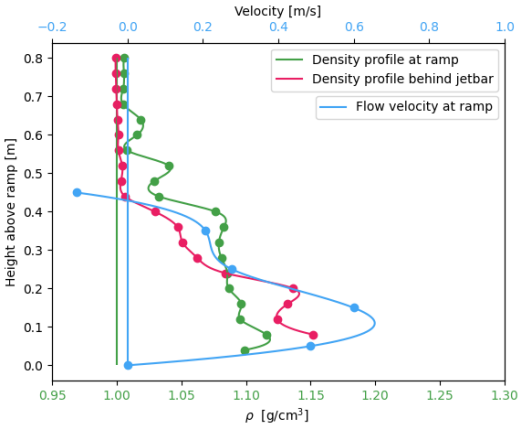

Figure 6.2: Flow velocity and density profiles for test 1 run 2.

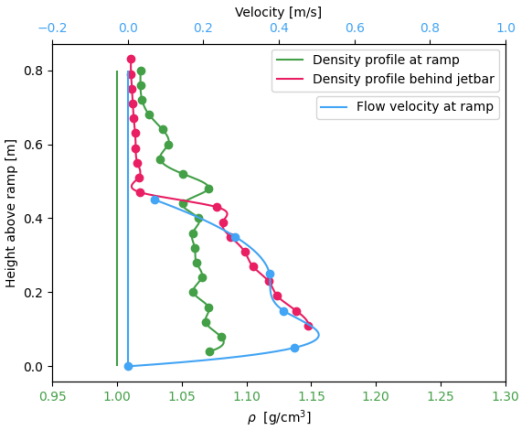

Figure 6.3: Flow velocity and density profiles for test 1 run 3.

6.3. Test 2

The objective of the second test is to see the influence of v_t (= 0.40 m/s) in comparison to test 1. p_j (= 0.5 bar) and SOD (= 70 m) are kept the same. The properties of the mud are:

τ_B	80.15	Pa
ρ_b	1282	kg/m^3
c_m	426	g/L
d_{init}	0.44	m

and settings during each run:

		Run 1	Run 2
Date		6-7-2021	6-7-2021
Time		14:16:00	16:11:00
v_t	m/s	0.40	0.40
D_n	mm	35	35
SOD$_r$	mm	70	70
SOD$_b$	mm	70	140
Q_t	L/s	133	134
μ	-	0.58	0.58
p_j (left)	bar	0.4817	0.4805
p_j (right)	bar	0.5101	0.5033
h_{ramp}	m	0.45	0.30
Δh_c	mm	70	70
I_j	N/m	559.7	560.2

Table 6.5: (Measured) parameters during the runs of test 2.

Table 6.6 presents the intrusion and production results of this test.

	s_{intr} at 5 m	s_{intr} at 10 m	s_{intr} at 15 m	s_{intr} at 20 m	s_{intr} at 25 m	$s_{av,intr}$	Production
Run 1	0.21 m	0.29 m	0.34 m	0.26 m	0.07 m	0.21 m	85.88 kg/s
Run 2	0.16 m	0.14 m	0.07 m	0.10 m	0.07 m	0.16 m	65.43 kg/s

Table 6.6: s_{intr} at different positions along the length of the flume together with $s_{av,intr}$ and corresponding production for test 2.

The measured profiles in Figure 6.4 and 6.5 for runs 1 and 2 respectively show that the density profile at the ramp increases in height and decreases in magnitude as was seen during test 1 as well. Also,

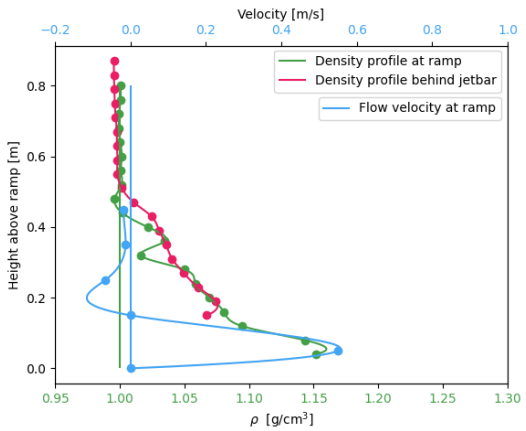

Figure 6.4: Flow velocity and density profiles for test 2 run 1.

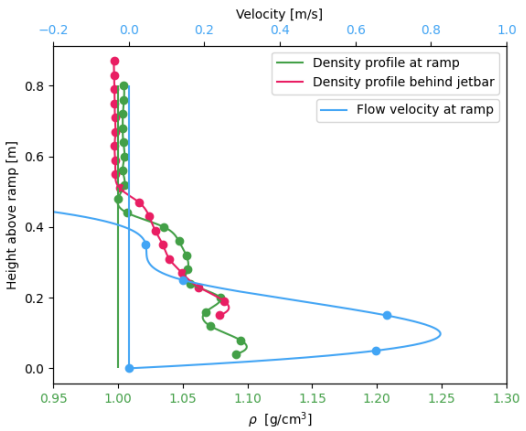

Figure 6.5: Flow velocity and density profiles for test 2 run 2.

the velocity profile increases in both properties but an increase in magnitude was not observed during test 1. The density profiles at the ramp and behind the jetbar are more or less the same in height and magnitude. The upper edge of the velocity profiles is now much lower than the upper edges of both density profiles.

6.4. Test 3

The objective of the third test is to apply D_n = 20 mm in order to decrease I_j. v_t = 0.40 m/s, p_j = 1 bar and SOD = 0. The properties of the mud are:

τ_B	156	Pa
ρ_b	1307	kg/m^3
c_m	468	g/L
d_{init}	0.51	m

and settings during each run:

		Run 1	**Run 2**	**Run 3**	**Run 4**
Date		9-7-2021	9-7-2021	9-7-2021	9-7-2021
Time		09:58:00	11:24:00	13:34:00	14:56:00
v_t	m/s	0.40	0.40	0.40	0.40
D_n	mm	20	20	20	20
SOD$_r$	mm	10	10	10	60
SOD$_b$	mm	-10	0	-30	60
Q_t	L/s	70	69	91	93
μ	-	0.64	0.64	0.85	0.87
p_j (left)	bar	1.02	1.04	0.98	0.99
p_j (right)	bar	1.06	1.05	1.03	1.02
h_{ramp}	m	0.50	0.45	0.35	0.20
Δh_c	mm	0	0	0	30
I_j	N/m	424.6	415.8	423.8	423.5

Table 6.7: (Measured) parameters during the runs of test 3.

During runs 3 and 4 a leak appeared in the jetbar which caused the discharge to increase. Table 6.8 presents the intrusion and production results of this test.

	s_{intr} at 5 m	**s_{intr} at 10 m**	**s_{intr} at 15 m**	**s_{intr} at 20 m**	**$s_{av,intr}$**	**Production**
Run 1	0.06 m	0.04 m	0.07 m	0.15 m	0.06 m	25.48 kg/s
Run 2	0.08 m	0.10 m	0.12 m	0.18 m	0.10 m	44.96 kg/s
Run 3	0.19 m	0.17 m	0.17 m	0.16 m	0.18 m	79.42 kg/s
Run 4	0.13 m	0.13 m	0.13 m	0.05 m	0.13 m	58.44 kg/s

Table 6.8: s_{intr} at different positions along the length of the flume together with $s_{av,intr}$ and corresponding production for test 3.

In Figure 6.6 to 6.9 the density current does not move during the first two runs but starts moving during runs 3 and 4. The height of the density profile at the ramp is for run 1 and 2 more or less the same but increases in height when the current starts to move as well during run 3 and 4.

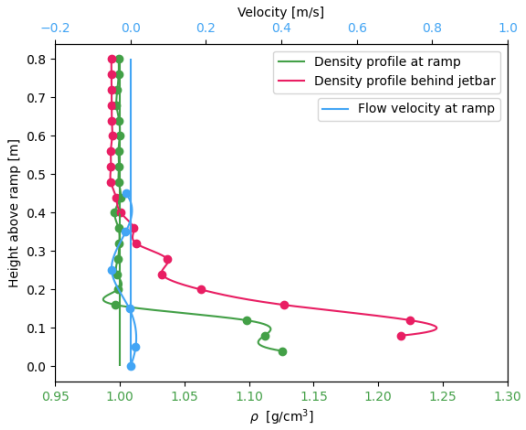

Figure 6.6: Flow velocity and density profiles for test 3 run 1.

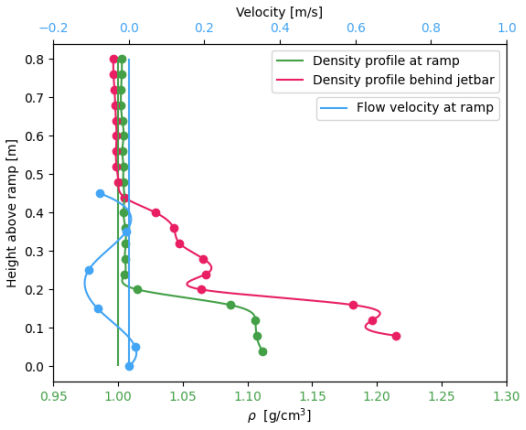

Figure 6.7: Flow velocity and density profiles for test 3 run 2.

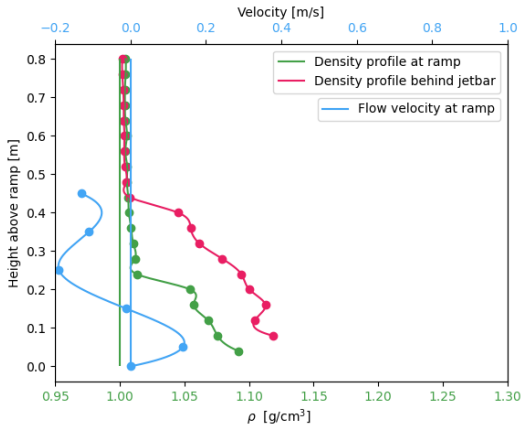

Figure 6.8: Flow velocity and density profiles for test 3 run 3.

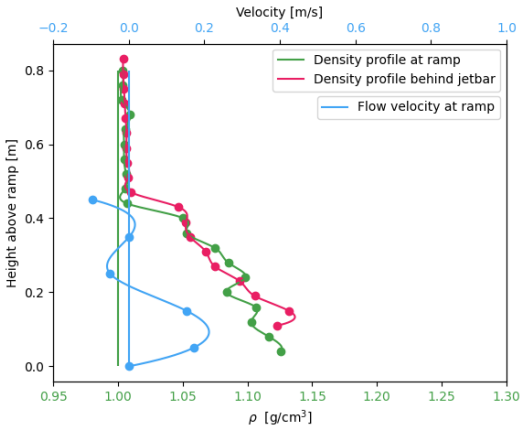

Figure 6.9: Flow velocity and density profiles for test 3 run 4.

6.5. Test 4

The objective of the fourth test is to vary with v_t (= 0.25 m/s) in comparison to test 3. p_j = 1 bar, D_n = 20 mm and SOD = 0. The properties of the mud are:

τ_B	237.2	Pa
ρ_b	1334	kg/m^3
c_m	514	g/L
d_{init}	0.57	m

and settings during each run:

		Run 1	Run 2	Run 3
Date		14-7-2021	14-7-2021	14-7-2021
Time		11:17:00	11:44:00	14:50:00
v_t	m/s	0.25	0.25	0.25
D_n	mm	20	20	20
SOD$_r$	mm	10	10	10
SOD$_b$	mm	-60	-50	20
Q_t	L/s	223.7	69.4	69
μ	-	2.10	0.65	0.65
p_j (left)	bar	1.01	1.03	1.03
p_j (right)	bar	1.02	1.04	1.02
h_{ramp}	m	0.50	0.45	0.35
Δh_c	mm	0	0	0
I_j	N/m	410.5	416.4	410.6

Table 6.9: (Measured) parameters during the runs of test 4.

Q_t of run 1 is affected by an error in the measuring equipment and is during the analysis corrected to the values of runs 2 and 3. I_j is here already corrected for a realistic value of Q_t (69 L/s). Table 6.10 presents the intrusion and production results of this test.

	s_{intr} at 5 m	s_{intr} at 10 m	s_{intr} at 15 m	s_{intr} at 20 m	$s_{av,intr}$	Production
Run 1	0.06 m	0.07 m	0.06 m	0.07 m	0.06 m	19.50 kg/s
Run 2	0.14 m	0.16 m	0.13 m	0.22 m	0.14 m	44.20 kg/s
Run 3	0.18 m	0.17 m	0.16 m	0.10 m	0.17 m	52.43 kg/s

Table 6.10: s_{intr} at different positions along the length of the flume together with $s_{av,intr}$ and corresponding production for test 4.

In Figure 6.10 to 6.12 a flow starts to occur only from run 3. This was the case for test 3 as well which had a I_j in the same order of magnitude. The density profiles at the ramp are for runs 1 and 2 more or less the same but decrease in height and increase in magnitude for run 3. The density profiles behind the jetbar mainly decrease in magnitude with ascending runs. The density profiles behind the jetbar show very high values, even higher than the density of the bed. This is of course not possible, but an explanation could not be found, unfortunately. The big difference in density between the ramp and the jetbar could indicate that a lot of sediment has settled before reaching the ramp.

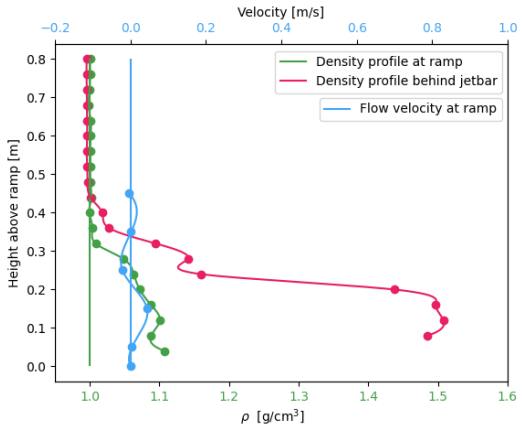

Figure 6.10: Flow velocity and density profiles for test 4 run 1.

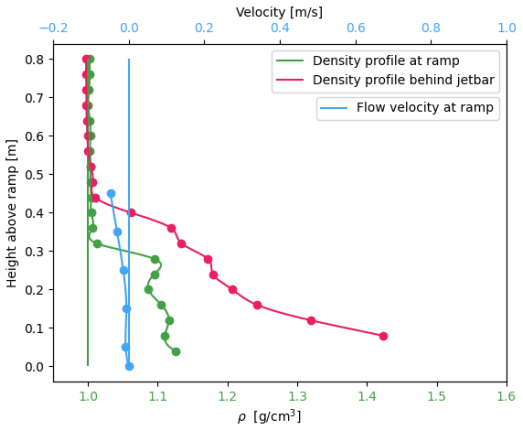

Figure 6.11: Flow velocity and density profiles for test 4 run 2.

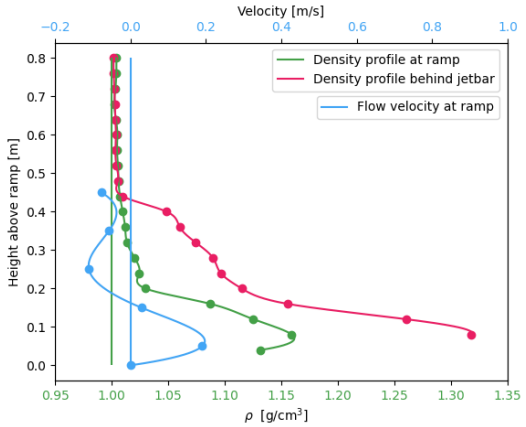

Figure 6.12: Flow velocity and density profiles for test 4 run 3.

6.6. Test 5

The objective of the fifth test is to see the influence of p_j (= 0.5 bar) in comparison to test 4. v_t = 0.25 m/s, D_n = 20 mm and SOD = 0 m. The properties of the mud are:

τ_B	132.7	Pa
ρ_b	1295	kg/m^3
c_m	448	g/L
d_{init}	0.52	m

and settings during each run:

		Run 1	Run 2	Run 3	Run 4
Date		19-7-2021	19-7-2021	19-7-2021	19-7-2021
Time		11:21:00	13:26:00	14:51:00	15:50:00
v_t	m/s	0.25	0.25	0.25	0.25
D_n	mm	20	20	20	20
SOD$_r$	mm	10	10	10	60
SOD$_b$	mm	-10	-20	-50	10
Q_t	L/s	223.5	52	53	51.5
μ	-	2.99	0.69	0.70	0.69
p_j (left)	bar	0.50	0.51	0.51	0.50
p_j (right)	bar	0.50	0.51	0.51	0.50
h_{ramp}	m	0.50	0.45	0.35	0.30
Δh_c	mm	0	0	0	30
I_j	N/m	217.1	219.7	223.2	214.2

Table 6.11: (Measured) parameters during the runs of test 5.

Again, a calibration error occurred in the discharge meter during run 1. The other results from run 1 were corrected for the right discharge (52 L/s). Table 6.12 presents the intrusion and production results of this test.

	s_{intr} at 5 m	s_{intr} at 10 m	s_{intr} at 15 m	s_{intr} at 20 m	$s_{av,intr}$	Production
Run 1	0.05 m	0.04 m	0.03 m	0.04 m	0.05 m	12.09 kg/s
Run 2	0.07 m	0.07 m	0.04 m	0.17 m	0.07 m	18.82 kg/s
Run 3	0.06 m	0.06 m	0.06 m	0.07 m	0.06 m	16.13 kg/s
Run 4	0.10 m	0.10 m	0.04 m	0.13 m	0.10 m	26.88 kg/s

Table 6.12: s_{intr} at different positions along the length of the flume together with $s_{av,intr}$ and corresponding production for test 5.

In Figure 6.13 to 6.16 no horizontal transport occurs during any run, but solely fluidization of mud from the density profiles is observed. I_j is also the lowest of all tests. Still, an increase in height and magnitude is observed in the density profiles at the ramp for the first three runs. The height of the density profiles behind the jetbar increases slightly with ascending runs but the magnitude increases. The density of run 3 behind the jetbar is much larger than the initial density of the bed, but again no explanation was found.

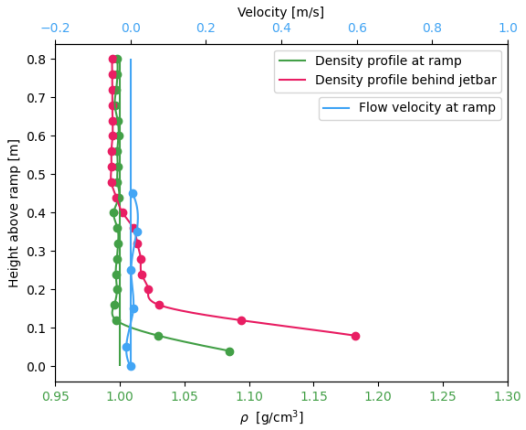

Figure 6.13: Flow velocity and density profiles for test 5 run 1.

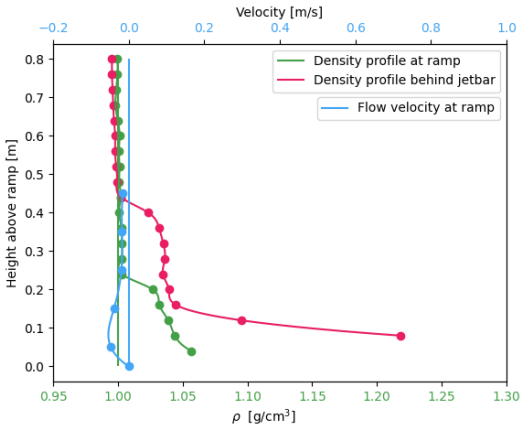

Figure 6.14: Flow velocity and density profiles for test 5 run 2.

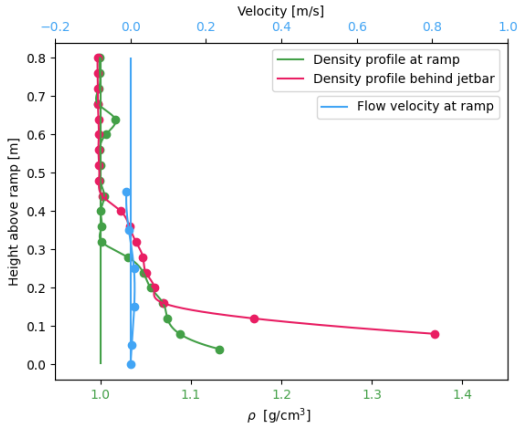

Figure 6.15: Flow velocity and density profiles for test 5 run 3.

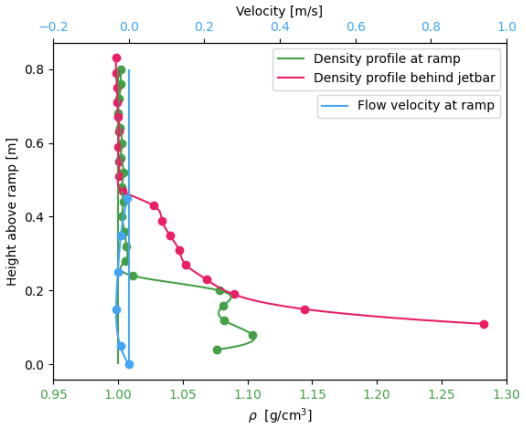

Figure 6.16: Flow velocity and density profiles for test 5 run 4.

6.7. Test 6

The objective of the sixth test is to see the influence of the SOD_r (= 300 mm). v_t = 0.25 m/s, D_n = 20 mm and p_j = 1 bar. The properties of the mud are:

τ_B	112.2	Pa
ρ_b	1293	kg/m^3
c_m	444	g/L
d_{init}	0.58	m

and settings during each run:

		Run 1	Run 2	Run 3	Run 4
Date		22-7-2021	22-7-2021	22-7-2021	22-7-2021
Time		09:40:00	11:40:00	13:45:00	15:32:00
v_t	m/s	0.25	0.25	0.25	0.25
D_n	mm	20	20	20	20
SOD_r	mm	300	300	60	300
SOD_b	mm	220	230	-40	260
Q_t	L/s	68.16	72.14	73.43	76.33
μ	-	0.64	0.66	0.67	0.71
p_j (left)	bar	0.99	1.04	1.06	1.04
p_j (right)	bar	1.00	1.06	1.06	1.04
h_{ramp}	m	0.50	0.45	0.35	0.20
Δh_c	mm	0	0	0	0
I_j	N/m	401.6	437.7	446.2	458.7

Table 6.13: (Measured) parameters during the runs of test 6.

Table 6.14 presents the intrusion and production results of this test. From $s_{av,intr}$ it is observed that a relative small SOD_r provides a relatively large production.

	s_{intr} at 5 m	s_{intr} at 10 m	s_{intr} at 15 m	s_{intr} at 20 m	$s_{av,intr}$	Production
Run 1	0.04 m	0.06 m	0.06 m	0.35 m	0.05 m	13.32 kg/s
Run 2	0.07 m	0.08 m	0.10 m	0.16 m	0.08 m	19.98 kg/s
Run 3	0.21 m	0.22 m	0.38 m	0 m	0.22 m	57.28 kg/s
Run 4	0.16 m	0.15 m	0.04 m	0.04 m	0.16 m	41.29 kg/s

Table 6.14: s_{intr} at different positions along the length of the flume together with $s_{av,intr}$ and corresponding production for test 6.

Figure 6.17 to 6.20 show that for a SOD_r of 300 mm sediment is suspended high in the water column relative to a SOD_r of 60 mm at the ramp. The velocity profile shows for a SOD_r of 300 mm a higher velocity profile at the ramp relative to a SOD_r of 60 mm as well. During run 3 the magnitude of the density profiles increases in comparison to runs 1 and 2. A SOD_r of 60 mm fluidizes more sediment resulting in larger densities near the bed. A SOD_r of 300 mm however causes more horizontal transport caused by the thicker layer (~0.3 - 0.5 m) of moving fluid mud at a rather low velocity of 0.2 m/s. Tests with I_j in the same order of magnitude and a SOD_r of ~0 mm show a flow from runs 3 and 4 onwards but during this test, a SOD_r of 300 mm creates a flow from run 1 already.

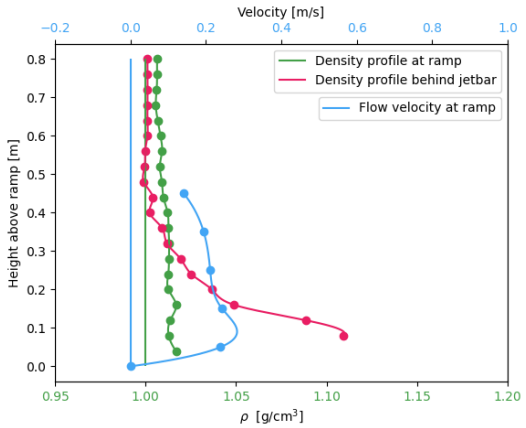

Figure 6.17: Flow velocity and density profiles for test 6 run 1. SOD_r = 300 mm.

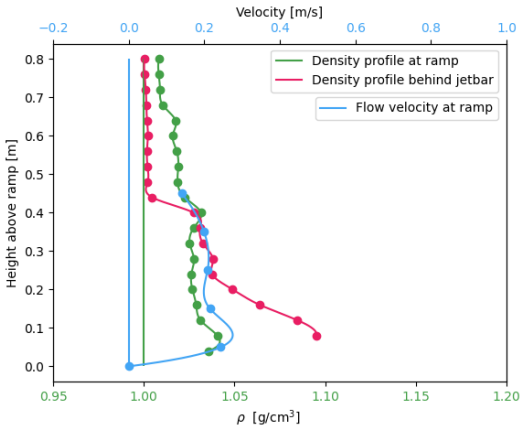

Figure 6.18: Flow velocity and density profiles for test 6 run 2. SOD_r = 300 mm.

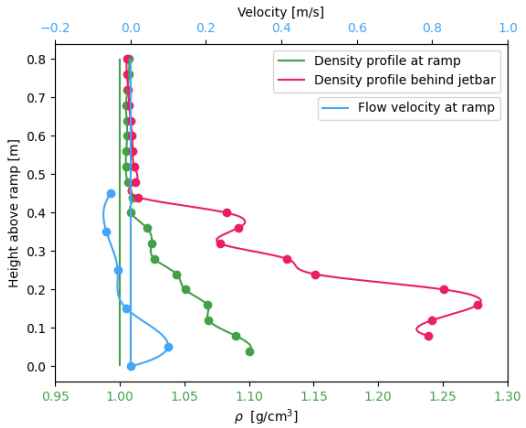

Figure 6.19: Flow velocity and density profiles for test 6 run 3. SOD_r = 60 mm.

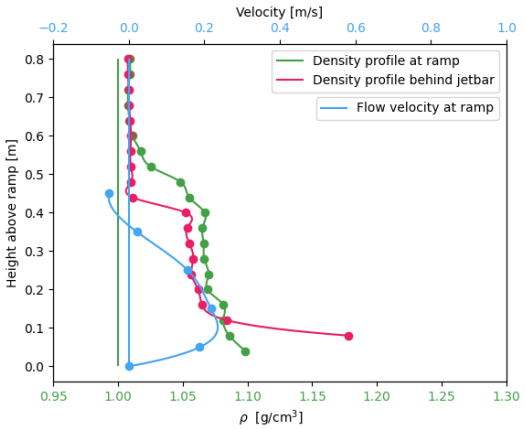

Figure 6.20: Flow velocity and density profiles for test 6 run 4. SOD_r = 300 mm.

6.8. Summary of test results

The table below provides a summary of the actual settings used during the tests and is a revision of the textmatrix given in Table 5.3. The values of p_j are from the right side of the jetbar.

		v_t [m/s]	D_n [mm]	p_j [bar]	SOD$_r$ [mm]	SOD$_b$ [mm]	τ_B [Pa]	I_j [N/m]	$s_{av,intr}$ [m]	Production [kg/s]
Trial	Run 1	0.25	20	0.54	10	-	109	192.22	0.03	9.39
week	Run 2	0.25	20	1.07	10	-	109	426.04	0.06	18.87
	Run 3	0.25	20	1.06	10	-	109	391.84	0.06	18.87
	Run 4	0.25	30	0.49	10	-	109	345.46	0.09	28.31
	Run 5	0.25	30	1.03	10	-	109	863.08	0.11	34.57
Test 1	Run 1	0.25	35	0.51	10	-60	118.2	566.3	0.08	20.16
	Run 2	0.25	35	0.52	10	-60	118.2	575.4	0.17	44.35
	Run 3	0.25	35	0.53	50	10	118.2	579.7	0.24	64.51
Test 2	Run 1	0.40	35	0.51	70	70	80.15	559.7	0.21	85.88
	Run 2	0.40	35	0.50	70	140	80.15	560.2	0.16	65.43
Test 3	Run 1	0.40	20	1.06	10	-10	156	424.6	0.06	25.48
	Run 2	0.40	20	1.05	10	0	156	415.8	0.10	44.96
	Run 3	0.40	20	1.03	10	-30	156	423.8	0.18	79.42
	Run 4	0.40	20	1.02	60	60	156	423.5	0.13	58.44
Test 4	Run 1	0.25	20	1.02	10	-60	237.2	410.5	0.06	19.53
	Run 2	0.25	20	1.04	10	-50	237.2	416.4	0.14	44.20
	Run 3	0.25	20	1.02	10	20	237.2	410.6	0.17	52.43
Test 5	Run 1	0.25	20	0.50	10	-10	132.7	217.1	0.05	12.10
	Run 2	0.25	20	0.51	10	-20	132.7	219.7	0.07	18.82
	Run 3	0.25	20	0.51	10	-50	132.7	223.2	0.06	16.13
	Run 4	0.25	20	0.50	60	10	132.7	214.2	0.10	26.88
Test 6	Run 1	0.40	20	1.00	300	220	112.2	399.6	0.05	13.32
	Run 2	0.40	20	1.06	300	230	112.2	433.5	0.08	19.98
	Run 3	0.40	20	1.06	60	-40	112.2	446.2	0.22	57.28
	Run 4	0.40	20	1.04	300	260	112.2	458.7	0.16	41.29

Table 6.15: Summary of all the test results.

An important notion regarding the interpretation of the data is the resolution of the velocity profiles. At five points of different heights above the ramp, the flow velocity is measured with a distance of 10 cm between every probe. The lowest data point is manually added and is always zero. Then a line is drawn through these points and shows a bell-shaped curve as is often schematized in literature (van Rijn (n.d.); Middleton (1993); Winterwerp & Van Kesteren (2004)). This is done to make visual interpretation to the reader more inelaborate but can give a false idea of the flow of the density current since it is not necessarily true that the measured data point of maximum velocity is also the real maximum. The maximum can be below or above this point as well. It is also not known whether the lowest point is truly zero. This can be a false assumption when a hydraulic smooth bed is assumed as well.

Furthermore, this study failed to collect samples from the density current to analyse its rheology. The technique with a pumping system and tubes did not have enough power to transport sediment out of the flume, unfortunately.

7 | Analysis

This chapter provides an analysis of the findings of the test results (Chapter 6). The focus of the analysis is on the rheology (7.1), production rate (7.2), density current dynamics (7.3) and SOD (7.4).

7.1. Rheology

The rheological properties of mud used during the experiments τ_B and ρ_b from Chapter 6 (test 1 to 6) and from Table 5.5 (*salt versus fresh water dilutions*) are compared to the findings of Ten Brummelhuis (2021). Ten Brummelhuis conducted rheological experiments on the same mud and fitted the Bingham models of Thomas and Jacobs & Van Kesteren to his data. In Figure 7.1 these Bingham models together with the data of Ten Brummelhuis and the data of the experiments of this study are plotted. The data from this study falls on the same trends as found by Ten Brummelhuis. However, the data of the experiments cannot be attributed solely to the trends for fresh or salt water dilution. For the equations and parameters of the Bingham models the reader is referred to Ten Brummelhuis (2021).

The experimental data contains one clear outlier outside the trends of Thomas and Jacobs & Van Kesteren. This is the undiluted data point in Table 5.5. This data point was collected on undiluted mud which was dredged in December 2020 in the Calandkanaal and had been in contact with air several times, whereas the mud utilised for the WID tests was collected as of June 2021. It may well be possible that organic matter has been degraded and therefore changed its rheological properties. When diluted, the expected behaviour is seen again as illustrated by the corresponding, lower-lying data points concerning this outlier. Another possible reason why this point does not fit the curves is that its density is measured with a pyknometer, which can be quite inaccurate.

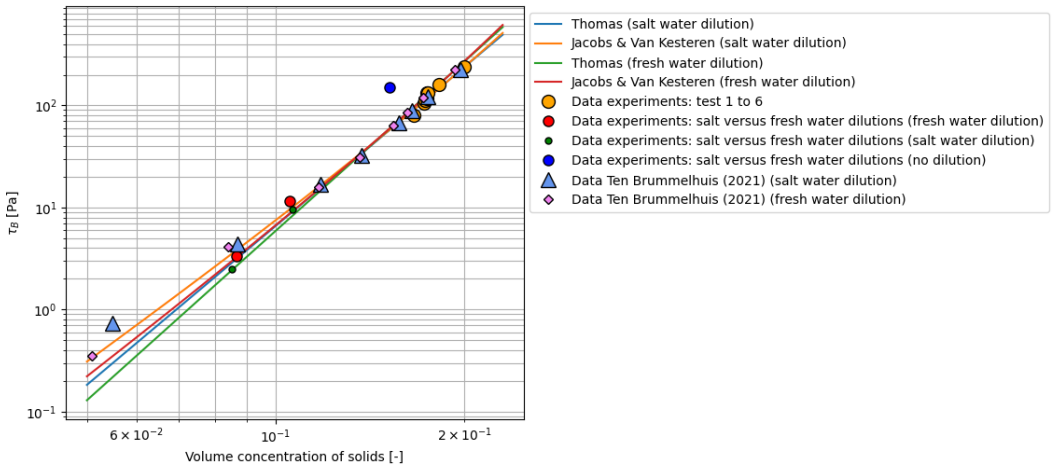

Figure 7.1: Experimental data plotted against findings of Ten Brummelhuis (2021).

In Figure 7.2 the experimental data and the data of Ten Brummelhuis (2021) is plotted as a function of the density to make conversion of density and yield stress easier and to visualize the decay in yield stress for high and low-density differences. The formula corresponding solely to the experimental data is

$$\tau_B = 1 \cdot 10^{-10} \cdot e^{0.0213\rho} \tag{7.1}$$

and is plotted as well. The data of Ten Brummelhuis (2021) is added to compare the results of both studies. The data of the two studies fit Equation 7.1 quite close.

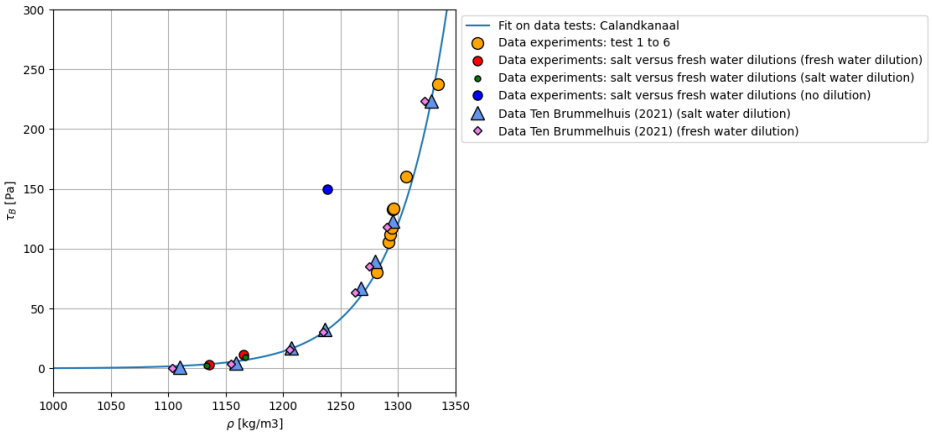

Figure 7.2: τ_B as a function of ρ of mud from the Calandkanaal in the Port of Rotterdam.

7.2. Production rate

From here on, a distinction is made between *initial production* (P_i), which is the amount of sediment stirred up by the jets, and *actual production* (P_a), which is the amount of sediment eventually transported by the density current. The production as determined in the previous chapter is initial production, which is derived solely from s_{intr}, v_t and ρ_b but does not say if it was removed from or stayed at the location. Later in this chapter, the importance of such a distinction is clarified.

In Figure 7.3 the production as a function of I_j from Table 6.15 is plotted labeled with the corresponding values of τ_B of each test. The production defined in Chapter 6 is initial production (P_i). The production is normalized per meter width. A slight positive trend can be observed: a higher I_j applied to the bed causes more P_i by the jetting process occurs. The data of the trial week falls on the trend of the first runs of every test.

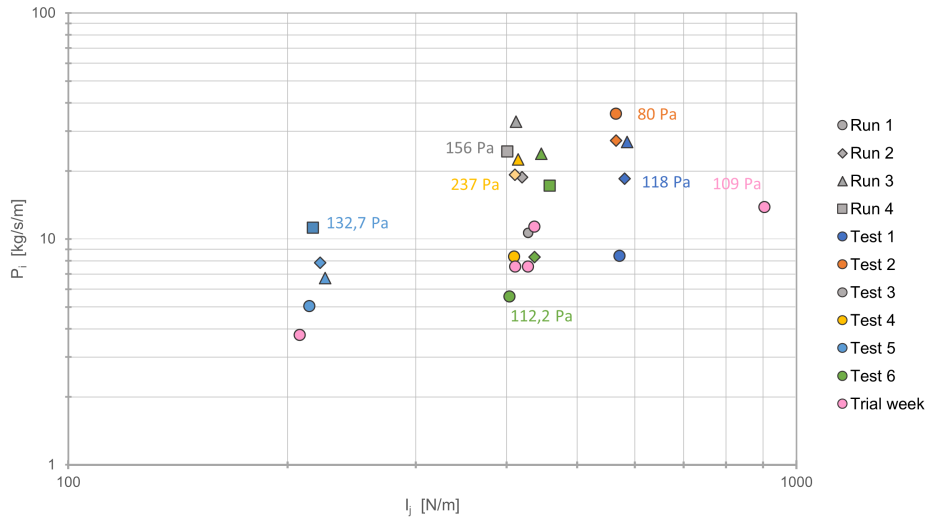

Figure 7.3: P_i as a function of I_j per unit width (strength of the bed indicated by labels).

Tests with lower values of τ_B cause higher P_i compared to higher values of τ_B for a I_j in the same order of magnitude. This can be observed between e.g. test 1 and 2 and between tests 3 and 4. However, at some points in the graph, this is not the case. P_i of test 6 is smaller during runs 1, 2 and 4 in comparison to the same runs of test 3 or 4 despite a lower value of τ_B during test 6. This observation can be linked to the fact that for these runs a SOD_r of 300 mm was applied. Run 3 of test 6, however, produces a significant increase in P_i in comparison to runs 1, 2 and 4, close to the ones of tests 3 and 4. During run 3, a SOD_r of 60 mm was applied. The influence of the SOD on the production rate is discussed

further in Section 7.4.

7.2.1. Production rate versus jet momentum

To be able to relate the WID production of the experiments to the jet production linear with the jet momentum, the theory of the production of sand by a moving jet of Vlasblom (2003) is applied to the experimental data:

$$M_s = \alpha_s I = \alpha_s \rho_w Q_j u_j = \alpha_s \rho_w Q_j \sqrt{\frac{2p_j}{\rho_w}} \tag{7.2}$$

with M_s the mass flux of eroded sediment and α_s a non-dimensionless empirical fitting parameter. The parameter settings of all the runs of every test have been applied to Equation 7.2 and plotted against the corresponding production (P_i) from Table 6.15. α_s is then iterated per run per v_t to match the values from Equation 7.2 and P_i as close as possible, i.e. fit the data to a 1:1 relation. The iterated values of α_s and the corresponding mean square error (MSE) are given in Table 7.1. M_s for the test settings together with α_s from Table 7.1 is plotted against P_i in Figure 7.4.

A distinction is made in v_t because a higher value of v_t should result in a lower value of s_{intr} (van Rhee, 2018) and to some extent a lower P_i. P_i is proportional to, among other things, s_{intr}. Table 7.1 unveils that a difference indeed occurs. However, α_s for v_t = 0.40 m/s is higher than for 0.25 m/s, which is the opposite of what is expected. Therefore, during these experiments, a variation in τ_B has a larger influence on the production than a variation in v_t.

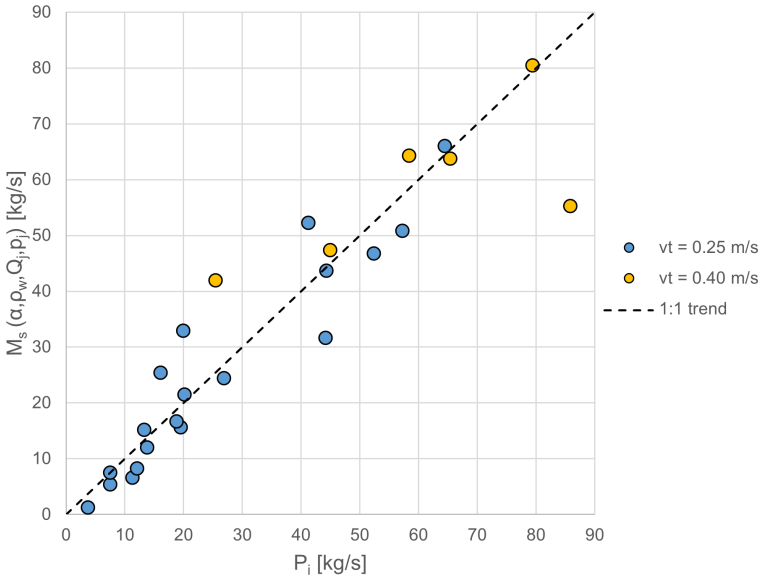

Figure 7.4: Production of according to the Vlasblom equation plotted against the production from Table 6.15.

	α_s (v_t = 0.25 m/s)	MSE	α_s (v_t = 0.40 m/s)	MSE
Run 1	5	8.92	13	604.72
Run 2	10	82.68	15	4.22
Run 3	15	40.66	25	0.97
Run 4	15	62.79	20	34.18

Table 7.1: Iterated values of α_s per run per v_t.

It has to be noted that Equation 7.2 provides a rough estimate of the production by water jets. In Figure 7.4 the MSE from the 1:1 relation can be up to 82 kg^2/s^2 (not taking the yellow outlier of 604 kg^2/s^2 into account). In Equation 7.2 the type of sediment and strength is not taken into account, though this may

influence the production significantly. When applied to e.g. sand the particle size distribution matters because it determines the permeability. For the case of this study the yield strength of the non-cohesive marine sediment determines when failure occurs.

The values of α_s from Table 7.1 are applicable for the range of τ_B of 80 – 237 Pa (= 1282 - 1334 kg/m^3). For values of τ_B outside this range it cannot be said for certain if the corresponding values of α_s hold as well.

Table 6.15, Figure 7.3, and Table 7.1 demonstrate ascending values of s_{intr} from run 1 onwards for most tests while the WID parameter settings stay similar between runs. Most tests of Schulting (1998) show the same behaviour by the mud, but an exact explanation is not given. Section 7.2.2 and 7.2.3 provide an analysis on the data of this study to gain more insight into this behaviour.

7.2.2. Dilution of the bed

In Figure 7.5 the intrusion depth normalized with the averaged nozzle diameter without contraction coefficient ($s_{intr}/D_{n,a}$) is plotted as function of the jet pressure normalized with the strength of the bed (p_j/τ_B) for all runs of all tests. $D_{n,a}$ is the total nozzle area of the 24 nozzles divided by the width of the jetbar. The situation is then represented as if the jetbar would discharge the water as a thin sheet over the width instead of 24 separate nozzles. For test 6, u_j applied to the bed with a SOD$_r$ of 300 mm is corrected according to (van Rhee, 2018)

$$\frac{u_{s,0}}{u_0} = \sqrt{\frac{k_1}{2}}\frac{D_n}{s} \approx 6.2\frac{D_n}{s} \tag{7.3}$$

for s > 6.2D_n with k_1 = 77 (Nobel, 2013) and s the distance from the mouth of a nozzle for a free-flowing jet in water, which is the same as the SOD. u_j is then converted to p_j according to Equation 5.1. Though this may not be fully accurate because Equation 7.3 only holds for the centre of a jet (r = 0) and decreases rapidly towards the border of the turbulent cone, it still provides an indication in the right order of magnitude.

Figure 7.5 illustrates a (weak) positive trend of $s_{intr}/D_{n,a}$ as a function of p_j/τ_B. The spreading is in the order of 4 to 20 cm (60%). The accuracy measured with the disk is between 1 and 2 cm. The accuracy of the disk does not explain the 60% spreading and therefore another explanation is needed.

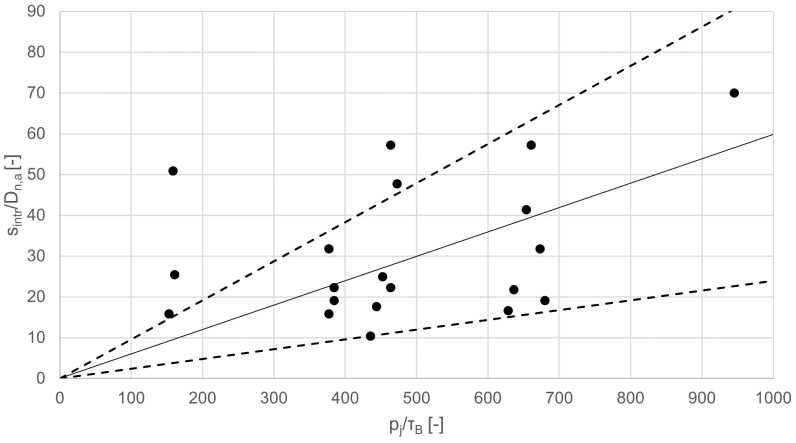

Figure 7.5: Test data of normalized s_{intr} over normalized p_j. The solid black line is the overall fit through all the data and the dashed lines are the approximate error boundaries.

In Figure 7.6 the data is plotted per run for all tests. As mentioned before, it is remarkable to see that all measured points for runs 2 to 4 are significantly higher than those for run 1. The blue trend is plotted on the data of run 1 and cuts the zero point of the graph. Because during later runs higher s_{intr} for the same jet pressure is produced, the bed must have lost strength (decreased τ_B) during the previous run and should follow the trend of the first (undiluted) runs. In Figure 7.7, all data outlying the error boundary (marked by the light grey area) is corrected for the blue trend. The error boundary is 30%,

which matches most of the blue data points. The value of p_j/τ_B increases and therefore τ_B decreases. The decrease of τ_B is converted to a relative dilution.

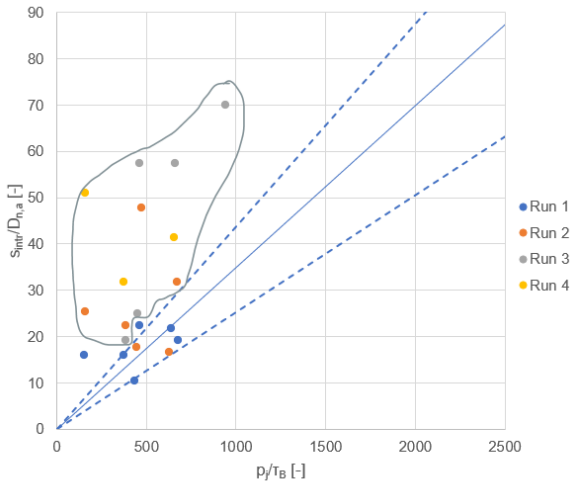

Figure 7.6: Normalized experimental data plotted per run.

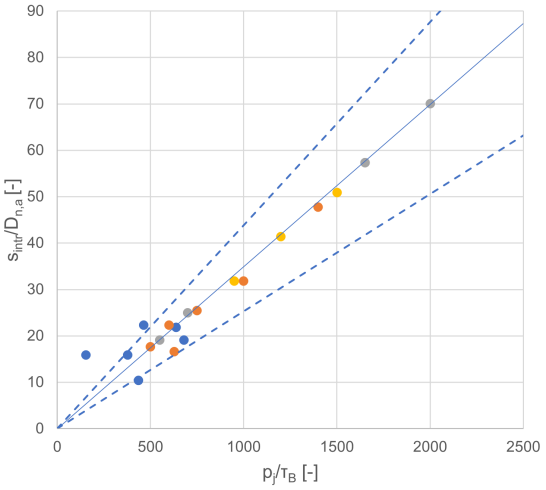

Figure 7.7: Normalized experimental data corrected for the blue trend.

Correcting the difference in τ_B of the corrected data to a difference in ρ (according to Equation 7.1) provides a trend of differences in volume concentration of solids (c_v) in the bed. Table 7.2 provides the percentage difference in dilution for all the corrected points. The total range in dilution is 2.25% to 42%. More specifically, for the second runs the dilutions range from 2.25% to 18%, for the third runs the dilutions range from 5.76% to 21% and for the fourth runs the dilutions range from 10.7% to 42%. The range in dilutions shifts upwards when the bed is injected multiple times. So when mud is penetrated by jets, a layer beneath s_{intr} is partly diluted. The sediment does not become fluid mud, but pore water is added to the bed. This causes τ_B to decrease and s_{intr} to increase during the next run. This increase in extra intrusion depth causes even more dilution in the new top part of the consolidated bed.

Test	Run	Original c_v	Corrected c_v	Absolute difference	Dilution in %
1	2	0.190	0.186	0.004	2.25%
3	2	0.203	0.189	0.014	6.99%
4	2	0.215	0.177	0.039	18.05%
5	2	0.223	0.207	0.016	7.16%
6	2	0.191	0.159	0.032	16.87%
1	3	0.189	0.174	0.016	8.27%
3	3	0.203	0.171	0.033	16.12%
4	3	0.216	0.171	0.045	21.04%
5	3	0.223	0.210	0.013	5.76%
6	3	0.191	0.164	0.027	14.09%
3	4	0.203	0.181	0.022	10.71%
5	4	0.197	0.164	0.033	16.79%
6	4	0.192	0.111	0.081	41.99%

Table 7.2: Values of original data points (Figure 7.6) and corrected data points (Figure 7.7).

7.2.3. Mass flux comparison

Initially, constant properties of the bed are assumed for the full duration of a test, i.e. the solids concentration of the bed and strength are not different between runs. But that should mean that s_{intr} does not differ too much between runs as well. The opposite is observed, however. The previous section indicates that when data of ascending runs of a test is corrected for the trend of the first run (see again 7.7),

and when it is certain that the bed is undisturbed over its full height, a decrease in required strength of the mud for the corresponding measured s_{intr} and thus a possible disturbance in the bed has occurred. This section analyzes the representative stretch and full-time series to see if this behaviour is seen back in the measured density and velocity data at the measuring frame at the end of the mud, by comparing the mass flux of the initial and actual production.

Representative stretch time series

Two mass fluxes are compared with each other: mass flux of sediment suspended into the water column by the jets if during all runs the initial sediment concentration of the bed (c_{init}) is assumed (P_i) to flow over the ramp and the actual mass flux of sediment transported by the density current measured at the frame (P_a). The control volume is schematized in Figure 7.8. For the calculation of P_a, the velocity profiles and density profiles at the ramp given in Chapter 6 are interpolated and integrated over the height. P_i is determined as follows:

$$P_i = s_{av,intr} \cdot w \cdot v_t \cdot c_{init} \tag{7.4}$$

with c_{init} the initial sediment concentration of the bed (= c_m for every test from Chapter 6) and $s_{av,intr}$ from Table 6.15.

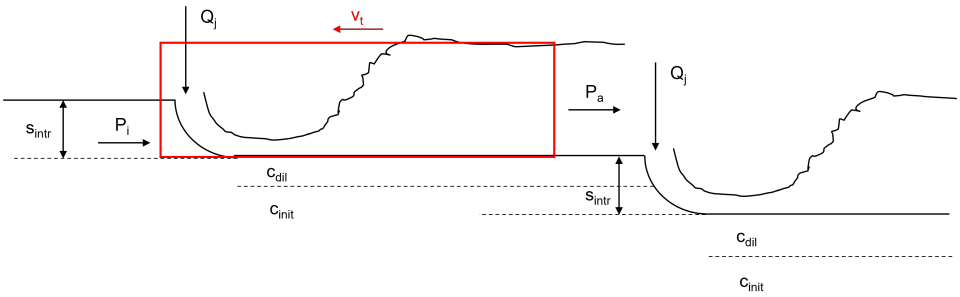

Figure 7.8: Schematization of the control volume with P_i as input and P_a as output, followed by the situation believed to follow after.

The results of P_i and P_a are presented in Table 7.3. For tests 1, 3 and 4 P_a/P_i decreases from run 1 to run 3, i.e. the difference in mass flux transported by the density current and the mass flux stirred up by the jets when the sediment concentration of an undisturbed bed is assumed to become bigger with ascending runs. For test 1, however, $P_a/P_i \geq 1$ for all runs, which means that more sediment is transported by the density current than is suspended by the jets. This should be impossible, but an explanation for this can not be found. For test 5 P_a/P_i decreases only from run 1 to run 2, but s_{intr} for the first three runs is almost the same (Table 6.15). For test 6, P_a/P_i is close to 1 for all runs with a SOD_r of 300 mm. So, for tests where s_{intr} increases and $SOD_r \approx 0$ mm (test 1, 3 and 4), P_a/P_i decreases.

The decrease of P_a/P_i between runs 1 and 2 of a test indicates that the penetrated volume with height s_{intr} for P_i during the latter run contains less sediment than was the case during the former run, i.e. the concentration of sediment of the penetrated volume is (at least partly) smaller than initially measured at the beginning of the test. A diluted concentration c_{dil} of the bed occurs within the penetrated volume of run 2 (or under the level of s_{intr} during run 1). Looking at the absolute values of P_i and P_a the rise in P_i is not seen back in P_a. P_a might increase as well, but not as much as P_i. P_a might increase by a few kg while the increase in s_{intr} should indicate a much larger increase. The occurrence of a layer of $c_{dil} < c_{init}$ decreases τ_B of the penetrated volume of run 2 (at least for the height at which c_{dil} occurs) and causes s_{intr} therefore to increases. A decrease in P_a/P_i between two runs thus can explain the increase in s_{intr} between the two runs. The same applies between runs 2 and 3: the amount of sediment in the penetrated volume of run 3 is even smaller than run 2, which can be related to an even higher s_{intr} than run 2.

Discussion on representative stretch time series approach

For the calculations of P_a and P_i, it is assumed that at the beginning of every run no suspended soil or fluid mud from the last run is left on top of the bed. After every run, the crest of the ramp is lowered

		Run 1	Run 2	Run 3	Run 4	
Test 1	P_i	16.1	45.7	64.5	-	kg/s
	P_a	39.0	88.7	63.7	-	kg/s
	P_i - P_a	-40.7	-63.9	13.8	-	kg/s
	P_a / P_i	2.42	1.94	0.99	-	-
Test 2	P_i	85.9	65.4	-	-	kg/s
	P_a	61.1	75.6	-	-	kg/s
	P_i - P_a	9.3	1.6	-	-	kg/s
	P_a / P_i	0.71	1.15	-	-	-
Test 3	P_i	27.0	45.1	81.1	58.6	kg/s
	P_a	18.2	23.5	24.6	63.5	kg/s
	P_i - P_a	9.1	21.1	53.5	-5.3	kg/s
	P_a / P_i	0.67	0.52	0.30	1.08	-
Test 4	P_i	18.5	43.2	52.5	-	kg/s
	P_a	27.2	29.7	29.7	-	kg/s
	P_i - P_a	-0.8	17.0	27.9	-	kg/s
	P_a / P_i	1.47	0.69	0.57	-	-
Test 5	P_i	13.5	18.9	16.2	27.0	kg/s
	P_a	4.1	5.1	17.9	15.4	kg/s
	P_i - P_a	7.6	13.0	14.6	20.9	kg/s
	P_a / P_i	0.31	0.27	1.11	0.57	-
Test 6	P_i	13.4	21.4	58.9	42.8	kg/s
	P_a	12.9	24.5	23.8	45.1	kg/s
	P_i - P_a	-4.3	-3.9	46.0	-2.0	kg/s
	P_a / P_i	0.96	1.15	0.40	1.05	-

Table 7.3: Theoretical initial production (P_i) compared with measured actual production (P_a) of the representative stretch.

and fluid mud which is left can flow away into the abyss behind the ramp. Probably not all fluid mud might flow away and part of it might be in P_a of the next run as well.

Furthermore, the values from Table 7.2 cannot be linked directly to the values of P_a/P_i in Table 7.3. During the correction of the data in Figure 7.7 and the corresponding dilutions from Table 7.2, it was assumed that these dilutions caused by the jets during the previous run reached over the full height of s_{intr} of the following run homogeneously. Whether this is true cannot be concluded from any data of the experiments of this study. No data on the density of the bed during the experiments was collected. Echo sounding measurements were conducted, and are presented in Appendix E, but the reflected sounding interfaces cannot be converted to density values. The low resolution also makes this data not useful, because it is hard to distinguish different layers within the souding profiles. A more detailed study should be conducted in combination with CFD modelling to gain a better understanding of what happens in the mud during jetting. This report does not contain such an analysis, because it is outside of the scope of this study.

Finally, it has to be noted that 'dilution' of the bed can mean several things. Diluting the soil in general means that water is added to the pore water of the soil. It is, however, unknown if the decrease in strength is homogeneously distributed within the soil or not and to what depth. Maybe weak points in the soil are filled with water from the jets and so-called cracks in the mud under the level of s_{intr} occur.

Full time series

The analysis above is conducted for the stationary situation of s_{intr} and the profiles that were determined in Chapter 6. So, the above applies to the representative stretch defined in the previous chapter. Now the same kind of analysis is conducted for the full velocity signals, given in Appendix C, by integrating over time and multiplying by the corresponding sediment concentration. This results in the absolute amount of mass over the ramp after each run $P_{a,abs}$ (in kg). $P_{i,abs}$ by the jetting process is calculated by integrating the difference in measured bed level after every run over the full length of the flume (in kg). Multiplying this height difference with the width and c_m provides $P_{i,abs}$. By integrating over the full time series, the fluctuations in time of these signals are taken into account and is, therefore, a more accurate approach.

In Figure 7.9 P_a/P_i from Table 7.3 is given and in Figure 7.10 $P_{a,abs}/P_{i,abs}$ is given both as a function of I_j. The vertical order between P_a/P_i and $P_{a,abs}/P_{i,abs}$ for most tests is the same, but for the full time integration, some runs of tests show much higher values above 1. Taking fluctuations in time into account causes the relative mass flux for some runs to increase. Despite that, the overall trend as a function of I_j for most tests is the same and the order of P_a/P_i per test for most tests is also similar. So, when the fluctuations in time are taken into account, the same behaviour is observed for the representative stretch. The full time integration, therefore, verifies the representative stretch time series approach at the beginning of this section.

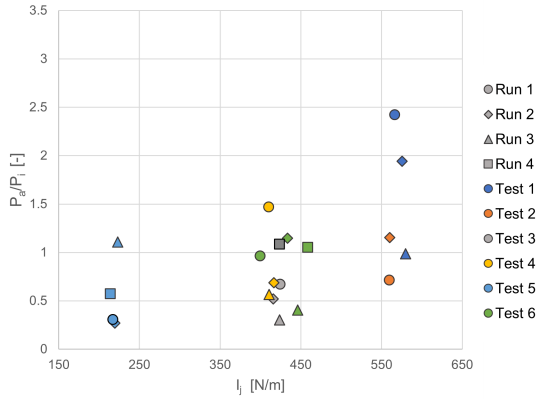

Figure 7.9: P_a/P_i as a function of I_j for the representative time series.

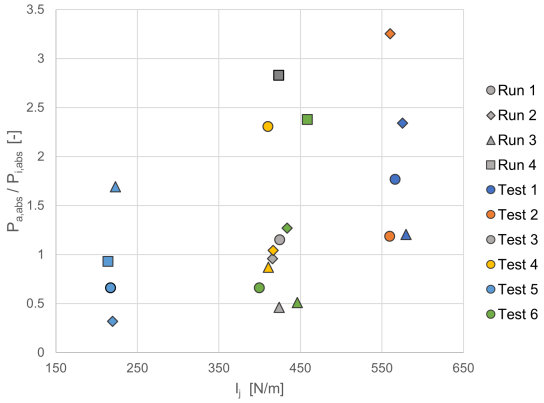

Figure 7.10: $P_{a,abs}/P_{i,abs}$ as a function of I_j for full integration over the time series specified per run.

An important notion is that P_a only includes the flux over the crest of the ramp. The measured profiles as input for P_a are measured on top of the ramp (at crest level). As was mentioned before, the level of the bed after a run is lower than the level of the crest of the ramp. At the end of some tests, it was observed that some fluid mud was left on top of the bed behind the ramp. The sediment which cannot flow over the crest is therefore neglected in the analysis, as is mentioned before. The density current is (partly) trapped if the momentum of the density current cannot overcome the difference between bed and crest level. This is one of the biggest uncertainties of this part of the analysis, but how big the influence is cannot be said with certainty since no data was collected on this. From visual observations, however, it was observed that the amount of fluid mud left was not as much such that it would disprove the above analysis.

The analysis from Section 7.2.2 and 7.2.3 indicates that the bed under the level of s_{intr} becomes disturbed by the jets. In particular places, pore water is added to the bed under the level of s_{intr} which decreases the strength of the new top layer and therefore causes a higher s_{intr} during the next run. The analysis, however, does not provide concrete values that can be used in practice but is merely qualitative. The situation is partly simplified by the assumptions and uncertainties mentioned above. How the bed becomes disturbed and to what extent is not further investigated in this study but is left for further research.

7.3. Density current dynamics

In this section, different aspects of the dynamics of the density current are analysed to gain a better insight into its behaviour as a function of the WID settings. In parts of this section, the results are linked back to the findings of the previous section on production rate (7.2).

7.3.1. Critical bed slope for a non-Newtonian fluid

Almost no horizontal transport by the density current is measured during some tests (see Chapter 6 and Section 7.2.3). The bed during the experiments is horizontal and it is analysed here whether a significant slope in the bed is necessary for the density current to flow without a momentum input from water jets.

The measured velocity profiles of the different tests unveil that the density current flows faster when a higher I_j is applied to the bed. The peak velocity of the measured velocity profiles u_2 (defined in Figure 4.5) is plotted as a function of I_j in Figure 7.11. u_2 is defined as the maximum velocity of the bell-shaped vertical velocity profile. However, u_2 is determined from the maximum measured data point and not from the maximum of the plotted line through the data points. The question may now arise about what causes the density current to flow and thus increase P_a. Although a positive trend of u_2 over I_j is illustrated, between 400 and 470 N/m u_2 ranges from 0 to 0.4 m/s and around 570 N/m from 0.5 to 0.8 m/s. The high variability of u_2 does not provide a decisive answer why P_a and I_j are positively related.

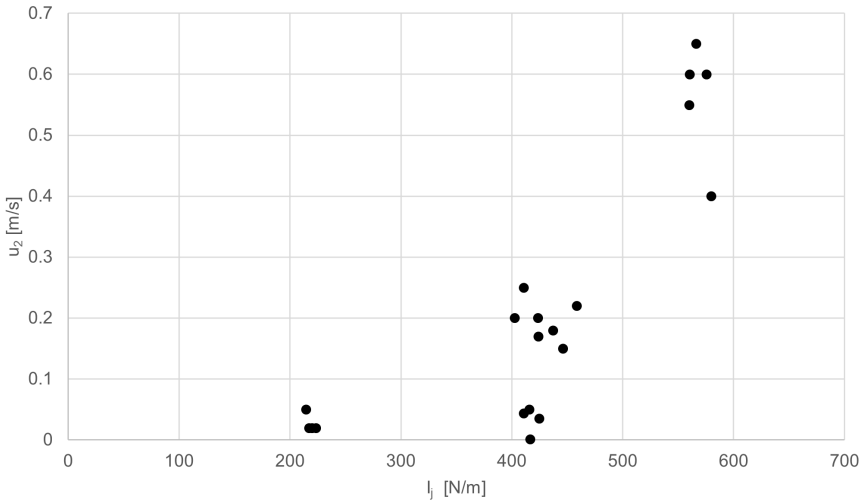

Figure 7.11: Measured peak velocities of the density current (u_2) as a function of I_j.

The critical bed slope for the initiation of motion of the density current is calculated. The experimental set-up is schematized as a horizontal bed with a slope β, an abyss and no external input of momentum from a jetbar. From the density profiles in Chapter 6 the highest density measured at the ramp in layer d_2 is ρ_m = 1150 kg/m^3 (with ρ_w = 1015 kg/m^3 (Appendix D): SSC = 223 g/L). This corresponds to τ_B = 4.3 Pa (Equation 7.1). h_2 = 10 cm. When this layer is schematized as a two layer system, i.e. clear water on top of the density current, the criteria becomes

$$\rho_m g' d \, tan(\beta) > \tau_B \tag{7.5}$$

For $d \approx 2h_2$ and $g' = (\rho_m - \rho_w)/\rho_w \cdot g$ = 1.47 m/s^2 the outcome is β_{cr} = 0.73 degrees. A hydrostatic pressure distribution and hydraulic smooth bed is assumed.

The critical bed slope is small such that most of the fluid mud should start to flow just by the difference in density for the small stretch of flume during the experiments. The yield stress of the fluid mud, therefore, does not obstruct the current such that it will not flow. The momentum of the density current originates from the water jets and the difference in density between the fluid mud and clean water. More initial momentum (I_j) applied to the bed, however, causes more stirring-up of sediment and can increase the density of the current, thereby increasing the driving force caused by the density difference as well.

7.3.2. Flow regime

The densimetric Froude number Fr_2 of a density current is defined in Equation 4.5 in Section 4.4. Fr_2 and I_j are given in Table 7.4 and are plotted against each other in Figure 7.12. The trend and distribution of the data is almost the same as in Figure 7.11. Fr_2 therefore mainly depends on u_2. The plots of the density profiles in Chapter 6 illustrate most of the time a high and low concentration layer d_1 and d_2 regardless of the magnitude of u_2. Figure 7.12 illustrates that for I_j < 500 N/m a sub-critical flow and for I_j > 500 N/m a super-critical flow of the density current at the ramp occurs. A possible explanation is given in this section.

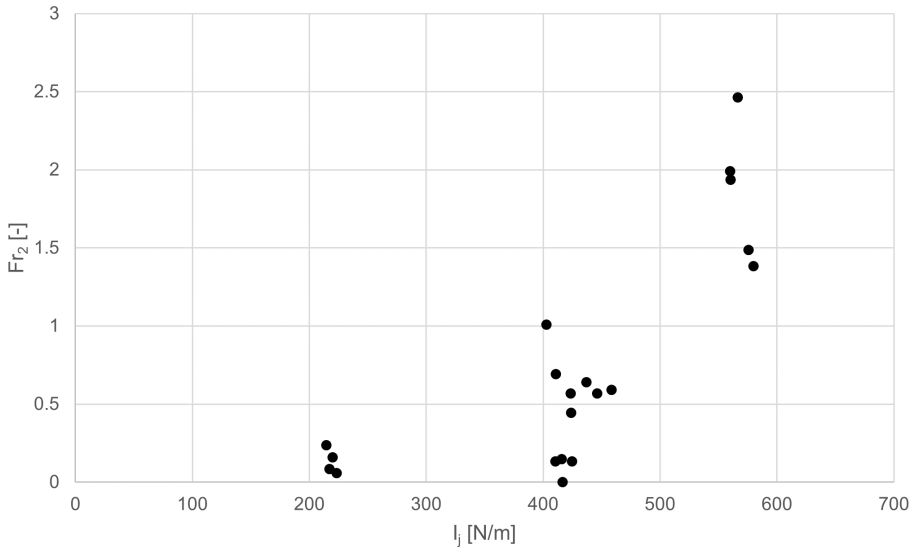

Figure 7.12: Fr_2 as a function of I_j.

The horizontal momentum of the density current at the ramp (I_{ramp}) is compared to the vertical momentum by the jets I_j using the ratio I_{ramp}/I_j. The amount of momentum of the density current is averaged over the height of the lower high concentration layer by using 3/4 of u_2. Table 7.4 shows that for I_j > 500 N/m relatively more horizontal momentum is measured at the ramp in comparison to I_j < 500 N/m.

		Fr_2	I_j [N/m]	I_{ramp} [N/m]	I_{ramp}/I_j [-]
Test 1	Run 1	2.46	566.26	45.48	0.0803
	Run 2	1.49	575.44	54.14	0.0941
	Run 3	1.38	579.73	63.87	0.1102
Test 2	Run 1	1.99	559.74	34.02	0.0608
	Run 2	1.94	560.17	108.86	0.1943
Test 3	Run 1	0.13	424.63	0.09	0.0002
	Run 2	0.15	415.83	0.32	0.0008
	Run 3	0.45	423.80	4.45	0.0105
	Run 4	0.57	423.55	8.70	0.0205
Test 4	Run 1	0.13	410.47	0.24	0.0006
	Run 2	0.0002	416.44	4.62	0.0111
	Run 3	0.69	410.63	5.18	0.0126
Test 5	Run 1	0.08	217.10	0.74	0.0034
	Run 2	0.16	219.68	0.04	0.0002
	Run 3	0.06	223.18	0.04	0.0002
	Run 4	0.24	214.24	0.18	0.0009
Test 6	Run 1	1.01	402.46	9.18	0.0228
	Run 2	0.64	436.89	7.58	0.0174
	Run 3	0.57	446.15	2.09	0.0047
	Run 4	0.59	458.42	8.51	0.0186

Table 7.4: Momentum balance between the jets and the measured density profiles at the ramp.

The loss in momentum is partly due to the turbulent interface between the density current and the stationary water on top or the friction from the bed. For the flow of a density current, it is known from Equation 4.7 to 4.10 that U is proportional to $1/(f_b + f_i)$, with f_b and f_i a bottom and interface friction factor. The shear stress from the bed and interface on top of the density current ($\tau_b + \tau_i$) are proportional

to f_b and f_i respectively. Thus Fr_2 is proportional to $1/(\tau_b + \tau_i)$.

When the density profiles at the ramp (given in chapter 6) are compared to the corresponding values of I_{ramp}/I_j it stands out that the vertical density gradients ($d\rho/dz$) are small and relatively high flow velocities near the bottom (≥ 0.20 m/s) are measured when relatively more I_{ramp} is measured as well (I_{ramp}/I_j > 0.015). This can be seen e.g. for all runs of test 1 and 2 and run 1, 2 and 4 of test 6. Small $d\rho/dz$ and relatively high flow velocities (thus higher du/dz), according to the definition of the Richardson number (Equation 4.14), indicate an unstable density current and cause turbulence which would decrease I_{ramp}, from a qualitative point of view at least.

For runs when a relatively low I_{ramp} is measured (I_{ramp}/I_j < 0.015), $d\rho/dz$ is higher and flow velocities are relatively smaller (≤ 0.20 m/s) in comparison to cases for I_{ramp}/I_j > 0.015. This should lead to a more stable density current according to the definition of the Richardson number.

When I_{ramp} is relatively high, observations in $d\rho/dz$ and du/dz indicate an unstable density current. One would expect the current to be even more unstable when I_{ramp} is relatively low but $d\rho/dz$ and du/dz indicate a more stable current compared to when I_{ramp} is relatively high. So, with less relative momentum measured at the ramp, the velocity and density profiles indicate less turbulence in the current as well. These are two counteracting observations. τ_b and/or τ_i probably do not contribute significantly to the loss of horizontal momentum, although these stresses can cause a lot of turbulence. It is worth noting that other factors cause turbulence as well.

A second cause of loss in momentum is the difference in height between the level of the bed and the level of the crest of the ramp to which the current runs up. The momentum is deflected upwards and then deflects horizontally again. This deflection causes the amount of horizontal momentum to decrease. A last possible cause of loss of momentum is the difference in density between the current and the surrounding water. The higher density of the density current causes the layer to flow because of the difference in hydraulic pressure, but the surrounding water provides a counteracting force to the flow.

This section tried to explain the behaviour seen in the previous section on the production rates (7.2). Production for I_j > 500 N/m was relatively higher than most other runs where I_j < 500 N/m. For I_j > 500 N/m, a super-critical density current is observed in the data as well, corresponding with a relatively high amount of momentum measured at the ramp.

7.4. Stand-off distance

This section discusses the influence of the SOD on production rates and behaviour of the density current. Observations made in the test results and from the analysis above provide an answer to the additional question posed in the introduction of this report. Runs 1, 2 and 4 of test 6 have a SOD_r of 300 mm and run 3 has a SOD_r of 60 mm. Run 1, 2 and 4 are therefore mainly compared to run 3 as all other remaining parameters between these runs are the same.

7.4.1. Production rate

Section 7.2 mentions that during test 6 the SOD_r of 300 mm had a noticeable influence on P_i. Figure 7.3 illustrates that run 1, 2 and 4 of test 6 produce a smaller P_i than run 3. Runs 1, 2 and 4 of test 6 also produce a lower P_i compared to runs 1, 2 and 4 of other tests for the same I_j (tests 3 and 4). This observation is even more remarkable since τ_B of test 6 is smaller than that of tests 3 and 4. So, despite a lower τ_B and equal I_j, runs of test with a SOD_r of 300 mm produce a smaller P_i compared to runs with a SOD_r of nearly 0 mm.

A SOD_r of 300 mm is > $6.2D_n$ = 6.2 · 20 mm = 124 mm thus the flow from the jets for the analysed cases is beyond the flow development region of the jets. According to Equation 7.3, $u_{s,0}$ decreases linearly with distance from the jet nozzle s when SOD_r > $6.2D_n$ and thus decreases the stagnation pressure at a distance s in the centre of the turbulent cone of the jet ($p_{s,0}$) as well. So, at 300 mm SOD_r a decrease between u_j and p_j occurs compared to u_j and p_j at the nozzle exit. This probably causes P_i to be relatively smaller in comparison to when SOD_r < $6.2D_n$.

7.4.2. Density current

In Table 7.4 it can be observed that I_{ramp}/I_j for runs 1, 2 and 4 of test 6 is higher than run 3 of test 6 and all runs of tests 3 and 4 where I_j is in the same order of magnitude. Because more horizontal momentum is measured at the ramp during runs 1, 2 and 4 of test 6, the transport of sediment, therefore, increases and causes P_a and thus P_a/P_i to increase as well (see Table 7.3).

During the experiments, video recordings were taken behind the glass wall to be able to make visual observations of the density current. Unfortunately, only the videos of run 2 of the trial week and run 1 of test 6 are of sufficient quality to be able to recognize the density current in the video. Some snapshots of the videos are given in Figure 7.13a to 7.13f.

I_j for run 1 of test 6 is very close to run 1 of the trial week and makes the quality of comparison of the two density currents reliable. τ_B also only differs 3 Pa between the two cases and v_t and p_j are for both the same. In case of a SOD_r of 0 mm solely a sub-critical regime is observed right behind the jetbar. For a SOD_r of 300 mm, a hydraulic jump is visible followed by a sub-critical regime. Billows like Kelvin–Helmholtz instabilities then follow and are visible in the third and fourth snapshot (Figure 7.13e

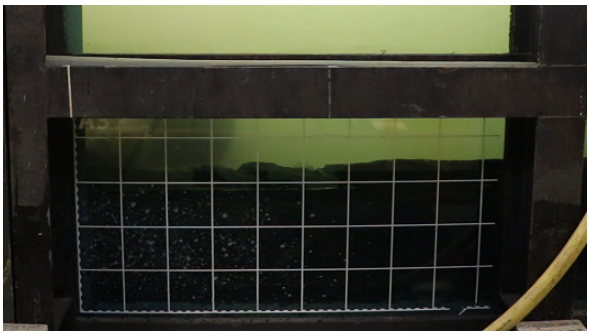

(a) Snapshot (1) of video recording: run 2, trial week. p_j = 1.07 bar, I_j = 426 N/m and SOD_r = 0 mm.

(b) Snapshot (2) of video recording: run 2, trial week. p_j = 1.07 bar, I_j = 426 N/m and SOD_r = 0 mm.

(c) Snapshot (1) of video recording: run 1, test 6. p_j = 1.00 bar, I_j = 401.6 N/m and SOD_r = 300 mm. Jetbar is still visible on the right side.

(d) Snapshot (2) of video recording: run 1, test 6. p_j = 1.00 bar, I_j = 401.6 N/m and SOD_r = 300 mm.

(e) Snapshot (3) of video recording: run 1, test 6. p_j = 1.00 bar, I_j = 401.6 N/m and SOD_r = 300 mm.

(f) Snapshot (4) of video recording: run 1, test 6. p_j = 1.00 bar, I_j = 401.6 N/m and SOD_r = 300 mm.

Figure 7.13: Snapshots of video recording of a density current for a SOD_r of 0 and 300 mm of the jetbar.

and 7.13f).

Finally, the flow velocity and density profiles measured at the ramp for the runs with a SOD_r of 300 mm illustrate that the height of the density current is larger in comparison to a SOD_r of 60 mm (see Figure 6.17 to 6.20). Because of entrainment of surrounding water, the flow rate of the jet (Q_s) increases with distance from the jet nozzle s according to (van Rhee, 2018)

$$\frac{Q_s}{Q_0} = \sqrt{\frac{8}{k}}\frac{s}{D_n} \approx 0.32\frac{s}{D_n} \tag{7.6}$$

and thus more water is pumped into the density current and therefore increases its volume. This transports sediment over a greater height and thus relatively more over the ramp as well.

In conclusion, the analysis on production rates shows that a $SOD_r > 6.2D_n$ decreases P_i in comparison to a $SOD_r < 6.2D_n$. However, P_a/P_i is closer to 1 when $SOD_r > 6.2D_n$. P_a is large because the height of the density and velocity profiles is larger in comparison to tests with a SOD_r of 0 mm while all other parameters are the same. Sediment is stirred up higher in the water column and can travel over a greater distance.

8 | Conclusions and recommendations

8.1. Conclusions

The introduction of this study defines two objectives:

- *Measure and analyze flow and sediment properties during the experiments in the water-soil flume for different parameter settings of water injection dredging.*
- *Find the optimal parameter setting of water injection dredging to maximize production.*

An additional question was added as well: *"What is the influence of the SOD on the behaviour of the density current?"*. Observations and analyses are conducted on the test results to reach the objectives and answer the additional question.

WID experiments have been conducted in the water-soil flume of Deltares over a stretch of 27 m of mud dredged from the Calandkanaal (Port of Rotterdam, The Netherlands). A jetbar was trailed (or *run*) multiple times over the mud with a fixed set of parameters. The flow velocity profile was measured at the end of the mud bed and the density profile was measured at the end of the bed and 1.4 m behind the jetbar. An analysis of these profiles at the end of the mud bed and disk measurements of the bed level shows that the parameter settings of water injection dredging have a significant influence on the production rates and behaviour of the density current. The disk measurements after every run of a test together with analysed samples of the bed show a positive relation between the production rate and jet momentum. The mass of sediment stirred up by the jets can be related linearly to the jet momentum using the Vlasblom equation where a non-dimensionless empirical fitting parameter is iterated per run per traverse velocity v_t. This relation can be used to apply the optimal jet settings for the desired production rate.

What is remarkable from the disk measurements is that the intrusion depth produced by the jets increases with ascending runs while the jet parameter settings stay the same. For tests where the intrusion depth increases with ascending runs and stand-off distance (SOD) $\approx$ 0 mm, the difference in mass flux by the density current and the mass flux stirred up by the jets when the sediment concentration of an undisturbed bed is assumed increases between runs. The increase in the difference between the two runs indicates that the concentration of sediment in the volume stirred by the jets is smaller during the latter run in comparison to the former run, thus is disturbed by the former run and therefore decreases in strength. This decrease in strength results in a larger intrusion depth during the latter run in comparison to the former run.

The analysis on the production rates shows that for tests with a high jet momentum, the mass of sediment transported by the density current is higher than for tests with a low jet momentum. The density current transports more sediment when initially more momentum is put in by the jets. The dynamics of the density current are analysed by determining the densimetric Froude number Fr_2 for every run of every test and plotting Fr_2 against the jet momentum. The plot illustrates that for a jet momentum > 500 N/m the density current is super-critical (Fr_2 > 1). From the measured flow velocity and density profiles, the momentum of the density current at the end of the bed is determined and shows that the ratio of momentum at the end of the bed over jet momentum is higher for a jet momentum > 500 N/m.

The influence of the SOD of the jets is analyzed by comparing runs with a SOD to runs without a SOD but with similar remaining jetting parameter settings. When SOD > $6.2D_n$, the jet stagnation pressure applied to the bed is outside the flow development region and therefore decreases with distance from the jet mouth. The data on production rates shows that the mass of sediment stirred up by the jets for runs with a SOD of 300 mm is lower in comparison to runs with a SOD of 0 mm, despite a lower strength of the bed. The ratio of the mass of sediment transported by the density current over the mass stirred up by the jets is however closer to 1 for runs with a SOD of 300 mm in comparison to runs without a SOD but similar remaining parameters. This is attributed to the observation that sediment is stirred up

higher in the water column and therefore has more time to settle, combined with high flow velocities also measured at these higher positions in the water column and entrainment. The combination of these two observations causes the sediment to travel over greater distances. So, if a large intrusion depth is required, no SOD should be applied and when large horizontal transport by the density current is desired, a SOD outside the flow development region of the jets should be used.

8.2. Recommendations

The experiments conducted for this study provide new knowledge on the principle of water injection dredging. However, little experimental research is conducted on this dredging technique and the results of this study post new questions to observations that cannot be answered solely from current knowledge.

The dynamics of the density current were briefly analyzed but most of the analysis was qualitative. More in-depth knowledge from the measured density and velocity profiles can be gained. For example, the velocity fluctuations in time can say something about the turbulence within the current or the height between the density profiles behind the jetbar and at the ramp can be compared to say something about the settling rate of the sediment in time.

The analysis of the production rate concludes that the bed becomes diluted (or disturbed) by the jets under the level of the intrusion depth and therefore decreases the strength, which results in a higher intrusion depth during the next run. To what depth and magnitude this dilution occurs in the bed and what other factors have an influence remains unknown at the end of this study. To unravel this, the same kind of experiments can be conducted with the right measuring and video equipment in place.

The experiments failed to take samples from the density current to determine its rheology. First steps have been made to include the rheology in CFD modelling of density currents from laboratory samples, but rheological data from density currents would enhance the quality of the output of these models. New experiments can be conducted where one can try to successfully take samples from the density current and analyse the rheology of the density with better qualitative data.

References

Allersma, E., De Groot, A. J., & Dijkema, L. (1984). Simulatie van slib. *Literatuurstudie. Delft: Waterloopkundig Laboratorium. Booij*, 1–150.

Anton Paar, A. (2021). *Portable density meter: DMA 35.* Retrieved 2021-03-05, from `https://www.anton-paar.com/corp-en/products/details/dma-35/`

Astarita, G. (1979). Scale-up problems arising with non-Newtonian fluids. *Journal of Non-Newtonian Fluid Mechanics*, *4*(4), 285–298. (Publisher: Elsevier)

Baird, A. J. (2002). Container Vessels in the New Millennium: Implications for Seaports. *Ocean Yearbook Online*, *16*(1), 300–327. (Publisher: Brill Nijhoff) doi: 10.1163/221160002X00196

Chassagne, C. (2019). *Introduction to Colloid Science*. Delft Academic Press.

Cushing, V. (1976). Electromagnetic water current meter. In *OCEANS'76* (pp. 663–679). IEEE.

Goda, A. (2021). *Rheological and plate's hydrodynamic resistance in fluid mud measurements for the nautical bottom applications: An experimental study for sailing through fluid mud applications* (Master thesis). Delft: Delft University of Technology.

Kirichek, A., Chassagne, C., Winterwerp, H., & Vellinga, T. (2018). How navigable are fluid mud layers. *Terra et Aqua*, *151*, 6–18.

Kirichek, A., Cronin, K., & De Wit, L. (2021). Advances in port maintenance: water injection dredging. In *IntechOpen.*

Kortmann, H. C. (1994). *Waterinjectie baggeren, een vernieuwde modellering* (MSc thesis). Delft: Delft University of Technology.

Krone, R. B. (1986). The significance of aggregate properties to transport processes. In *Estuarine Cohesive Sediment Dynamics* (pp. 66–84). Springer.

Leeungculsatien, T., & Lucas, G. P. (2013). Measurement of velocity profiles in multiphase flow using a multi-electrode electromagnetic flow meter. *Flow Measurement and Instrumentation*, *31*, 86–95. (Publisher: Elsevier)

Liard, M., Martys, N. S., George, W. L., Lootens, D., & Hebraud, P. (2014). Scaling laws for the flow of generalized Newtonian suspensions. *Journal of Rheology*, *58*(6), 1993–2015. (Publisher: Society of Rheology)

Mastbergen, D. R. (1986). *Behaviour flow of sand-water mixture at sand closures* (Tech. Rep.). Delft: TU Delft, Civil Technology.

Mastbergen, D. R. (1995). *WID demonstration tests* (Tech. Rep. No. No. J1014). Delft: DELFT HYDRAULICS.

Mastbergen, D. R., & Pennekamp, J. G. S. (1994). *Density Current Stability Analysis in the Case of Water Injection Dredging* (Tech. Rep. No. J0996). Delft: DELFT HYDRAULICS.

McCave, I. N. (1984). Size spectra and aggregation of suspended particles in the deep ocean. *Deep Sea Research Part A. Oceanographic Research Papers*, *31*(4), 329–352. (Publisher: Elsevier)

Middleton, G. V. (1993). Sediment deposition from turbidity currents. *Annual review of earth and planetary sciences*, *21*(1), 89–114. (Publisher: Annual Reviews 4139 El Camino Way, PO Box 10139, Palo Alto, CA 94303-0139, USA)

Miedema, S. A. (2019). Production estimation of water jets in drag heads. In *Proceedings of the Twenty-Second World Dredging Congress, WODCON XXII* (p. 17).

Moore, F. (1959). The Rheology of Ceramic Slips and Bodies. *TRANSACTIONS BRITISH CERAMIC SOCIETY*, *58*, 470–494.

Nezu, I., & Nakagawa, H. (2017). *Turbulence in open-channel flows*. Routledge.

Nobel, A. J. (2013). On the excavation process of a moving vertical jet in cohesive soil.

Owen, M. W. (1970). *A detailed study of the settling velocities of an estuary mud* (Vol. Report No. INT78). Wallingford, England: Hydraulics Research Ltd.

PIANC. (2013). *Injection Dredging* (Tech. Rep. No. 120). Brussels: The World Association for Waterborne Transport Infrastructure.

Schulting, W. H. (1998). *Jetten in slib ten behoeve van waterinjectie baggeren* (MSc thesis). Delft: Delft University of Technology.

Schuurman, K. A. D. (1997). *Modellering van het jetten van slappe menggronden tbv waterinjectiebaggeren* (MSc thesis). Delft: Delft University of Technology.

Sesták, J., Houska, M., & Zitny, R. (1982). Mixing of Thixotropic Fluids. *Journal of Rheology*, *26*(5), 459–475. (Publisher: The Society of Rheology)

Sigwald, R., Ledoux, S., & Spencer, K. (2015). *Water Injection Dredging Guidance Document* (Tech. Rep.). GEODE group: Groupe D'Etudes et D'Observation sur les Dragages et L'Environnement.

Swart, R. N. (2015). *Autonomous dredging of mud* (MSc thesis). Delft: Delft University of Technology.

Sánchez, R. J., Perrotti, D. E., & Gómez Paz, M. A. (2020). Ongoing challenges to ports: the increasing size of container ships. , 16. (Publisher: ECLAC)

Talmon, A. (2020). *Segregating Non-Newtonian Slurries* (Lecture notes OE44035 Dredging Pumps and Slurry Transport). Delft: Delft University of Technology.

Ten Brummelhuis, E. (2021). *Modelling of high concentration fluid mud water injection dredging density currents* (Master thesis). Delft: Delft University of Technology.

Van Kesteren, W. (2004). *Seafloor failure processes* (PhD-thesis). Delft: Delft University of Technology.

Van Leussen, W. (1988). Aggregation of Particles, Settling Velocity of Mud Flocs A Review. In J. Dronkers & W. van Leussen (Eds.), *Physical Processes in Estuaries* (pp. 347–403). Berlin, Heidelberg: Springer. doi: 10.1007/978-3-642-73691-9_19

Van Leussen, W. (1994). Estuarine macroflocs and their role in fine-grained sediment transport. *Ph. D. Thesis, University of Utrecht*.

van Rhee, C. (2018). *Lecture Notes OE44045* (Lecture notes OE44045 Dredging Processes II). Delft: Delft University of Technology.

van Rijn, L. C. (n.d.). Water Injection Dredging.

Van Rijn, L. C. (1993). *Principles of sediment transport in rivers, estuaries and coastal seas* (Vol. 1006). Aqua publications Amsterdam.

Van Rijn, L. C. (2016). Fluid Mud Formation.

Verhagen, H. J. (2000). Water injection dredging. *2nd International Conference Port Development and Coastal Environment: PDCE 2000, 5-7 June 2000, Varna, Bulgaria*. (Publisher: Black Sea Coastal Association)

Vlasblom, W. (2003). *Designing dredging equipment, lecture notes.* (Tech. Rep.). Delft: Delft University of Technology.

Williams, P. M. (2016). Zeta Potential. In E. Drioli & L. Giorno (Eds.), *Encyclopedia of Membranes* (pp. 2063–2064). Berlin, Heidelberg: Springer. Retrieved 2021-08-27, from https://doi.org/10.1007/978-3-662-44324-8_612 doi: 10.1007/978-3-662-44324-8_612

Wilson, D. A. (2007). Water injection dredging in US waterways, history and expectations. In *Proceedings of the 18th World Dredging Congress WODCON XVIII* (pp. 397–412).

Winterwerp, J. C. (1998). *Far-field transport and fate of fluid mud induced by Water Injection Dredging* (Tech. Rep. No. Z2200). Delft: DELFT HYDRAULICS.

Winterwerp, J. C., & Van Kesteren, W. G. (2004). *Introduction to the physics of cohesive sediment dynamics in the marine environment*. Elsevier.

Wren, D. G., Barkdoll, B. D., Kuhnle, R. A., & Derrow, R. W. (2000). Field techniques for suspended-sediment measurement. *Journal of Hydraulic Engineering*, *126*(2), 97–104. (Publisher: American Society of Civil Engineers)

Appendix A
Rheology of salt and fresh water dilutions

In this appendix, the rheological tests on Calandkanaal mud for different dilutions in the volume of salt and fresh water are presented. A controlled shear-rate test with a BOB geometry was carried out on different diluted mud samples. The samples were diluted in volume with fresh and salt water in two different ratios. The density of the undiluted sample was measured using a pyknometer and the density of the diluted samples was measured with a DMA 35. The details are given in Table A.1.

Water type dilution	**Dilution ratio**	**Density**	τ_B	**Plastic viscosity**
Fresh	1:1	1.1359 g/cm^3	3.35 N/m^2	0.0096 Pa·s
Fresh	1:0.6	1.1653 g/cm^3	11.5 N/m^2	0.113 Pa·s
Salt	1:1	1.1336 g/cm^3	2.50 N/m^2	0.0081 Pa·s
Salt	1:0.6	1.1669 g/cm^3	9.60 N/m^2	0.1258 Pa·s
No dilution	-	1.2381 g/cm^3	150 N/m^2	2.85 Pa·s

Table A.1: Rheology of different dilution ratios with salt and fresh water.

In Figure A.1 to A.5 the rheocurves corresponding to the different dilutions from Table A.1 are given in the same order. The red line represents the ramp down curve and the turquoise line is the dynamic viscosity. τ_B is determined by extrapolating the part of the red line from the high shear rates towards the vertical axis and determining the intersect.

The controlled shear rate tests for the dilutions with a ratio of 1:0.6 and the raw material were done

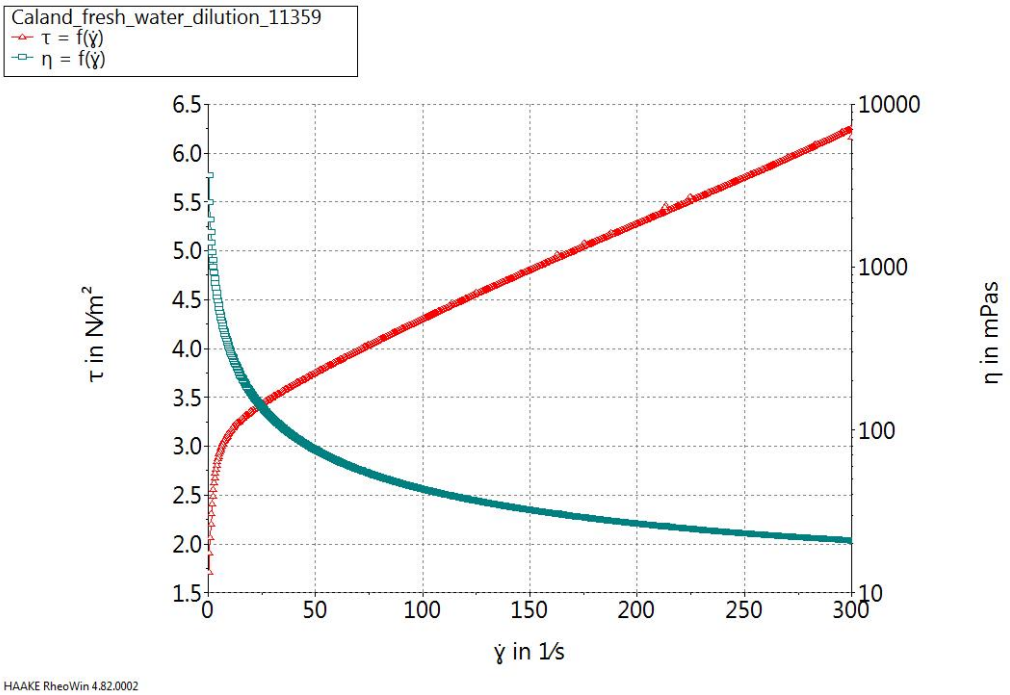

Figure A.1: Rheocurve of mud diluted with fresh water up to ρ = 1135.9 kg/m^3.

up to 20 1/s. The 1:1 dilutions went up to 300 1/s and were done the next day. These were done with higher shear rates to make interpolating easier. A higher shear rate gives a more straight line and thus more reliable τ_B. Unfortunately, it was forgotten to repeat this for the tests the day before.

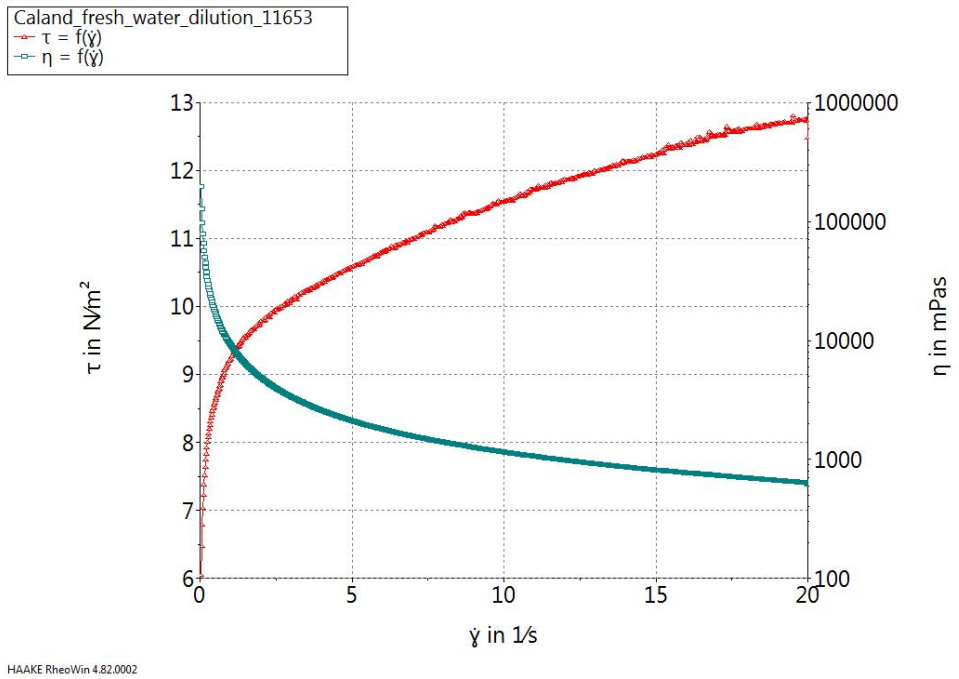

Figure A.2: Rheocurve of mud diluted with salt water up to ρ = 1165.3 kg/m^3.

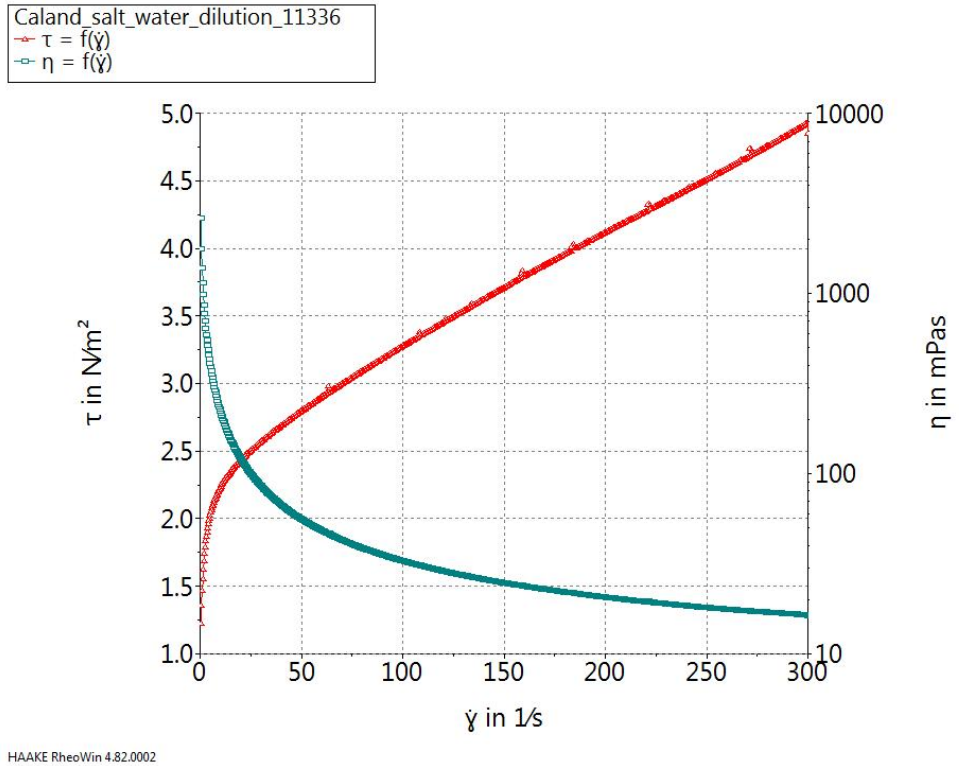

Figure A.3: Rheocurve of mud diluted with salt water up to ρ = 1133.6 kg/m^3.

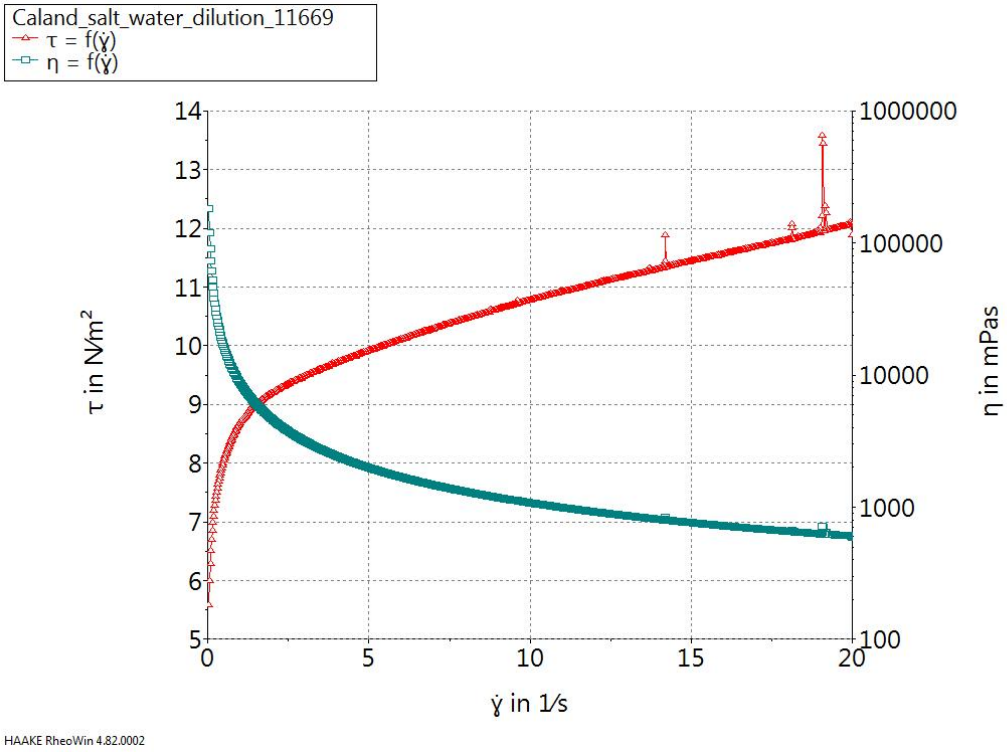

Figure A.4: Rheocurve of mud diluted with salt water up to ρ = 1166.9 kg/m^3.

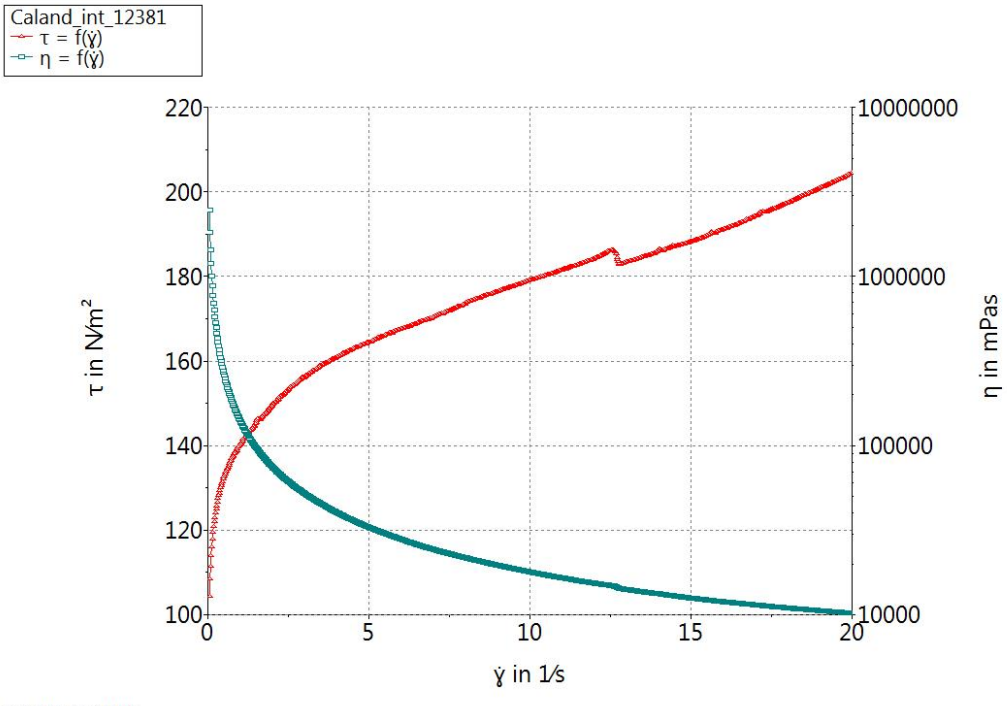

Figure A.5: Rheocurve of undiluted mud. ρ = 1238.1 kg/m^3.

Appendix B
Conductivity bar calibration

This appendix presents the calibration for the conductivity bars briefly described in Section 5.8.3. A mud sample was diluted six times and the density, temperature and relative voltage measured by the probes of the conductivity bars in that dilution were measured. The results for the conductivity bars of the frame are given in Table B.3 and plotted in Figure B.1 and B.2. The results for the conductivity bars behind the jetbar are given in Table B.4 and plotted in Figure B.3 and B.4.

For every probe or channel (Chan #) a line was fitted through the data and the corresponding function was derived. The relative voltage as a function of the density is described linearly as

$$\text{voltage} = \text{a} \cdot \text{density} + \text{b} \tag{B.1}$$

with a and b specified in Table B.3 and B.4 for every probe of the conductivity bars at the frame and behind the jetbar respectively. Rewriting Equation B.1 for the density as a function of the voltage and feeding the data from the experiments provides the results from the tests. The densities were measured with the DMA 35 device.

Chan 28 of the conductivity bars at the ramp shows a deviating calibration (Figure B.2) but does not post a problem with the results since the measured density profiles determined with this calibration show no strange behaviour for Chan 28. Furthermore, the measured signals of the conductivity bars behind the jetbar only go up to Chan 28. Though the same type of conductivity bars was used on top of the ramp, for unknown reasons no signal was measured at Chan 29 of the probes behind the jetbar.

	a	b	R^2
Chan 10	77.743	-84.679	0.9802
Chan 11	74.37	-81.406	0.9839
Chan 12	71.449	-78.35	0.9791
Chan 13	70.282	-77.075	0.9747
Chan 14	69.849	-76.583	0.9735
Chan 15	78.915	-85.842	0.9822
Chan 16	69.354	-76.157	0.9773
Chan 17	72.252	-79.05	0.9808
Chan 18	71.579	-78.435	0.9823
Chan 19	73.789	-80.548	0.9862
Chan 20	53.618	-60.265	0.9703
Chan 21	71.924	-78.555	0.9775
Chan 22	67.864	-74.491	0.9800
Chan 23	72.262	-78.873	0.9794
Chan 24	68.176	-74.711	0.9809
Chan 25	77.855	-84.533	0.9828
Chan 26	62.798	-69.449	0.9732
Chan 27	72.091	-78.544	0.9771
Chan 28	27.679	-33.983	0.8323
Chan 29	63.222	-69.649	0.9708

Table B.1: a and b for Equation B.1 for the calibration of the conductivity bars on the frame combined with the R^2 error of the fits from Figure B.1 and B.2.

	a	b	R^2
Chan 10	78.428	-84.835	0.9806
Chan 11	80.393	-86.865	0.9808
Chan 12	80.445	-86.849	0.9818
Chan 13	78.331	-84.720	0.9807
Chan 14	78.986	-85.332	0.9810
Chan 15	77.096	-83.478	0.9814
Chan 16	72.702	-79.098	0.9780
Chan 17	68.924	-75.299	0.9794
Chan 18	64.822	-71.143	0.9766
Chan 19	82.300	-88.807	0.9842
Chan 20	21.268	-27.319	0.9870
Chan 21	22.791	-29.090	0.9893
Chan 22	22.768	-29.079	0.9899
Chan 23	22.890	-29.193	0.9881
Chan 24	22.310	-28.480	0.9878
Chan 25	23.272	-29.550	0.9877
Chan 26	23.754	-30.165	0.9869
Chan 27	24.459	-30.870	0.9882
Chan 28	23.027	-29.352	0.9877
Chan 29	-	-	-

Table B.2: a and b for Equation B.1 for the calibration of the conductivity bars behind the jetbar combined with the R^2 error of the fits from Figure B.3 and B.4.

ρ_m (g/cm^3)	Temperature (°C)	Chan 10	Chan 11	Chan 12	Chan 13	Chan 14	Chan 15
1.1008	18.1	0.494	0.133	-0.027	-0.159	-0.159	0.594
1.0777	18.2	-0.697	-1.17	-1.252	-1.109	-1.059	-0.564
1.0535	18.2	-2.2983	-2.5604	-2.6316	-2.4908	-2.4584	-2.2044
1.0241	18.1	-4.71	-4.987	-4.773	-4.825	-4.773	-4.782
1.0191	17.9	-5.684	-5.7557	-5.7188	-5.614	-5.5592	-5.5592
1.0107	18.2	-6.4964	-6.6168	-6.5762	-6.4701	-6.4237	-6.4861

Chan 16	Chan 17	Chan 18	Chan 19	Chan 20	Chan 21	Chan 22	Chan 23	Chan 24
-0.232	0.077	0.007	0.393	-1.332	0.546	0.092	0.468	0.116
-1.217	-0.979	-1.149	-0.951	-2.767	-1.412	-1.61	-1.151	-1.313
-2.566	-2.4431	-2.5725	-2.3961	-3.169	-2.08	-2.375	-2.139	-2.381
-4.906	-4.837	-4.857	-4.699	-5.231	-4.739	-4.823	-4.571	-4.595
-5.601	-5.5331	-5.6053	-5.4593	-5.674	-5.351	-5.409	-5.351	-5.312
-6.4701	-6.4186	-6.4913	-6.3491	-6.3779	-6.1842	-6.2327	-6.26	-6.2327

Chan 25	Chan 26	Chan 27	Chan 28	Chan 29
0.846	-0.749	0.393	-4.08	-0.52
-0.588	-1.547	-0.674	-3.749	-1.232
-1.961	-2.789	-2.047	-4.309	-2.56
-4.554	-4.962	-4.492	-5.466	-4.702
-5.245	-5.495	-5.128	-5.829	-5.269
-6.3064	-6.4109	-6.158	-6.4793	-6.2039

Table B.3: Values of the conductivity bars on the frame for different dilutions per probe (Chan #) in volts.

ρ_m (g/cm^3)	Temperature (°C)	Chan 10	Chan 11	Chan 12	Chan 13	Chan 14	Chan 15
1.1008	18.1	1.101	1.227	1.303	1.101	1.204	1.015
1.0777	18.2	-0.188	-0.084	-0.005	-0.16	-0.05	-0.273
1.0535	18.2	-1.629	-1.607	-1.547	-1.626	-1.561	-1.725
1.0241	18.1	-4.3092	-4.2693	-4.2248	-4.279	-4.2248	-4.275
1.0191	17.9	-4.9427	-5.0035	-4.9264	-4.9581	-4.8819	-4.9581
1.0107	18.2	-6.052	-6.1068	-6.0208	-6.0191	-5.9798	-6.0358

Chan 16	Chan 17	Chan 18	Chan 19	Chan 20	Chan 21	Chan 22	Chan 23	Chan 24
0.537	0.23	-0.119	1.407	-3.35	-3.26	-3.20	-3.11	-3.05
-0.61	-0.925	-1.205	0.014	-2.98	-2.97	-2.98	-2.96	-2.92
-1.953	-2.183	-2.347	-1.55	-3.36	-3.39	-3.40	-3.37	-3.31
-4.4209	-4.49	-4.5144	-4.3325	-4.00	-4.08	-4.09	-4.07	-3.99
-5.0371	-5.0679	-5.1078	-4.9763	-4.16	-4.25	-4.26	-4.24	-4.16
-6.1068	-6.1068	-6.097	-6.0751	-4.42	-4.51	-4.52	-4.51	-4.42

Chan 25	Chan 26	Chan 27	Chan 28
-2.99	-3.06	-2.93	-3.13
-2.88	-2.95	-2.84	-2.97
-3.29	-3.36	-3.27	-3.37
-4.01	-4.09	-4.03	-4.08
-4.18	-4.28	-4.21	-4.26
-4.45	-4.55	-4.49	-4.52

Table B.4: Values of the conductivity bars behind the jetbar for different dilutions per probe (Chan #) in volts.

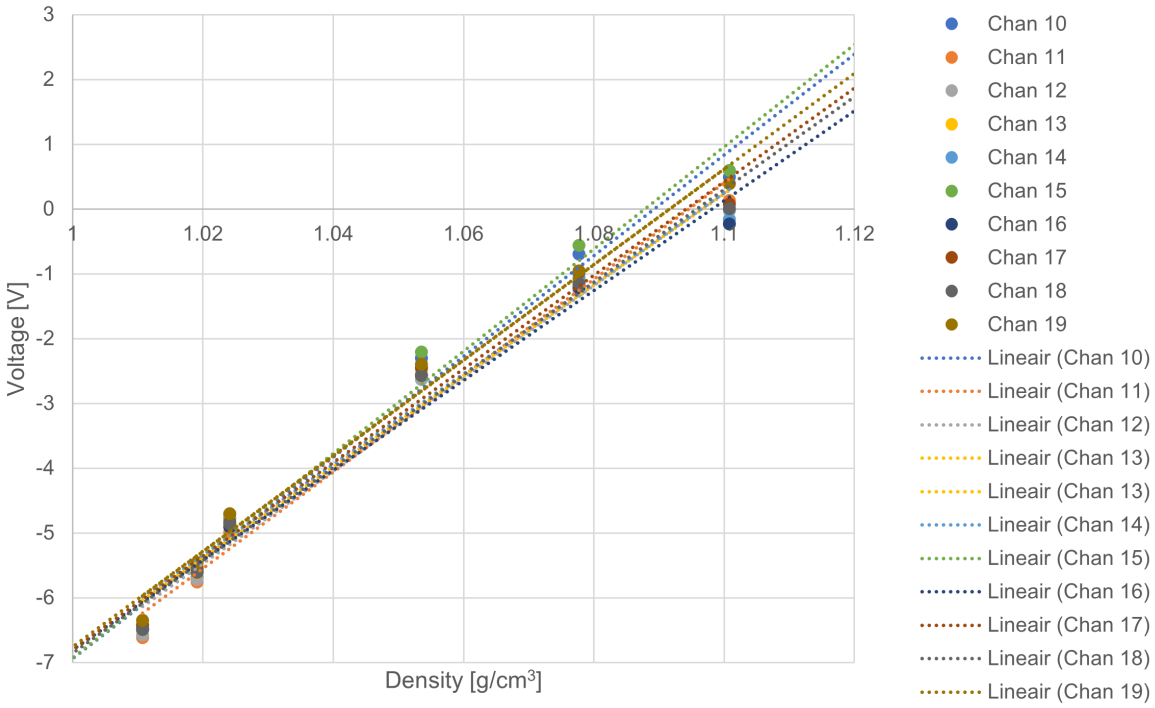

Figure B.1: Voltage measured as function of the density for Chan 10 to 19 for the conductivity bars on the frame.

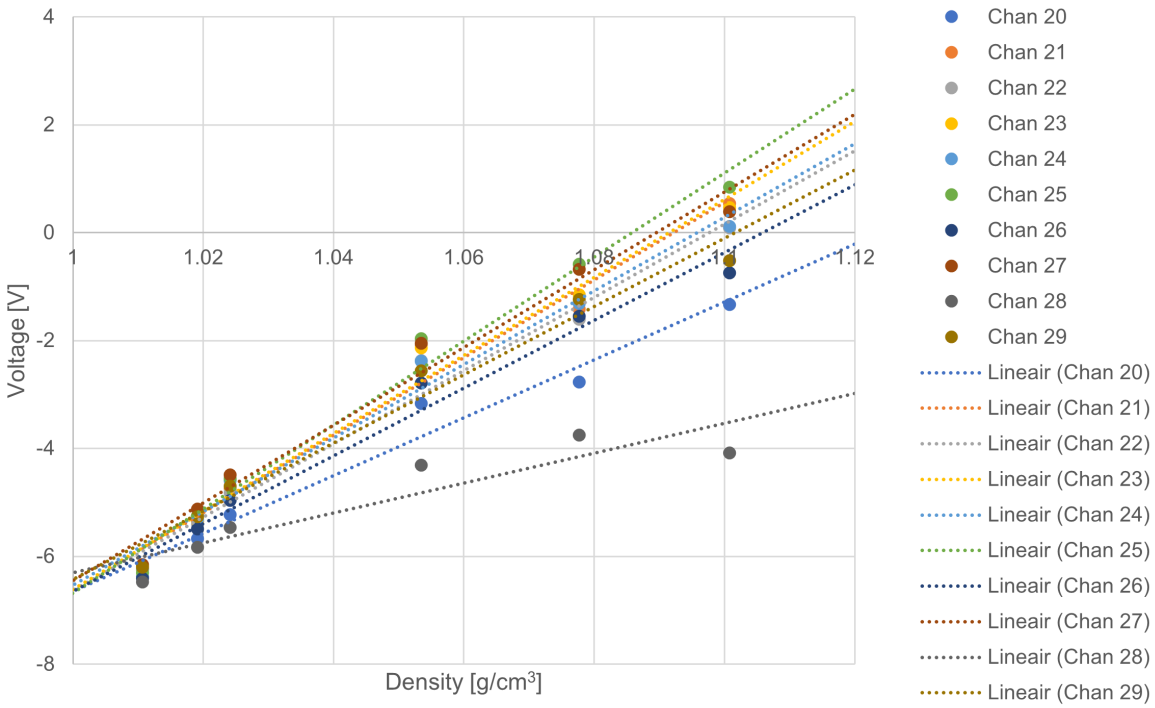

Figure B.2: Voltage measured as function of the density for Chan 20 to 29 for the conductivity bars on the frame.

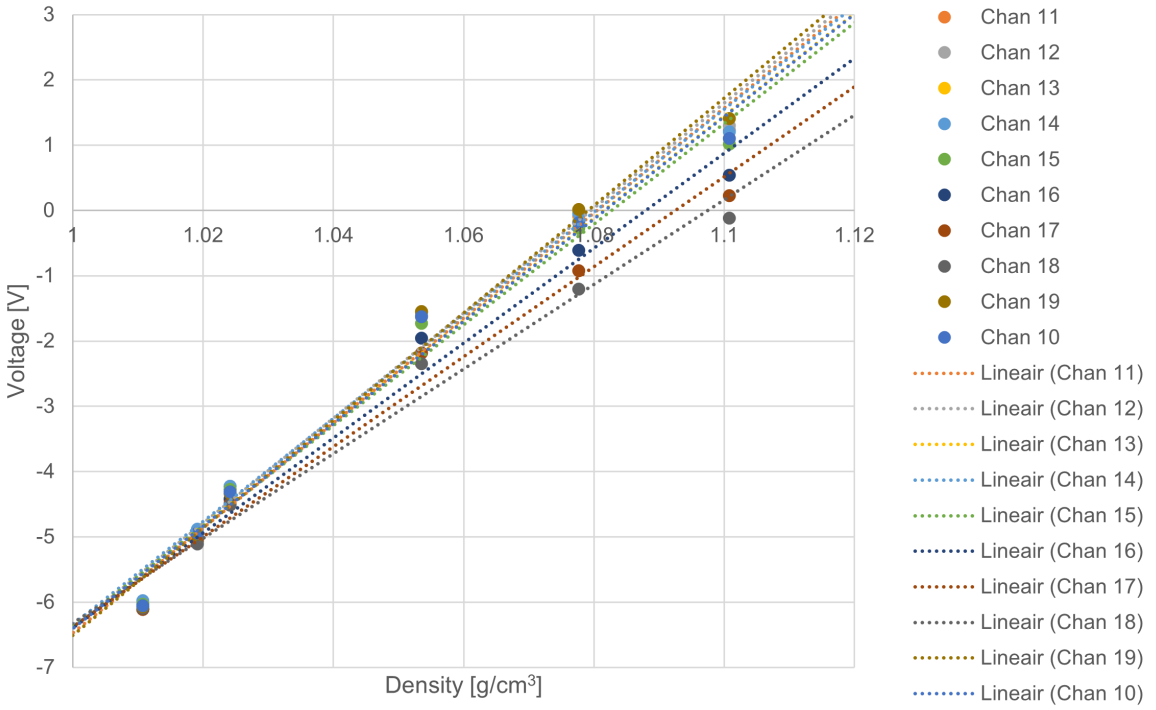

Figure B.3: Voltage measured as function of the density for Chan 10 to 19 for the conductivity bars behind the jetbar.

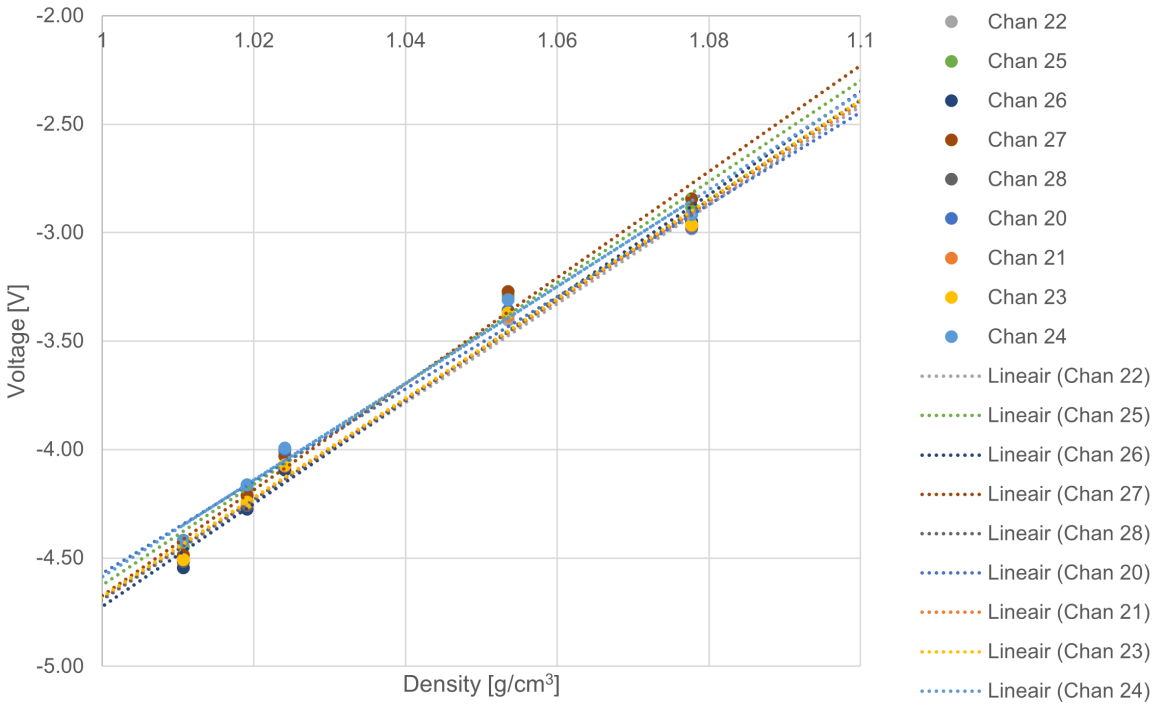

Figure B.4: Voltage measured as function of the density for Chan 20 to 29 for the conductivity bars behind the jetbar.

Appendix C
Test results: logs and time series

This appendix is an extension to Chapter 6 where the course of the tests and decisions made during the tests is described. The time series measured during every run of the tests are given at the end of every section as well. These time series were averaged to obtain the flow velocity and density profiles given in Chapter 6.

Trial week

Approach

A production corresponding to s_{intr} = 10 to 15 cm was desired, but from production formulas given in the literature, it could not be determined what settings were needed in the setup of the experiments of this study. Therefore, runs were done with varying D_n (20 and 30 mm) and p_j (0.5 and 1 bar). To make a good comparison between these parameters, all other parameters were kept constant. During each run only four nozzles were attached to the jetbar (n = 4) while the others were kept blind. During the next run, four nozzles with the corresponding D_n were attached to four places next to the ones of the previous run and the ones from the previous ones were made blind. Now the same stretch of mud was not jetted twice. These runs were conducted, because beforehand it was unknown what s_{intr} would be and to ensure to have enough mud for all the runs. The eventual settings of each run are given in Table 6.1. The results from these runs are given back in Table 6.2. The production as a function of the momentum, both in unit per meter width, is plotted in Figure C.1.

From the measured s_{intr} of the echo sounder and disk it was concluded that the echo sounding measurements were most reliable for these trials since they show repeatability for the same set of parameters (run 2 and 3). For unknown reasons, the disk showed a higher value of s_{intr}. Flow momentum I can be described as the flow of mass times the momentum per mass and is calculated as

$$I = Q \cdot u \cdot \rho_w \tag{C.1}$$

with unit N. The momentum can be normalized to 2D. The total jet momentum $I_{j,t}$ (for Q = Q_t and u = u_j) is then divided by n times the approximate width of the jet per n ($\approx$ 10 cm) to normalize I per meter width (I_j). The production is calculated as described in Equation 2.1.

Results

In Figure C.1 the data from Table 6.2 is plotted. The data shows a positive trend as a function of the momentum of the jets per meter width. Run 1, 2, 3 and 5 fall almost perfectly on the same line, but run 4 deviates from this trend. Run 4 produces more than is expected for that amount of momentum according to the other runs. For run 4 the data of the echo sounder was hard to interpret and it is possible that the wrong interface was identified, but because of the good correspondence with the disk measurements, this is unlikely.

The rheocurve made of the mud of the bed is given in Figure C.2. The intersection of the linear green line with the vertical axis represents the Bingham yield stress. The red line is the ramp down curve of the controlled shear stress.

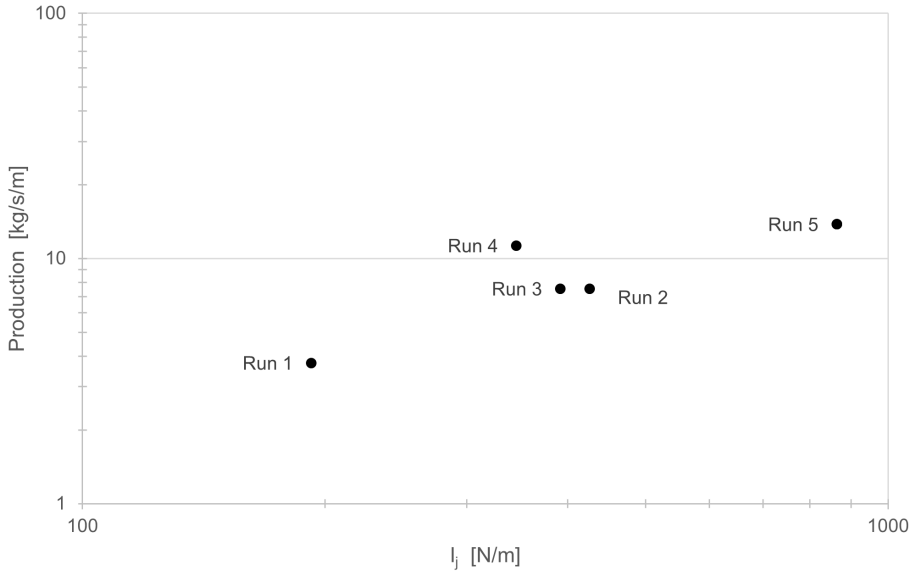

Figure C.1: Production versus momentum both normalized per meter width.

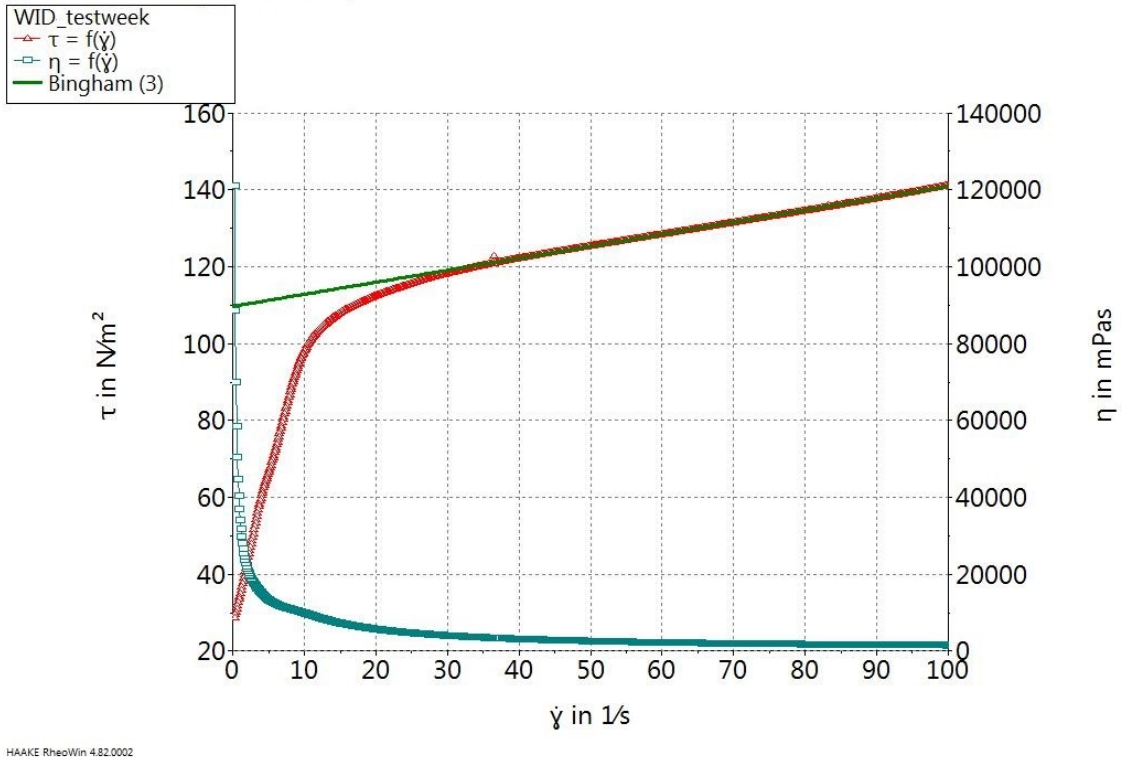

Figure C.2: Rheocurve of the mud bed at the beginning of the trial week (BOB-geometry).

Test 1

τ_B and D_n

The strength during this test (τ_B) is close to the 100 Pa criteria. As already mentioned, D_n is 35 mm. This is due to a mistake made during the process of drilling the nozzles to the right size. Because of this, the momentum of the jets is larger than expected and already after run 3 the bottom of the flume is touched by the jets. This mistake is unfortunately noticed only after test 5.

SOD_r and SOD_m

From test 1 onward a distinction is made between the SOD of the jetbar above the ramp (SOD_r) and the SOD of the jetbar relative to the level of the mud bed (SOD_b), see Figure C.3. During the analysis of the data, it was discovered that during the tests the level of the mud was not equal to the level of the crest of the ramp. If the level of the bed is above the level of the crest of the ramp, and also the level of the SOD relative to the crest (SOD_r), then SOD_b is negative, i.e. the jetbar is ploughing through the mud. Because of that, it is important to make a distinction between SOD_r and SOD_b.

$s_{av,intr}$ is the difference between disk measurements of the level of the bed before and after a run at a representative stretch of the flume. Because SOD_b can be negative, $s_{av,intr}$ does not necessarily start just below the level of the jetbar but can also start above the level of the jetbar. From the measured levels of the bed, the jetbar blows away sediment at higher levels than the jetbar and, because this sediment is also removed, it is seen as production as well. It is, however, important to take this into account when these results are analysed in further studies.

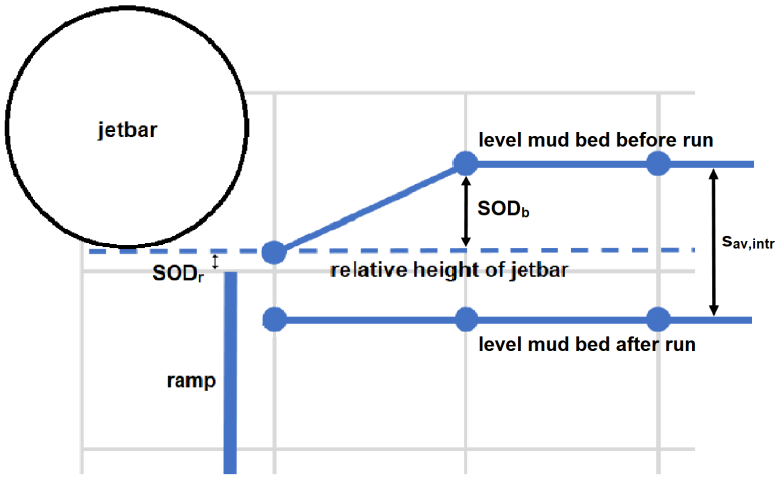

Figure C.3: Visualization of SOD_r and SOD_b where SOD_b is negative.

The pressure in the jetbar is measured at both ends. In Figure 5.11 the two sensors are illustrated on top of the horizontal tube attached to wires. The ”right” and ”left” sides are respectively the traversing direction. Furthermore, a SOD_r of 10 mm is used for the jetbar not to hit the top of the ramp. During the last run, a SOD_r of around 50 mm is needed in order not to hit the measuring frame. From the parameter sets of the other tests, this is applied during more tests as well.

Test results

In Figure C.5 the bed level after each run is plotted (relative to the top of the flume) together with the level of the ramp and jetbar at the beginning of a run. Figure C.4 illustrates the relative horizontal locations of these measured points. As mentioned before, the depth of the flume is 2.5 m. The initial thickness of the bed is approximately 0.56 m, but towards the ramp, it is decreased to 0.50 m, which is the same height as the ramp.

The bed level data presented in the upcoming sections originates from disk measurements. During post-processing of the data, the disk was considered more reliable than the echo sounder. The data from the echo sounding was hard to interpret for the actual tests. In most cases, different layers in

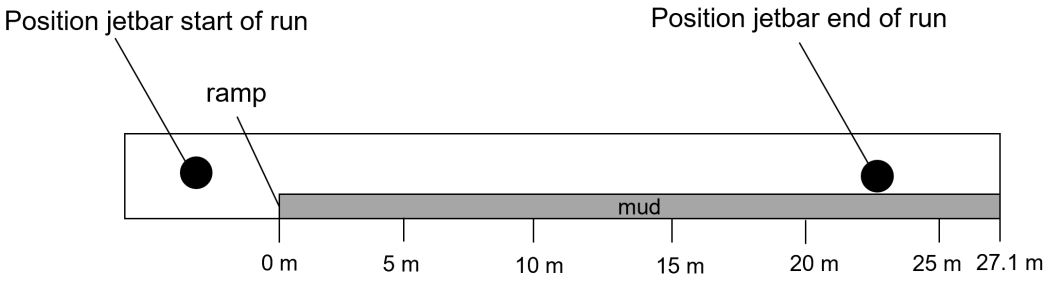

Figure C.4: Measuring positions in the flume.

the data could not be distinguished visually or were at the same level as the run before. The lower frequencies of the signal did not penetrate the fluid mud or it was at least not clear where the signal identified the transition between fluid mud and thick, consolidated mud. A possible explanation why the data from the trial week is reliable and that of the tests is not, is that during the actual tests a lot more fluid mud was created, which can be a problem for echo sounding. The disk always showed reasonable results. It can be said with certainty that the disk always penetrated the fluid mud and therefore gave an indication of the level of the thicker layers. In order to have the reader check these conclusions of the echo sounding data, the echo sounding profiles of all tests are given in Appendix E.

Figure C.5 , at a distance of 20 m from the ramp, a decrease in bed level is observed in the data. At the end of a run, the jetbar stops between 20 and 25 m but does not immediately stop injecting water into the mud. It took around 5 seconds to walk from the control panel of the carriage to the pump to turn it off, so after stopping the carriage, the jetbar was still blowing mud away at a fixed position.

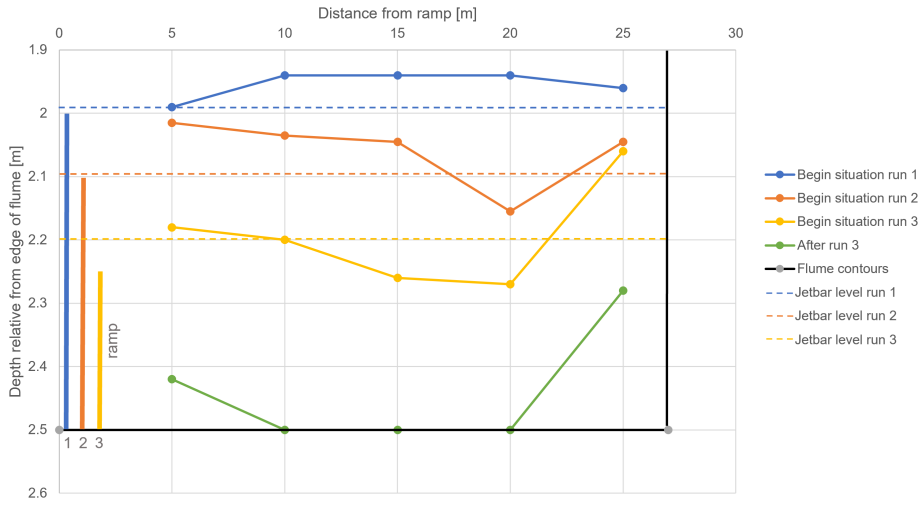

Figure C.5: Bed level after each run at different positions in the flume together with h_{ramp} (solid vertical line) and the level of the jetbar (horizontal dotted line) for test 1.

Table C.1 provides the time intervals over which is averaged to generate the flow velocity profiles and density profiles given in Figure 6.1 to 6.3. For a time interval of 50 - 75 seconds the jetbar runs from 12.5 to 27.1 meters in the flume.

	Time interval	
Run 1	50 - 75	s
Run 2	50 - 75	s
Run 3	50 - 75	s

Table C.1: Averaged time intervals from the time series for plotting the flow velocity and density profiles.

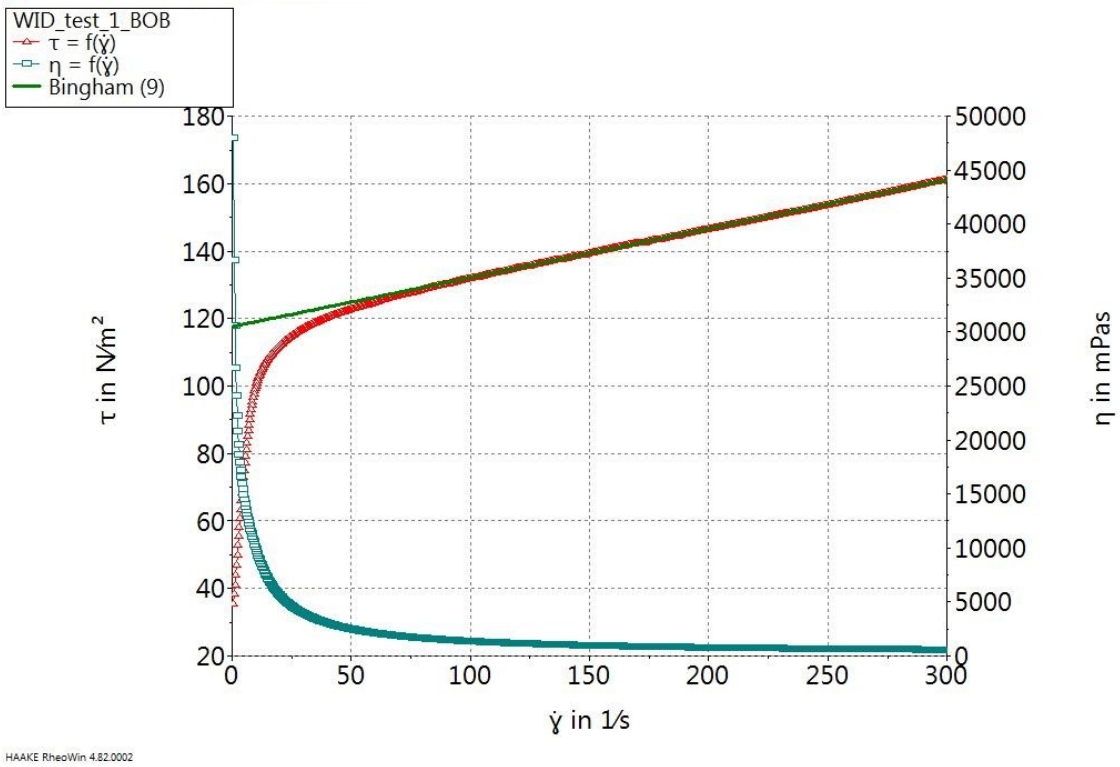

Figure C.6: Rheocurve of the mud bed at the beginning of the test (BOB-geometry).

Time series: run 1

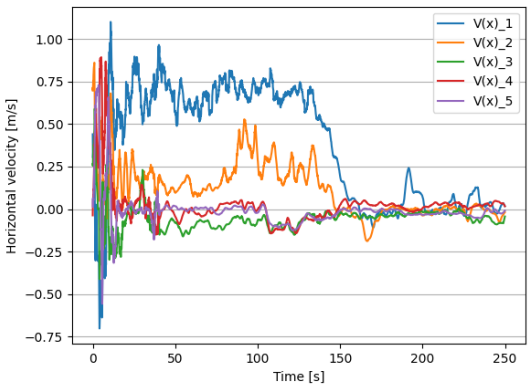

Figure C.7: Velocity signal at frame.

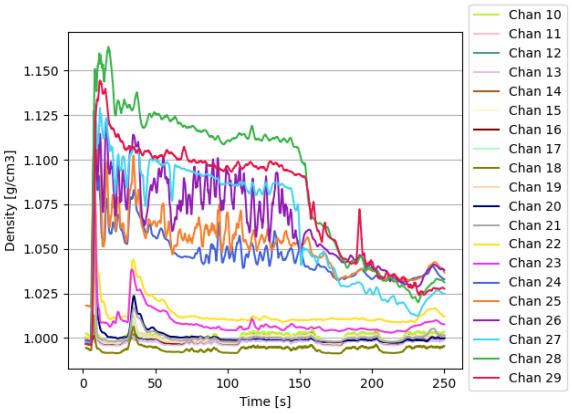

Figure C.8: Density signal at frame.

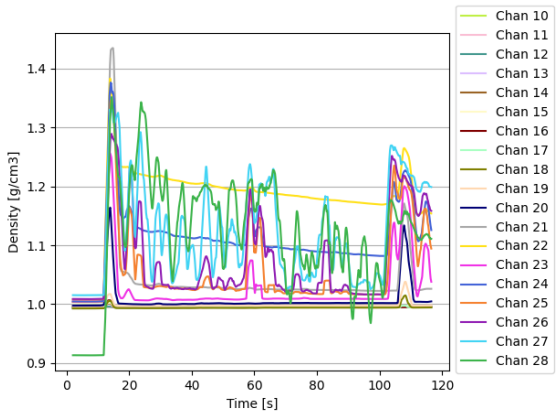

Figure C.9: Density signal behind jetbar.

Time series: run 2

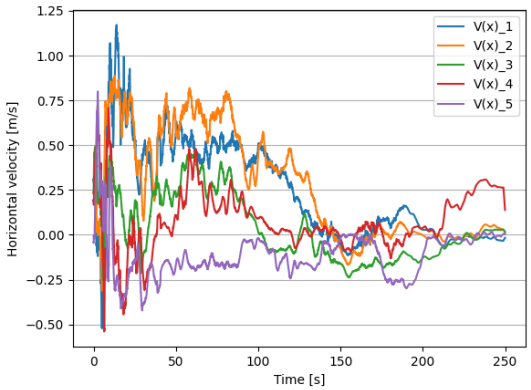

Figure C.10: Velocity signal at frame.

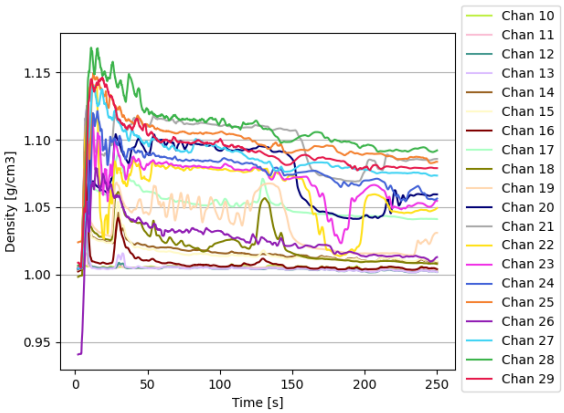

Figure C.11: Density signal at frame.

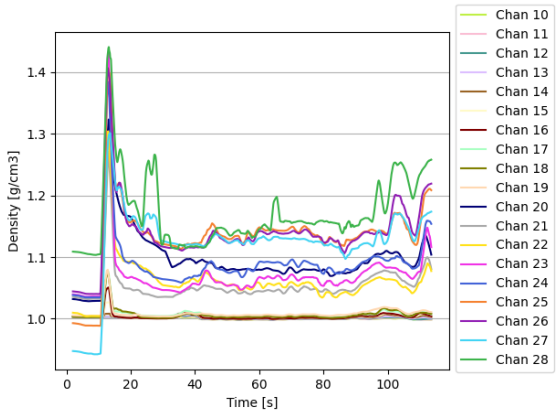

Figure C.12: Density signal behind jetbar.

Time series: run 3

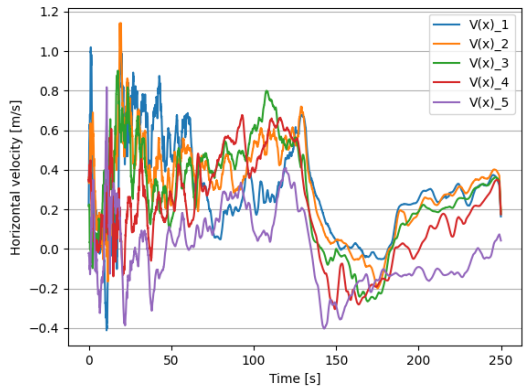

Figure C.13: Velocity signal at frame.

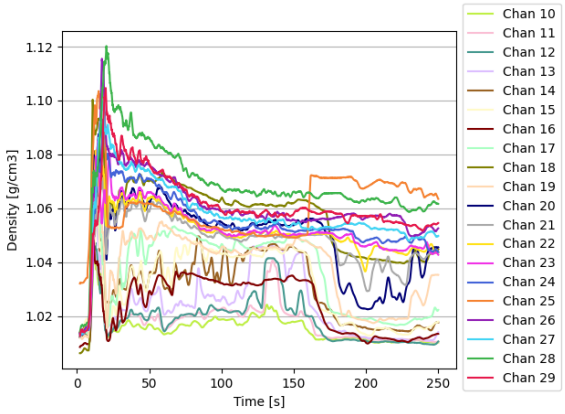

Figure C.14: Density signal at frame.

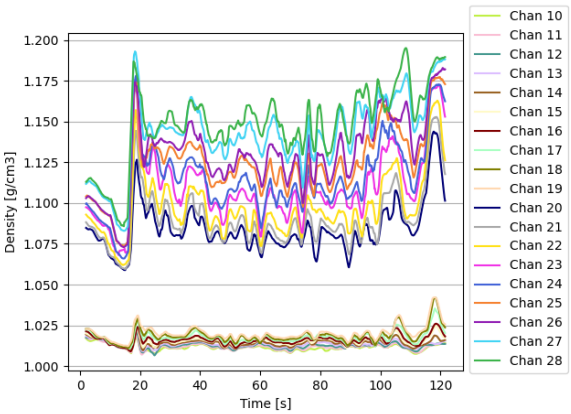

Figure C.15: Density signal behind jetbar.

Test 2

τ_B and D_n

During this test, τ_B is lower than the 100 Pa criteria and the bed only has an initial height of 0.40 to 0.45 m. This test was again done with a D_n of 35 mm, so the momentum of the jets was again larger than expected from the trial week. Because of the high momentum and low strength, a lot of production occurred and only two runs during this test could be conducted before touching the bottom of the flume.

SOD_r

A SOD_r of 70 mm is applied for both runs because during test 1 the jetbar touched something exactly at the moment it was above the measuring frame. Afraid to be damaging the measuring equipment, a SOD_r of 70 mm was applied to guarantee the safety of the equipment. After emptying the flume and placing the jetbar above the ramp, it was confirmed that a SOD_r of 10 mm was enough not to hit any of the equipment and during the following tests, a SOD_r of 10 mm during the first two or three runs was applied again.

Test results

In Figure C.16 the bed level after each run is plotted for this test. s_{intr} during this test was very high. This is probably caused by the low strength of the mud and high momentum of the jets. After run 1, almost all the mud was blown away. After run 2, some mud at 5 and 10 m from the ramp was still left. This was visually confirmed after removing the water on top. It was concluded therefore that the jets did not touch the bottom and s_{intr} at those points is still representative.

From the bed level data in Figure C.16 a stationary situation behind the jetbar is hard to identify. The profile of the bed after run 1 is nowhere horizontal. To still be able to estimate the production, s_{intr} only at 5 m from the ramp is taken as $s_{av,intr}$. Although this is a single point, in the results of later tests it is observed that at 5 m almost always a stationary situation occurs. Therefore, this assumption is used here as well.

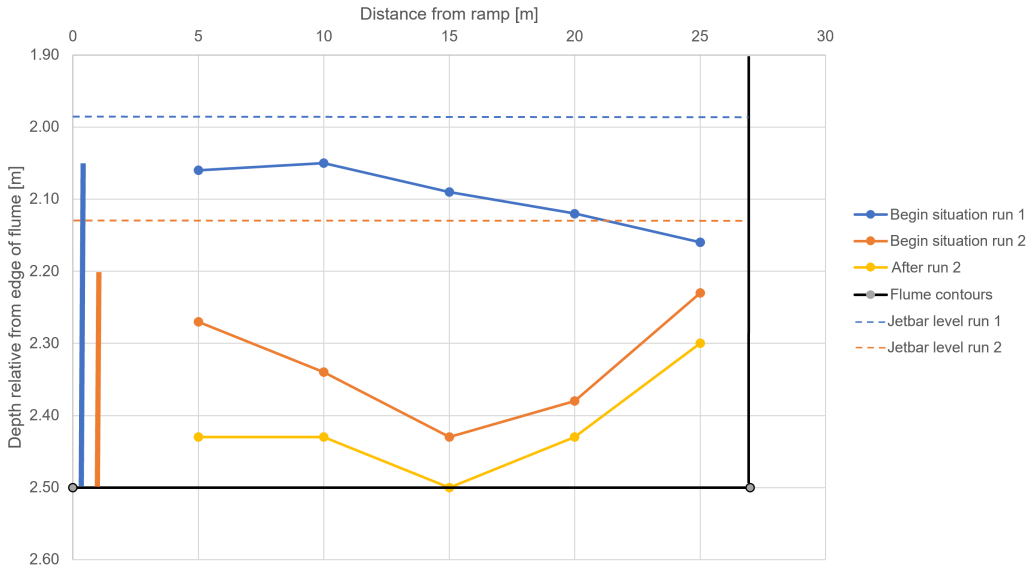

Figure C.16: Bed level after each run at different positions in the flume together with h_{ramp} (solid vertical line) and the level of the jetbar (horizontal dotted line) for test 2.

Table C.2 provides the time intervals over which is averaged to generate the flow velocity profiles and density profiles given in Figure 6.4 and 6.5. For a time interval of 50 - 75 seconds the jetbar runs from 20 to 27.1 meters in the flume.

	Time interval	
Run 1	50 - 75	s
Run 2	50 - 75	s

Table C.2: Averaged time intervals from the time series for plotting the flow velocity and density profiles.

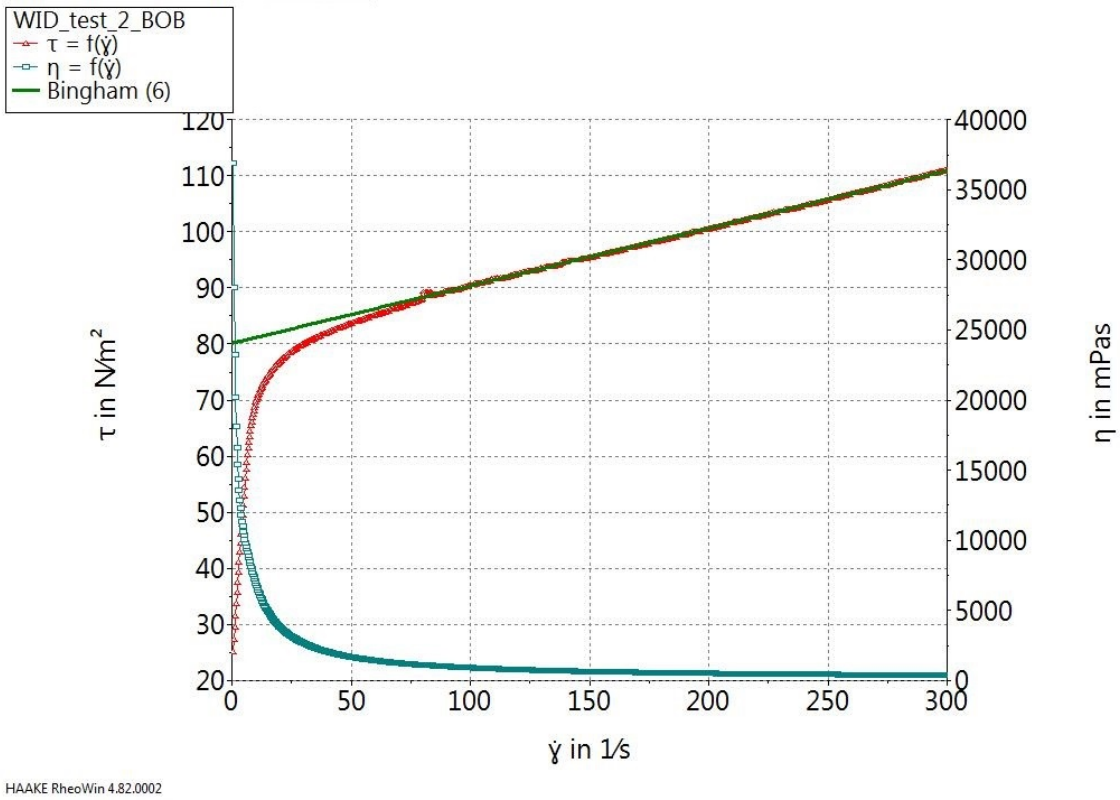

Figure C.17: Rheocurve of the mud bed at the beginning of the test (BOB-geometry).

Time series: run 1

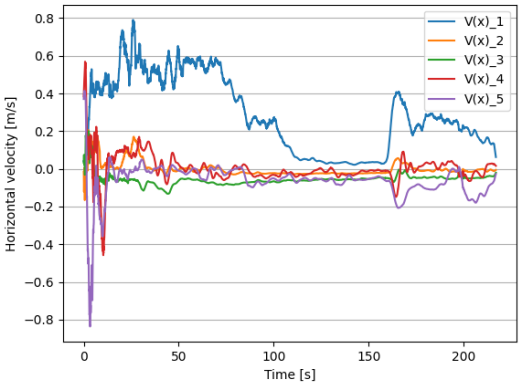

Figure C.18: Velocity signal at frame.

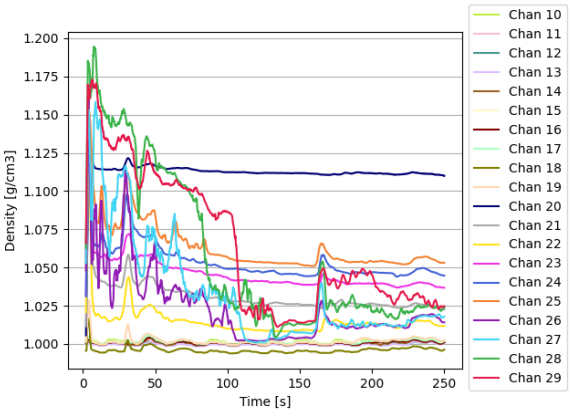

Figure C.19: Density signal at frame.

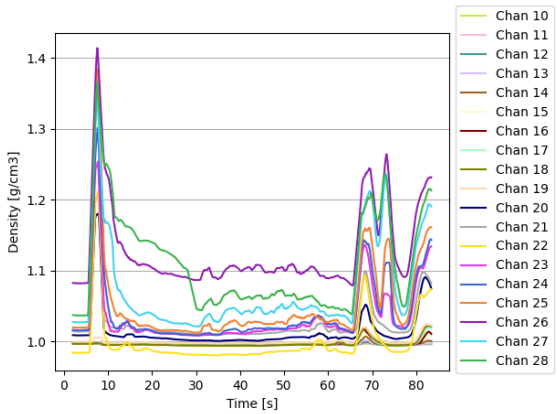

Figure C.20: Density signal behind jetbar.

Time series: run 2

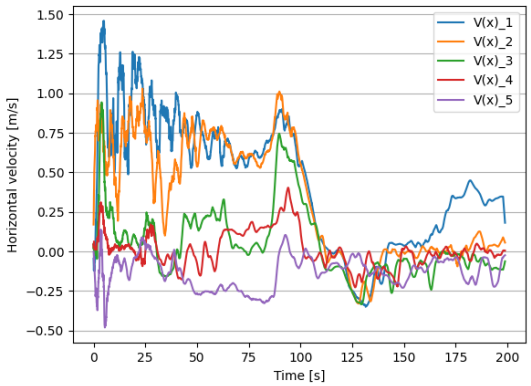

Figure C.21: Velocity signal at frame.

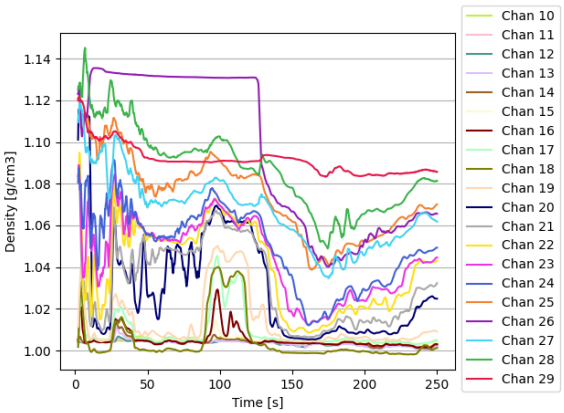

Figure C.22: Density signal at frame.

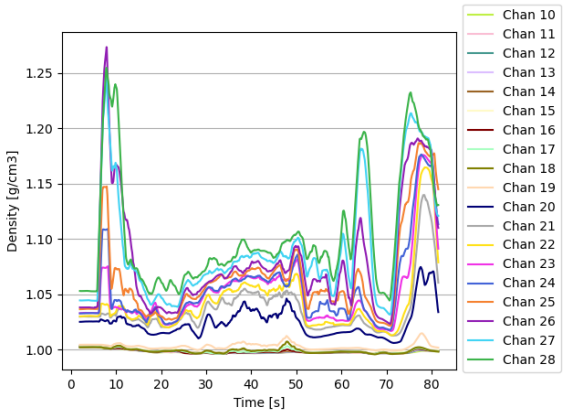

Figure C.23: Density signal behind jetbar.

Test 3

Test settings

τ_B of the mud during this test was higher than the criteria but still acceptable. D_n is now 20 mm because it was thought that in the previous tests a D_n of 30 mm was used and blew the mud away too much. To still make a sufficient number of runs during the following tests, D_n was therefore reduced.

During run 3 it was noticed that in order to reach a pressure of 1 bar out of the nozzles a higher frequency for the pump was needed. This was also the case during the fourth run. After emptying the flume, it was observed that a crack had formed in the middle of the jetbar. A possible explanation for this is that during the second run the jetbar hit the wall of the flume and caused a momenting force in the middle that was beyond the strength of the PVC. This was, however, not a problem since the leak was not directed towards the mud and a pressure of 1 bar could still be reached. Before the start of the fourth test, the leak was closed and stayed that way. This also explains the higher values of Q_t in the table of the parameter settings.

Test results

In Figure C.24 the bed level after each run is plotted for this test. Up to 15 m from the ramp a more or less stationary situation occurred behind the jetbar. The difference is not more than a couple of centimetres. $s_{av,intr}$ is determined for this stretch of the flume. Furthermore, the results show clearly that with an increasing number of runs, s_{intr} increases as well. This was also observed during other experimental studies on WID. Again, at 20 m after every run, the depth is much larger. The same reason is given as for the previous tests.

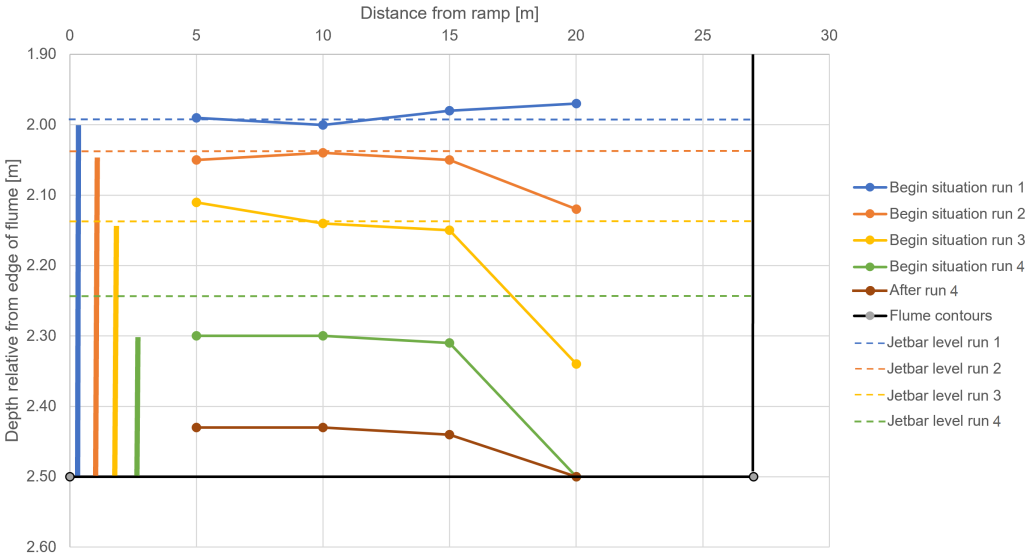

Figure C.24: Bed level after each run at different positions in the flume together with h_{ramp} (solid vertical line) and the level of the jetbar (horizontal dotted line) for test 3.

Table C.3 provides the time intervals over which is averaged to generate the flow velocity profiles and density profiles given in Figure 6.6 to 6.8. For a time interval of 30 - 40 seconds, the jetbar runs from 12 to 16 meters in the flume. For a time interval of 50 - 50 seconds, the jetbar runs from 20 to 24 meters in the flume and for a time interval of 30 - 70 seconds, the jetbar runs from 12 to 27.1 meters in the flume.

	Time interval	
Run 1	30 - 40	s
Run 2	50 - 60	s
Run 3	50 - 60	s
Run 4	30 - 70	s

Table C.3: Averaged time intervals from the time series for plotting the flow velocity and density profiles.

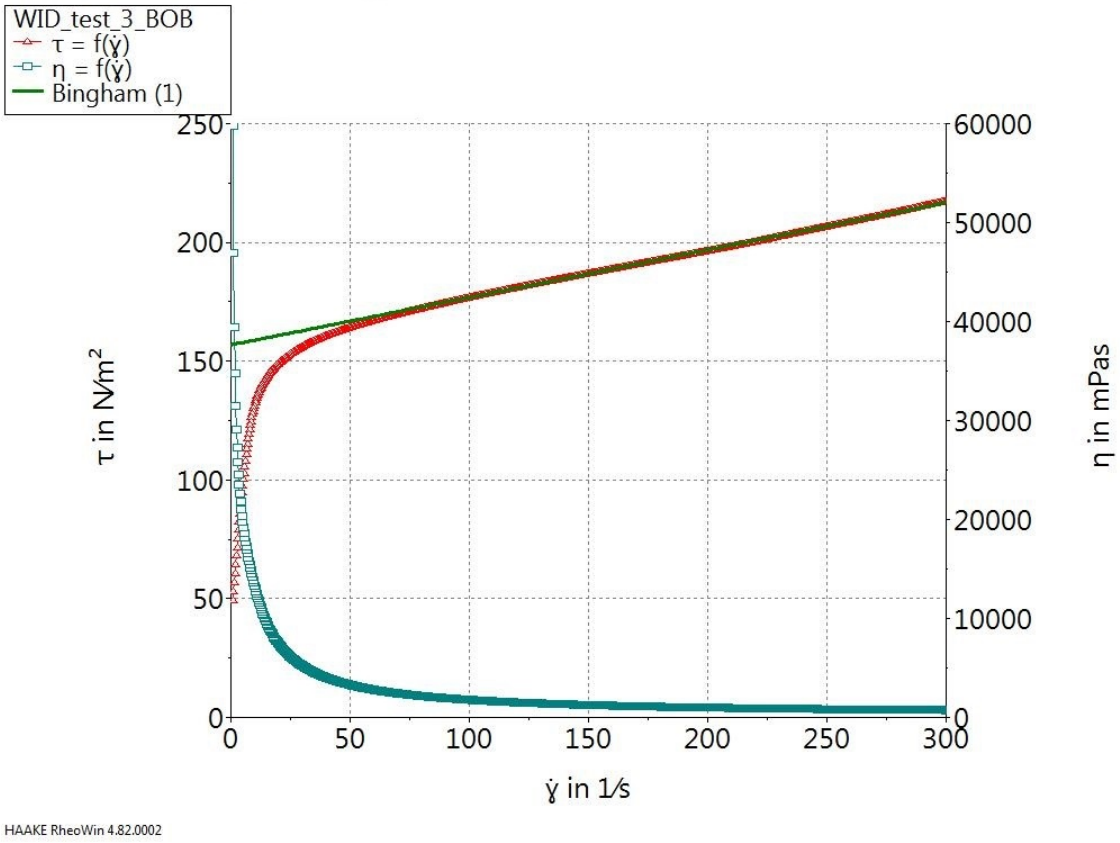

Figure C.25: Rheocurve of the mud bed at the beginning of the test (BOB-geometry).

Time series: run 1

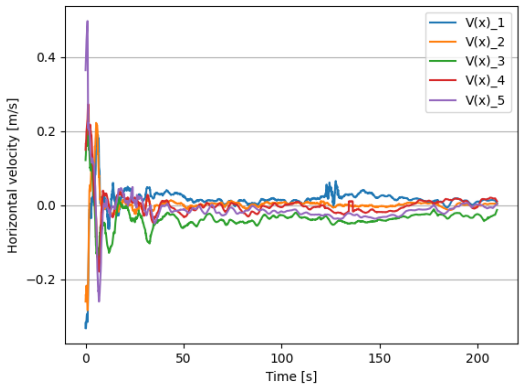

Figure C.26: Velocity signal at frame.

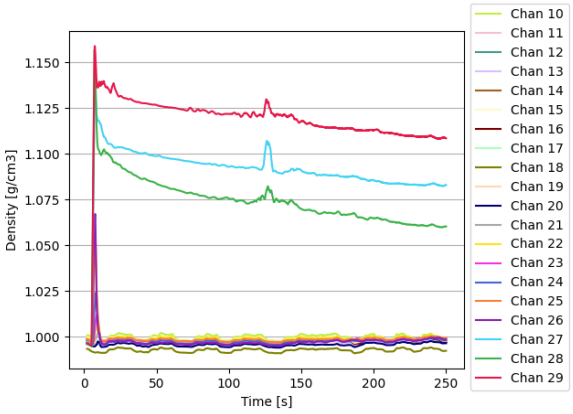

Figure C.27: Density signal at frame.

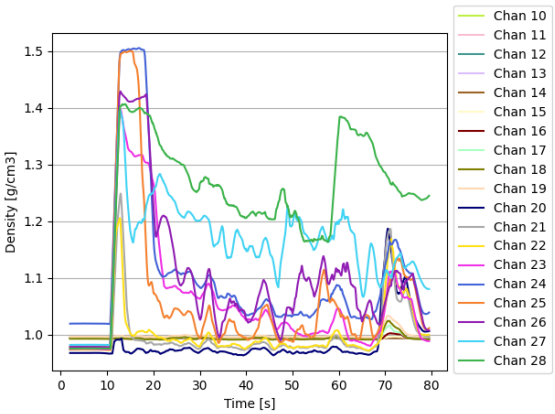

Figure C.28: Density signal behind jetbar.

Time series: run 2

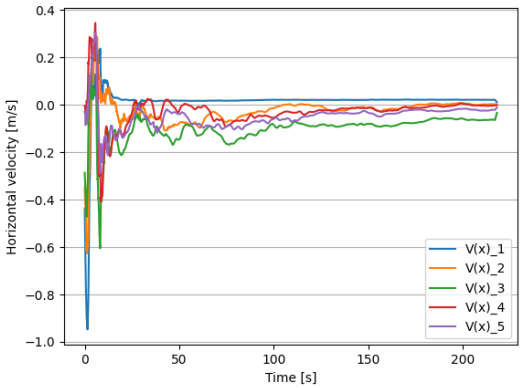

Figure C.29: Velocity signal at frame.

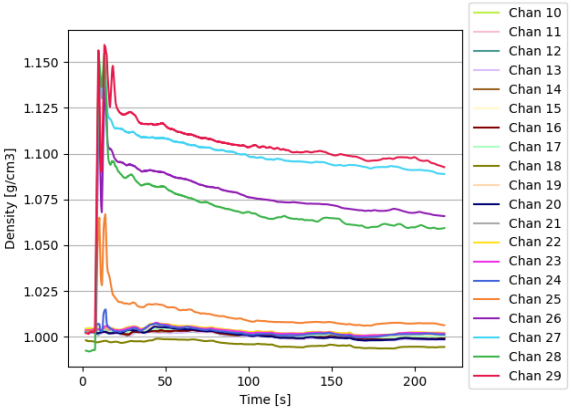

Figure C.30: Density signal at frame.

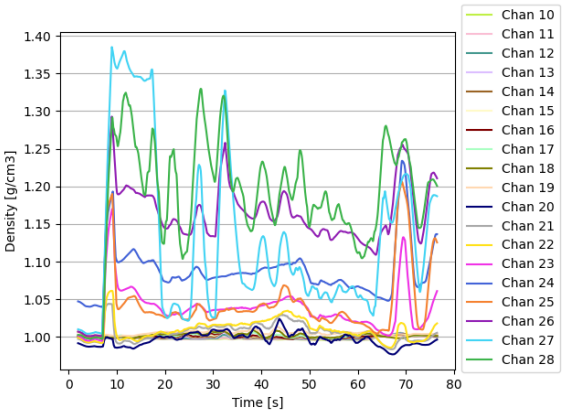

Figure C.31: Density signal behind jetbar.

Time series: run 3

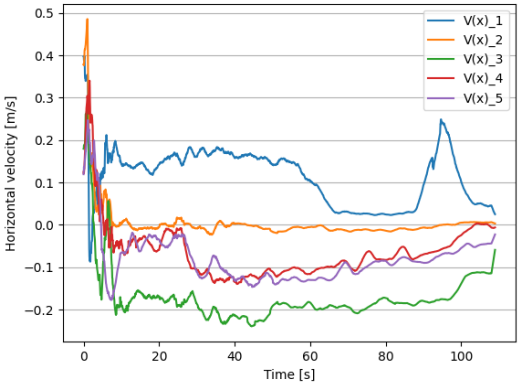

Figure C.32: Velocity signal at frame.

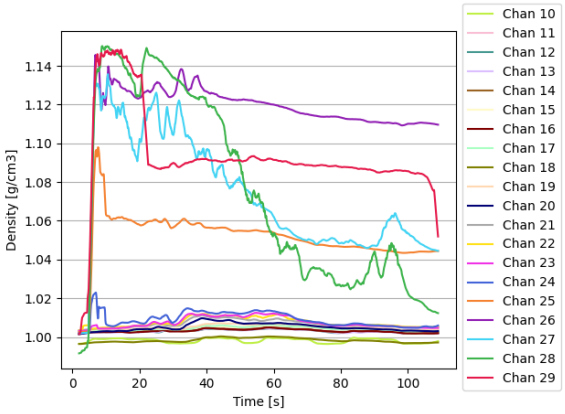

Figure C.33: Density signal at frame.

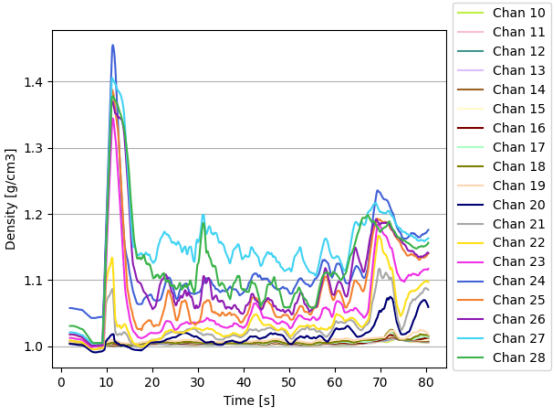

Figure C.34: Density signal behind jetbar.

Time series: run 4

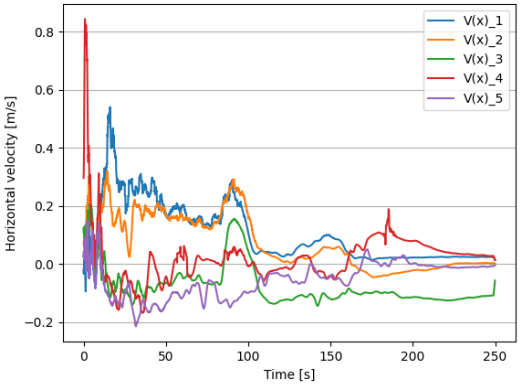

Figure C.35: Velocity signal at frame.

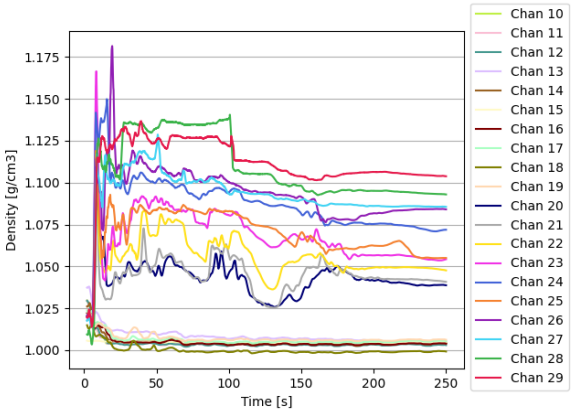

Figure C.36: Density signal at frame.

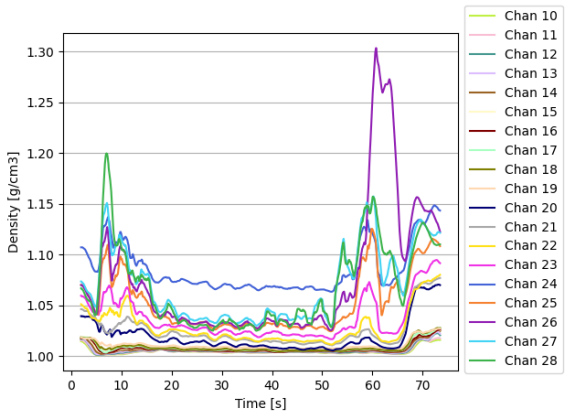

Figure C.37: Density signal behind jetbar.

Test 4

Test settings

τ_B during this test (237.2 Pa) was more than two times the strength criteria (100 Pa). As was mentioned in Section 5.5 the rheology of the material could only be accurately determined at Deltares after the flume was already filled with the material. It could not be mixed with water to reduce the strength because there were no tools available which could mix a layer of only 0.5 m high of mud with a volume of around 30 m^3. Still, because a relatively low v_t and high p_j were applied, which in theory would give the highest s_{intr}, a high strength should not necessarily impose a problem on the results.

According to the discharge measuring device, Q_t during the first run was very high. The device did not work properly during this run. After rebooting the system, the device worked properly for the other runs. Q_t of the first run is not taken into account in the results, but instead a value of 69 L/s was used in the post-processing.

Test results

In Figure C.38 the bed level after each run is plotted for this test. Again, up to 10 m from the ramp, a more or less stationary situation occurred behind the jetbar and is therefore used for $s_{av,intr}$. Probably as a result of the relatively high strength of the mud, a layer of around 200 mm was left after run 3. A fourth run was not done, because, looking at the results of the previous runs, it was expected that the jets would hit the bottom floor and would thus not result in reliable production.

Table C.4 provides the time intervals over which is averaged to generate the flow velocity profiles and density profiles given in Figure 6.10 to 6.12. For a time interval of 50 - 75 seconds, the jetbar runs from 12.5 to 27.1 meters in the flume.

	Time interval	
Run 1	50 - 75	s
Run 2	50 - 75	s
Run 3	50 - 75	s

Table C.4: Averaged time intervals from the time series for plotting the flow velocity and density profiles.

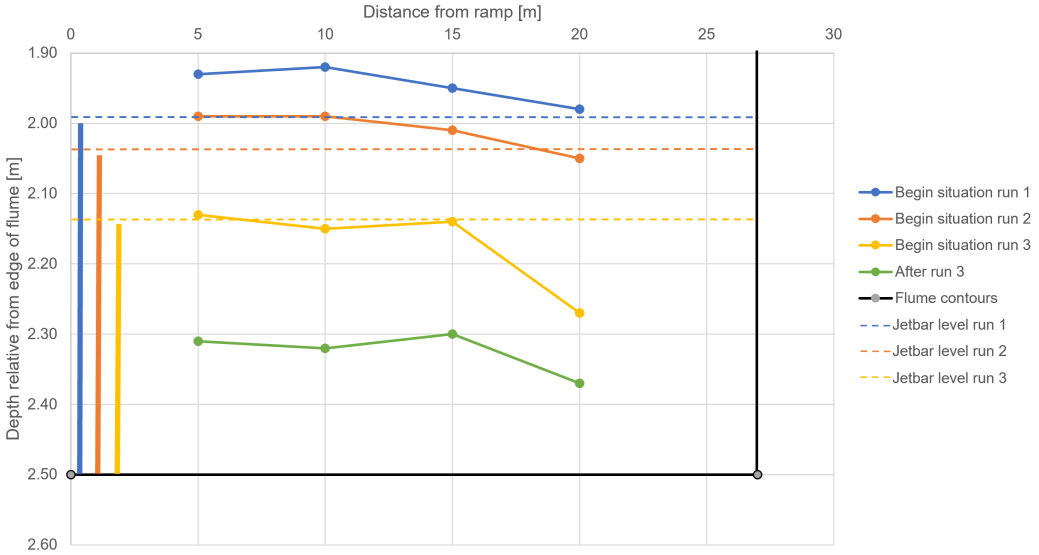

Figure C.38: Bed level after each run at different positions in the flume together with h_{ramp} (solid vertical line) and the level of the jetbar (horizontal dotted line) for test 4.

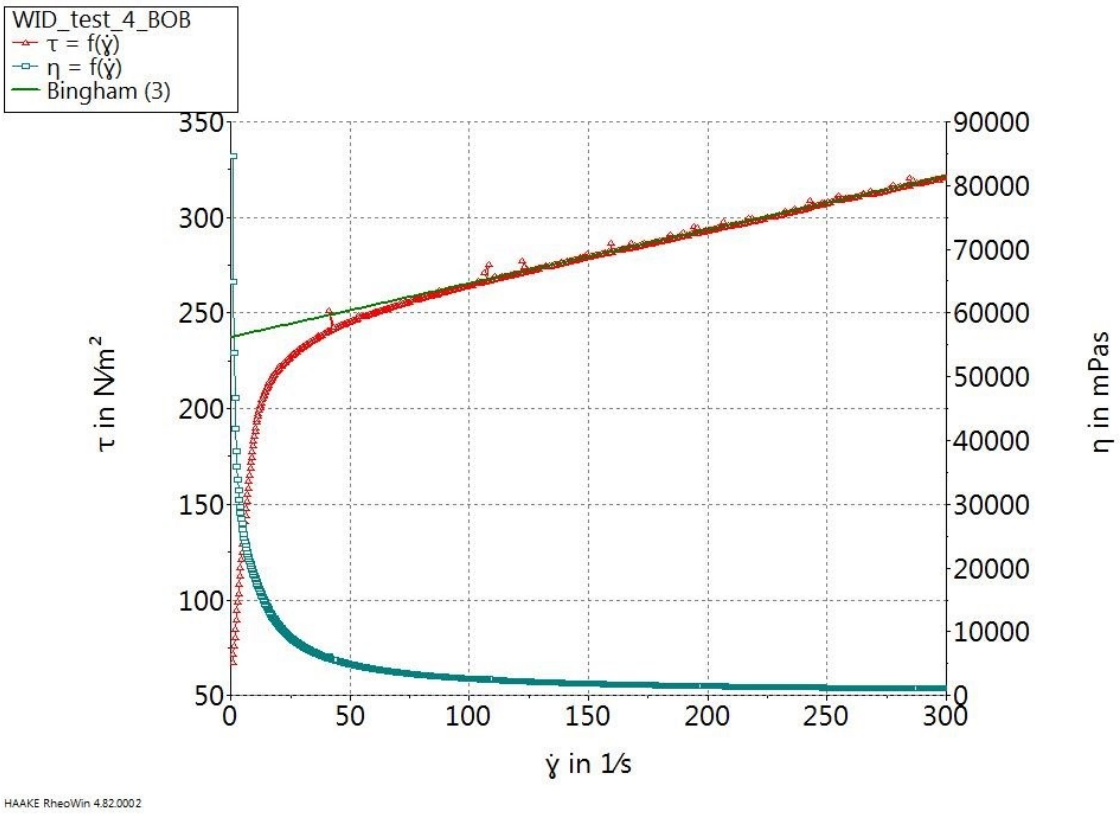

Figure C.39: Rheocurve of the mud bed at the beginning of the test (BOB-geometry).

Time series: run 1

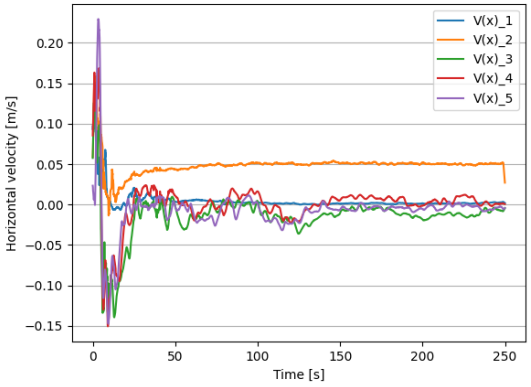

Figure C.40: Velocity signal at frame.

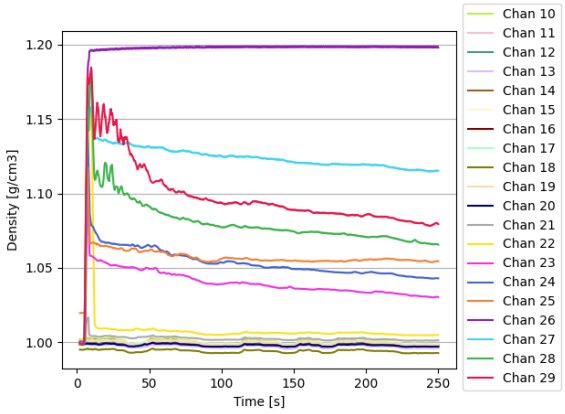

Figure C.41: Density signal at frame.

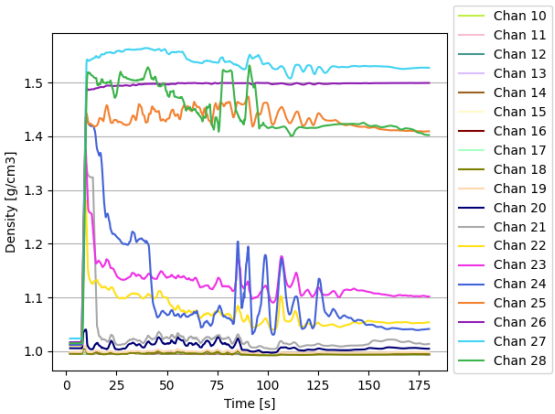

Figure C.42: Density signal behind jetbar.

Time series: run 2

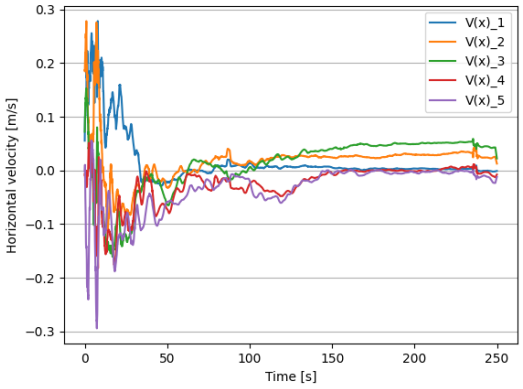

Figure C.43: Velocity signal at frame.

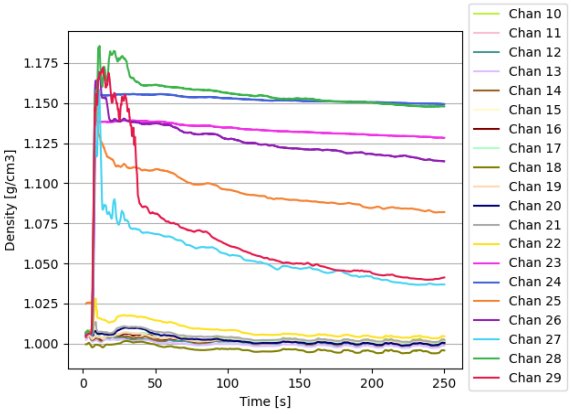

Figure C.44: Density signal at frame.

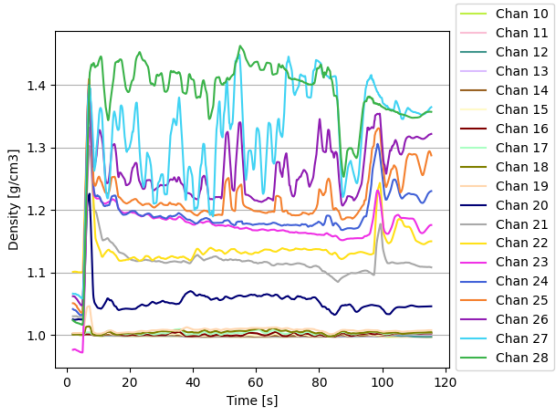

Figure C.45: Density signal behind jetbar.

Time series: run 3

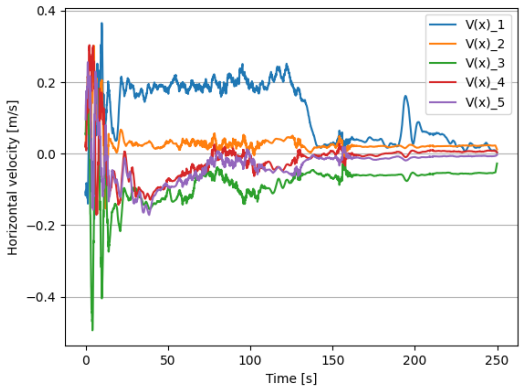

Figure C.46: Velocity signal at frame.

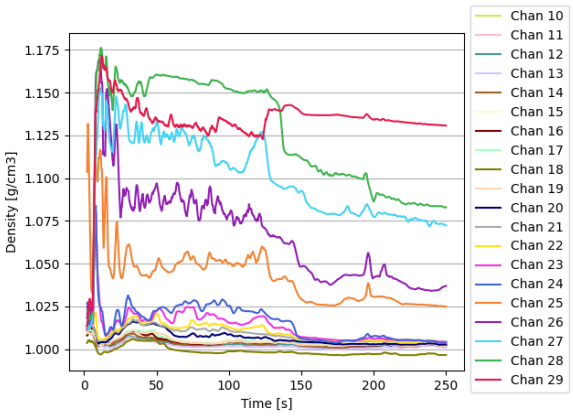

Figure C.47: Density signal at frame.

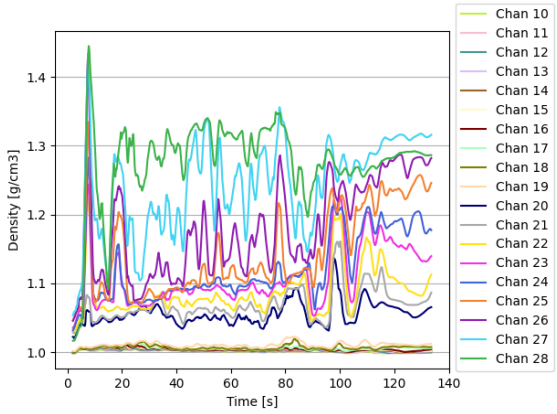

Figure C.48: Density signal behind jetbar.

Test 5

Test settings

During this test, the properties of the mud did not exceed the criteria too much (τ_B = 132.7 Pa). During the first run, Q_t was again very high according to the discharge measuring device. Again, after a reboot before the next runs, it worked fine. Also, this measurement was not processed in the cumulative results but corrected with a value close to one of the other runs.

As was discussed before, this test should have had a SOD_r of around 400 mm, but 0 mm was used. To make a good comparison between tests with a D_n of 20 mm, a test with p_j = 0.5 bar and v_t = 0.25 or 0.4 m/s had to be done. This test, therefore, was used to apply v_t = 0.25 m/s.

Test results

In Figure C.49 the bed level after each run is plotted for this test. Again, the distance between 5 and 10 m from the ramp shows a stationary situation in the bed. At 15 m, an accumulation of sediment is observed in the data which grows with every run. This is probably caused by the jetbar which stays pumping sediment for around 7 à 8 seconds at 20 m, but can not be said for sure since the water was too turbid to observe anything at that depth.

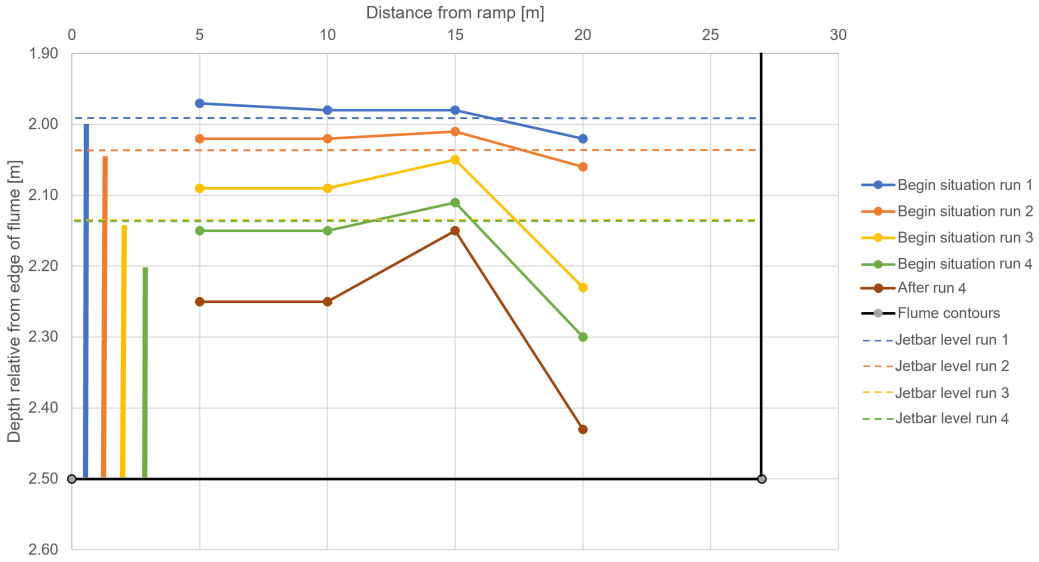

Figure C.49: Bed level after each run at different positions in the flume together with h_{ramp} (solid vertical line) and the level of the jetbar (horizontal dotted line) for test 5.

Table C.5 provides the time intervals over which is averaged to generate the flow velocity profiles and density profiles given in Figure 6.13 to 6.16. For a time interval of 50 - 75 seconds the jetbar runs from 12.5 to 27.1 meters in the flume.

	Time interval	
Run 1	50 - 75	s
Run 2	50 - 75	s
Run 3	50 - 75	s
Run 4	50 - 75	s

Table C.5: Averaged time intervals from the time series for plotting the flow velocity and density profiles.

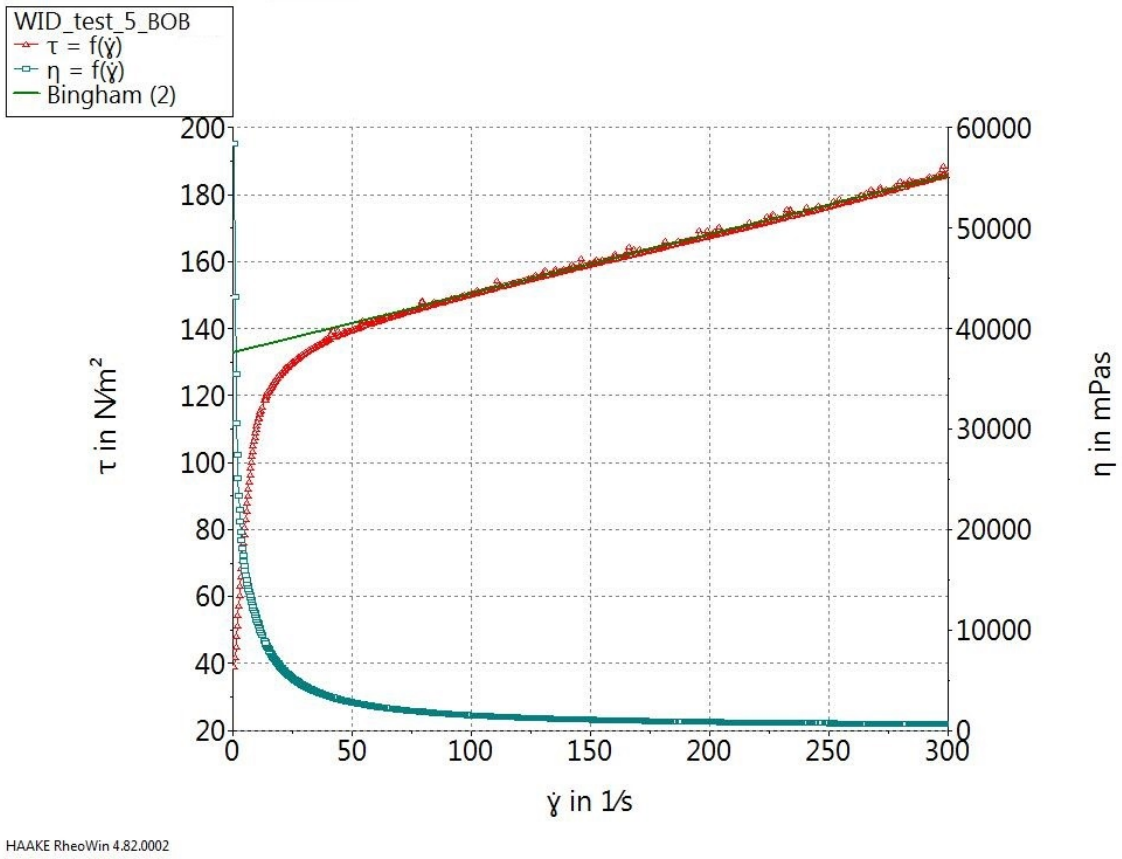

Figure C.50: Rheocurve of the mud bed at the beginning of the test (BOB-geometry).

Time series: run 1

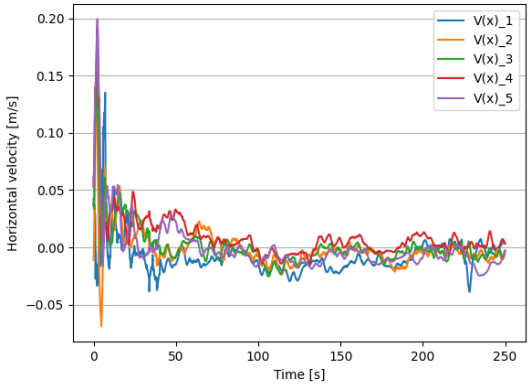

Figure C.51: Velocity signal at frame.

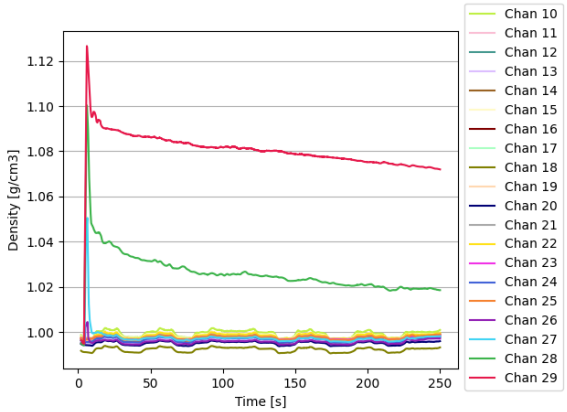

Figure C.52: Density signal at frame.

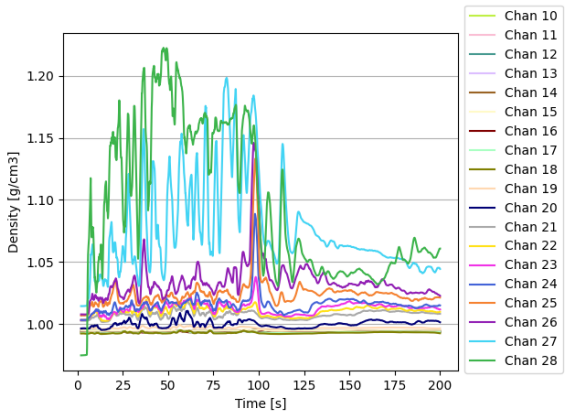

Figure C.53: Density signal behind jetbar.

Time series: run 2

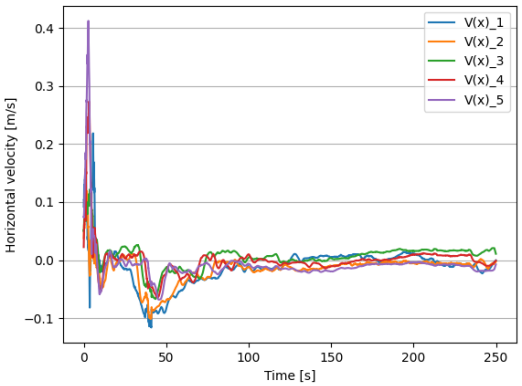

Figure C.54: Velocity signal at frame.

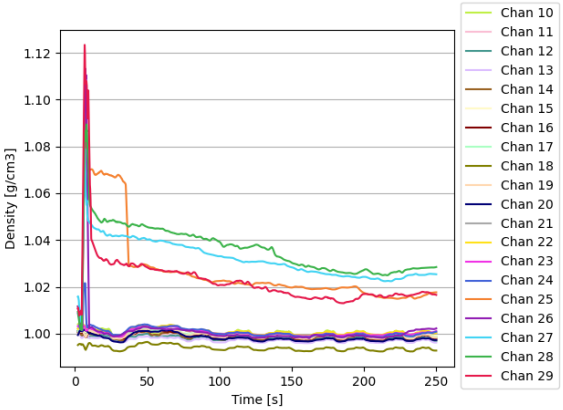

Figure C.55: Density signal at frame.

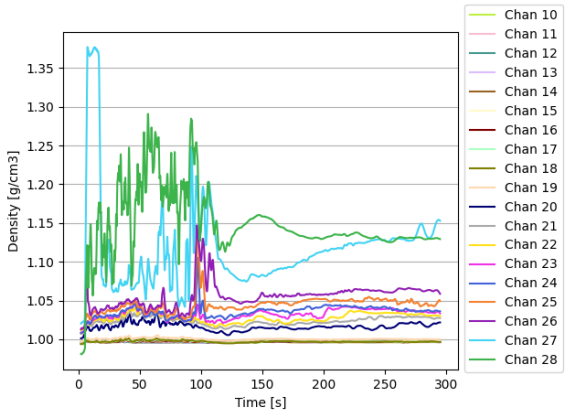

Figure C.56: Density signal behind jetbar.

Time series: run 3

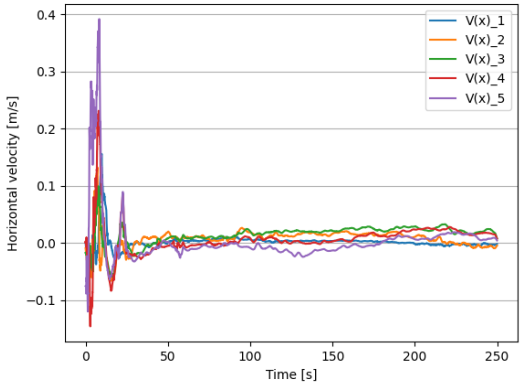

Figure C.57: Velocity signal at frame.

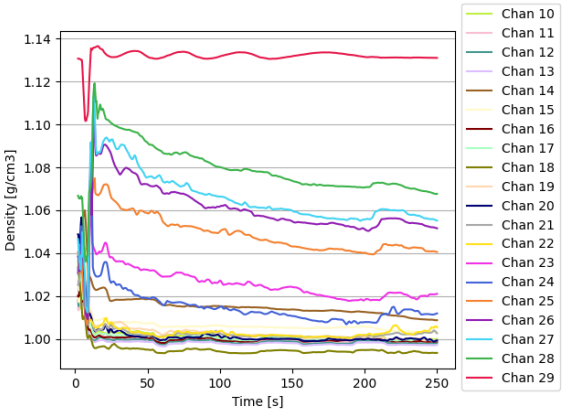

Figure C.58: Density signal at frame.

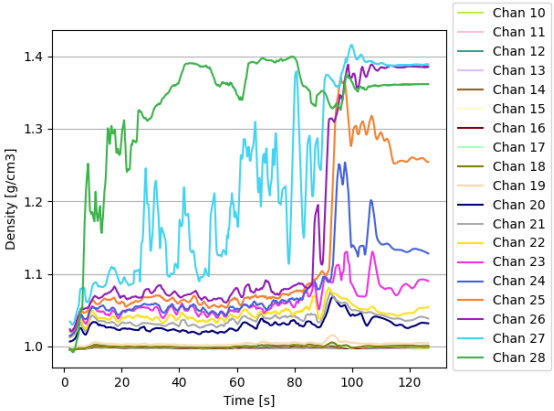

Figure C.59: Density signal behind jetbar.

Time series: run 4

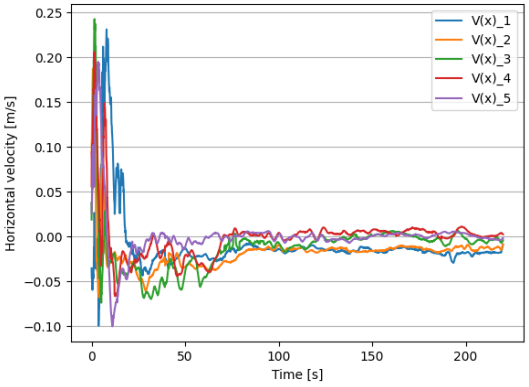

Figure C.60: Velocity signal at frame.

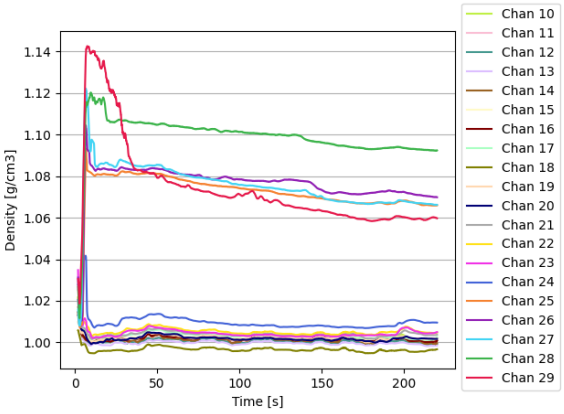

Figure C.61: Density signal at frame.

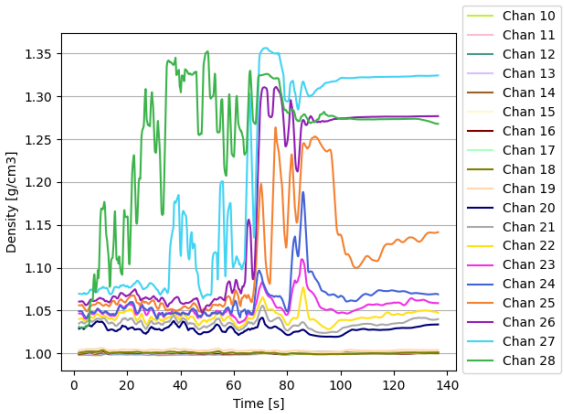

Figure C.62: Density signal behind jetbar.

Test 6

Test settings

During this test a SOD_r of 300 mm was applied to the process for runs 1, 2 and 4. This was done to see the influence of the SOD_r on the production as was discussed earlier. Also, not 400 but 300 mm was applied eventually because it was thought that 400 mm would be too far into the region of fully developed flow of the jets to have a significant and measurable impact on the mud. During run 3, a SOD_r of 60 mm was applied to see, during the test itself, if a variation in SOD_r would make a big difference or not.

Test results

Figure C.63 shows after run 3 a significant production increase compared to the other runs with a higher SOD_r. Furthermore, Figure C.63 shows that between 5 and 10 m from the ramp a stationary situation occurred behind the jets and thus is taken for $s_{av,intr}$. At 15 m from the ramp, a significant decrease in bed level occurs.

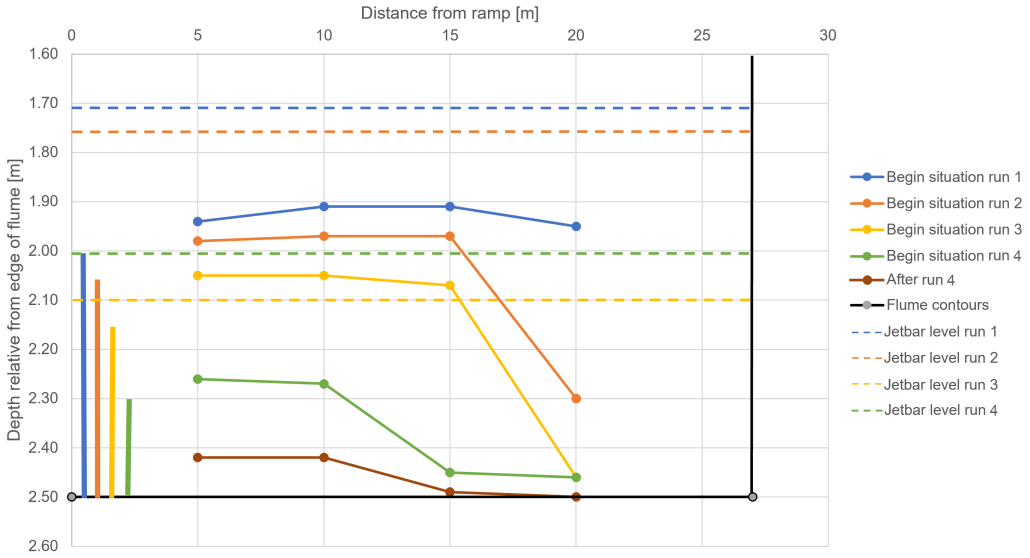

Figure C.63: Bed level after each run at different positions in the flume together with h_{ramp} (solid vertical line) and the level of the jetbar (horizontal dotted line) for test 6.

Table C.6 provides the time intervals over which is averaged to generate the flow velocity profiles and density profiles given in Figure 6.17 to 6.20. For a time interval of 40 - 70 seconds, the jetbar runs from

10 to 17.5 meters in the flume and for a time interval of 50 - 75 seconds, the jetbar runs from 12.5 to 27.1 meters in the flume.

	Time interval	
Run 1	40 - 70	s
Run 2	50 - 75	s
Run 3	50 - 75	s
Run 4	50 - 75	s

Table C.6: Averaged time intervals from the time series for plotting the flow velocity and density profiles.

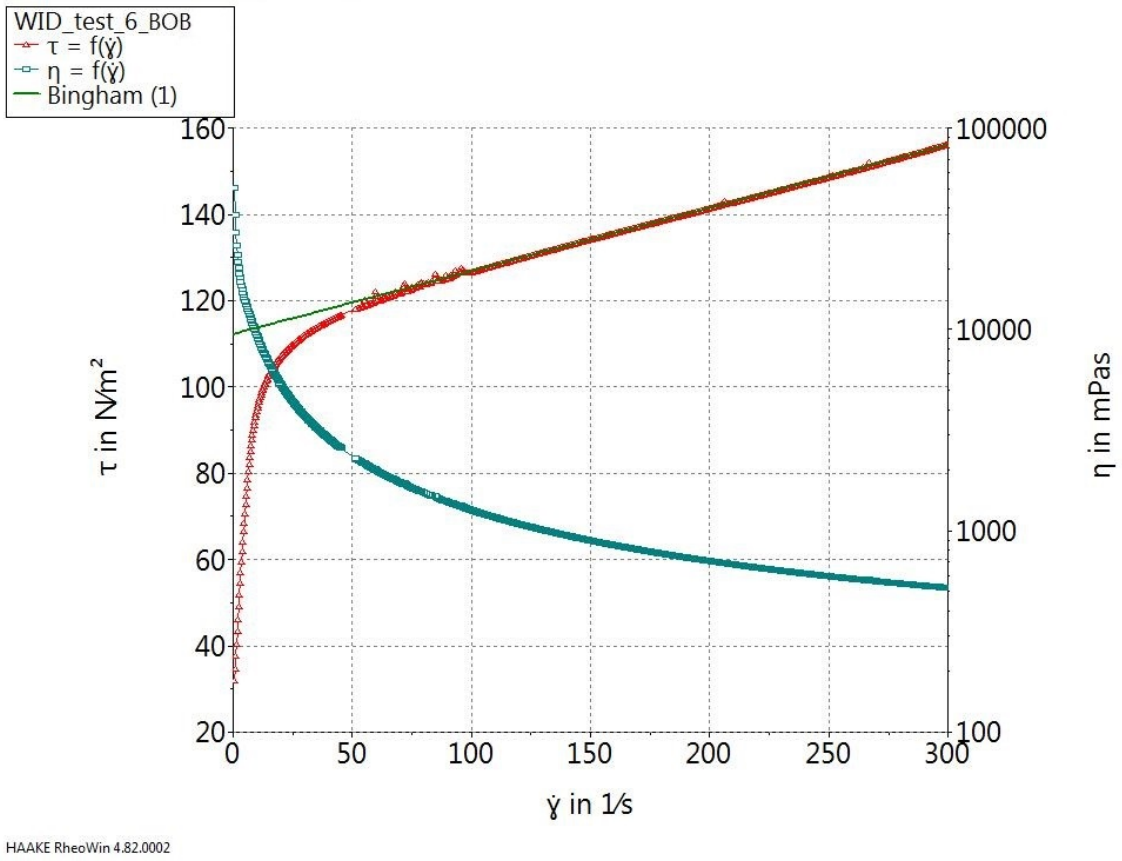

Figure C.64: Rheocurve of the mud bed at the beginning of the test (BOB-geometry).

Time series: run 1

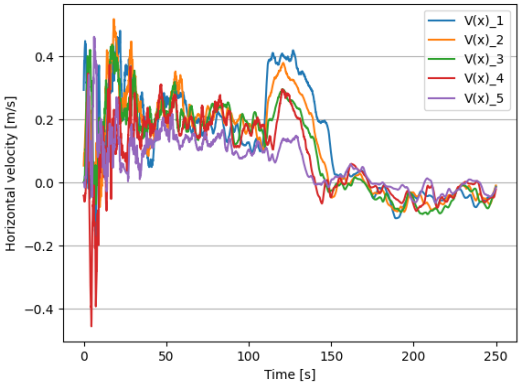

Figure C.65: Velocity signal at frame.

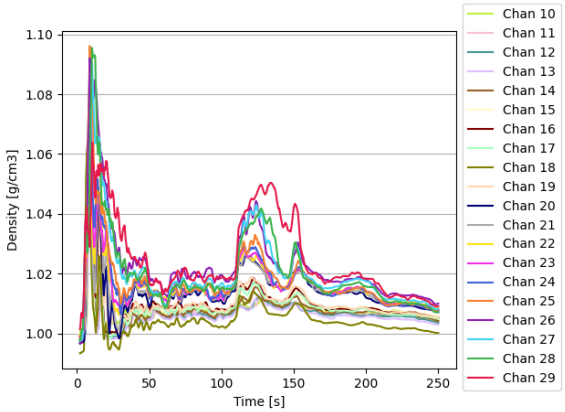

Figure C.66: Density signal at frame.

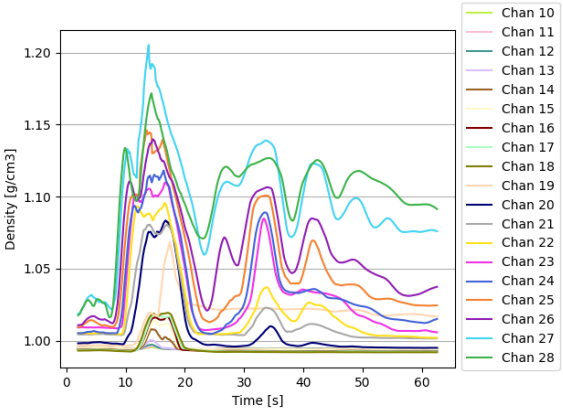

Figure C.67: Density signal behind jetbar.

Time series: run 2

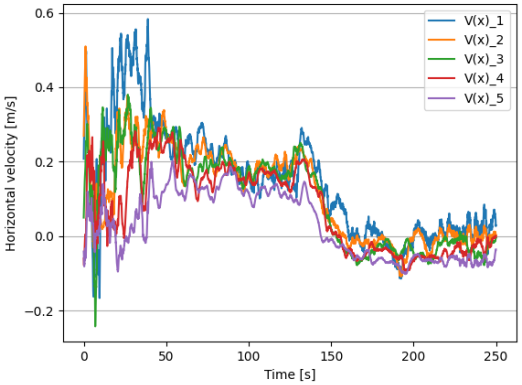

Figure C.68: Velocity signal at frame.

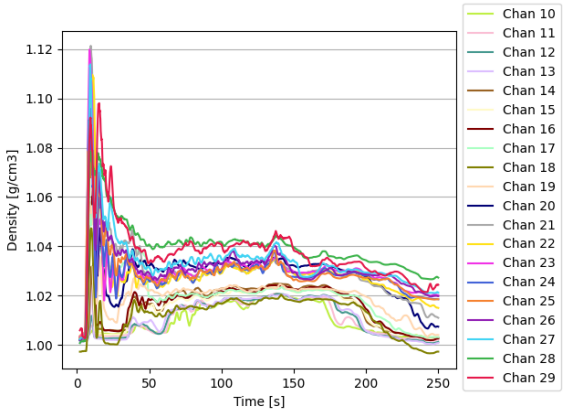

Figure C.69: Density signal at frame.

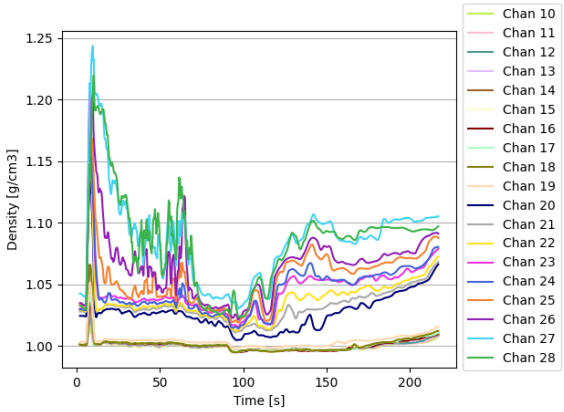

Figure C.70: Density signal behind jetbar.

Time series: run 3

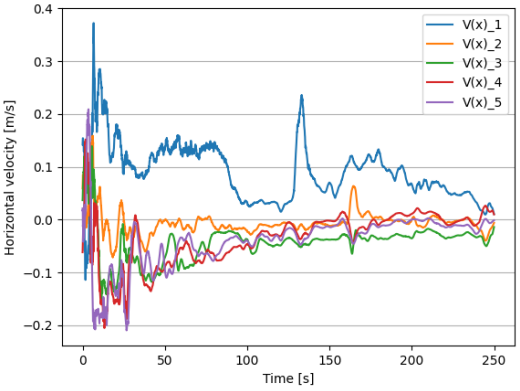

Figure C.71: Velocity signal at frame.

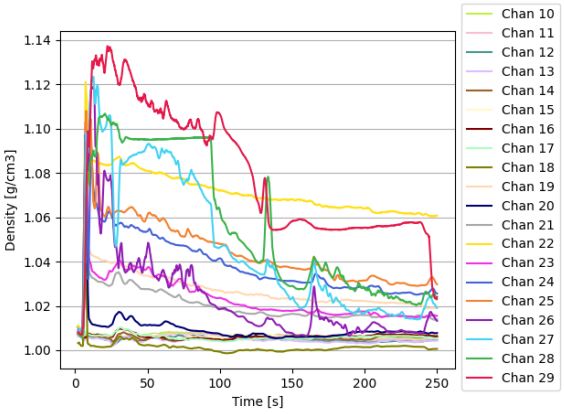

Figure C.72: Density signal at frame.

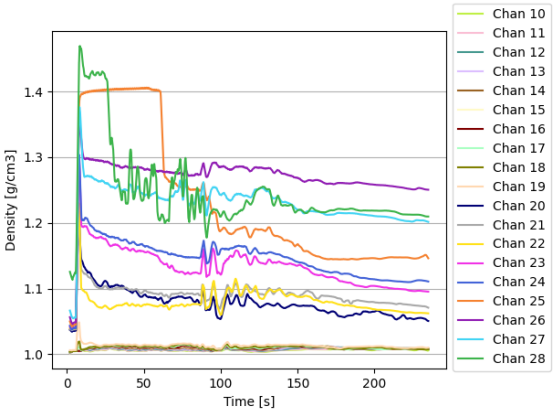

Figure C.73: Density signal behind jetbar.

Time series: run 4

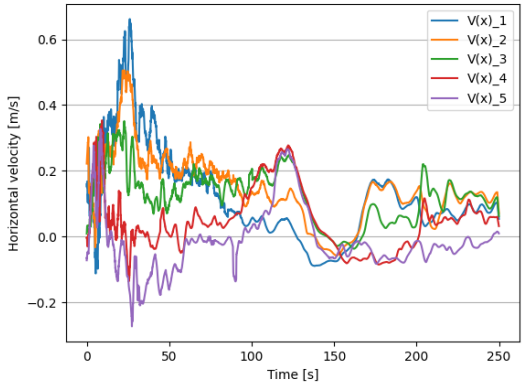

Figure C.74: Velocity signal at frame.

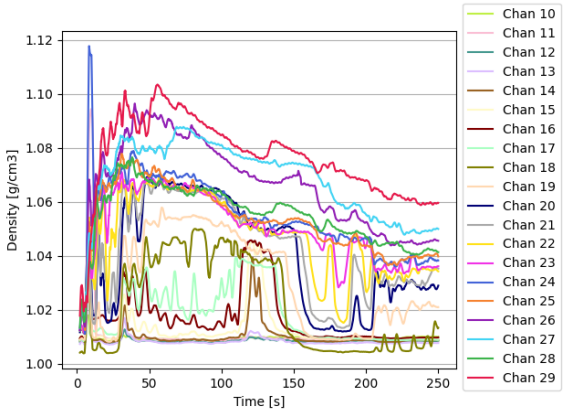

Figure C.75: Density signal at frame.

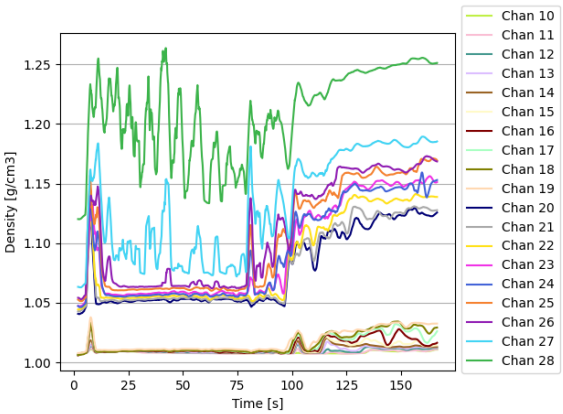

Figure C.76: Density signal behind jetbar.

Appendix D
Water density correction

During the experiments, the mud containing salt pore water is injected with fresh water. This causes the salinity of the suspension to be lower than the salinity of the undisturbed bed. To determine the SSC, the difference between ρ_m and ρ_w is of influence. Using the density of salt water ($\rho_w \approx 1025$ kg/m^3) to determine the SSC of the density current for different densities would provide misleading concentrations, especially when ρ_m is close to 1025 kg/m^3.

A series of dilutions with fresh water has been made on mud from the Calandkanaal. With every dilution, the density of the mixture was measured with a DMA 35. Initially, ρ_w = 1025 kg/m^3 is assumed for the pore water of the undisturbed mud and values of ρ_w of the dilutions were calculated according to the dilution ratio. All values are given in Table D.1. ρ_m is plotted as a function of ρ_w in Figure D.1. The boundaries for correction of ρ_w are given below from this figure. If e.g. ρ_m < 1050 kg/m^3 it is save to use ρ_w = 1000 kg/m^3.

		ρ_m	≤	1050 kg/m^3 → ρ_w = 1000 kg/m^3
1050 kg/m^3	<	ρ_m	≤	1100 kg/m^3 → ρ_w = 1005 kg/m^3
1100 kg/m^3	<	ρ_m	<	1150 kg/m^3 → ρ_w = 1010 kg/m^3
1150 kg/m^3	≤	ρ_m	<	1200 kg/m^3 → ρ_w = 1015 kg/m^3
		ρ_m	>	1200 kg/m^3 → ρ_w = 1025 kg/m^3

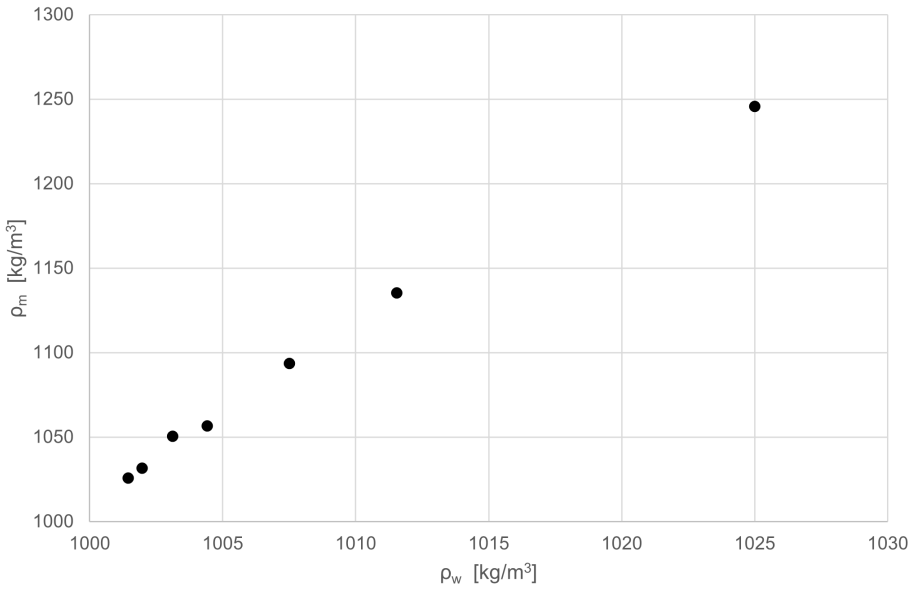

Figure D.1: ρ_b as a function of ρ_w for a certain dilution range.

Dilution ratio	ρ_m [kg/m^3]	ρ_w [kg/m^3]
1:0	1245.6	1025
1:1	1135.2	1011.50
1:2	1093.7	1007.49
1:4	1056.7	1004.41
1:6	1050.5	1003.12
1:10	1031.5	1001.97
1:14	1025.8	1001.44

Table D.1: Dilution ratios and measured corresponding ρ_m.

Appendix E
Echo sounding data

This appendix presents the sounding profiles from the duo frequency echo sounder made during test 1 to 6. The details of the echo sounder used for this study are given in Section 5.8.5. Although this data is not used during the analysis of this study due to its insufficient quality, it is still presented to let the reader judge the quality as well.

During every sounding, the concrete bottom floor is 1.5 meters below the 0 m level of the echo sounder. The position of the ramp can be quite clearly identified in most figures, as it is most often a clear height difference. Furthermore, the red lines correspond to 200 kHz and the green lines to 38 kHz.

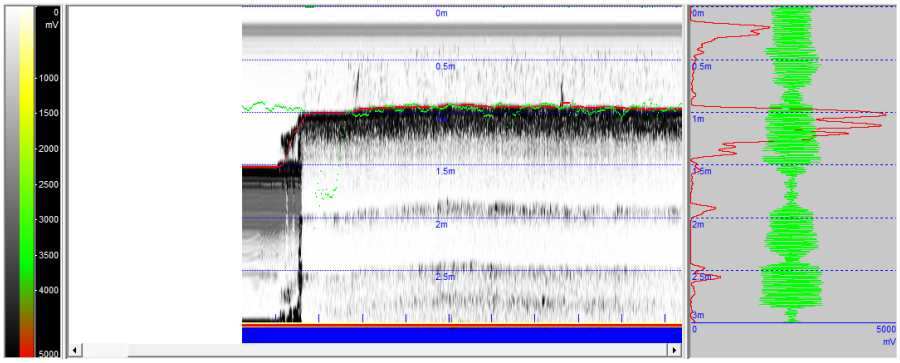

Figure E.1: Test 1: echo sounding profile made before the execution of run 1. v_t = 0.25 m/s, D_n = 35 mm, p_j = 0.51 bar, SOD_r = 10 mm, SOD_b = -60 mm, τ_b = 118.2 Pa.

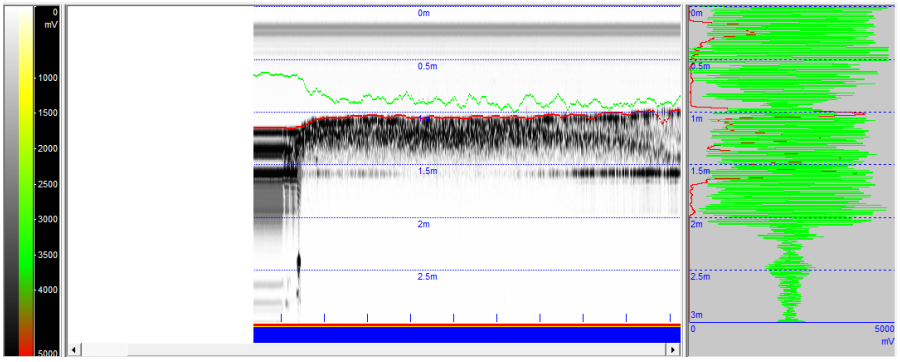

Figure E.2: Test 1: echo sounding profile made before the execution of run 2. v_t = 0.25 m/s, D_n = 35 mm, p_j = 0.52 bar, SOD_r = 10 mm, SOD_b = -60 mm, τ_b = 118.2 Pa.

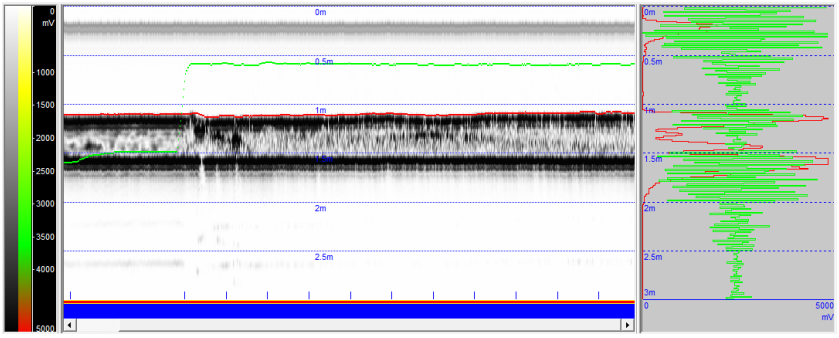

Figure E.3: Test 1: echo sounding profile made before the execution of run 3. v_t = 0.25 m/s, D_n = 35 mm, p_j = 0.53 bar, SOD_r = 50 mm, SOD_b = 10 mm, τ_b = 118.2 Pa.

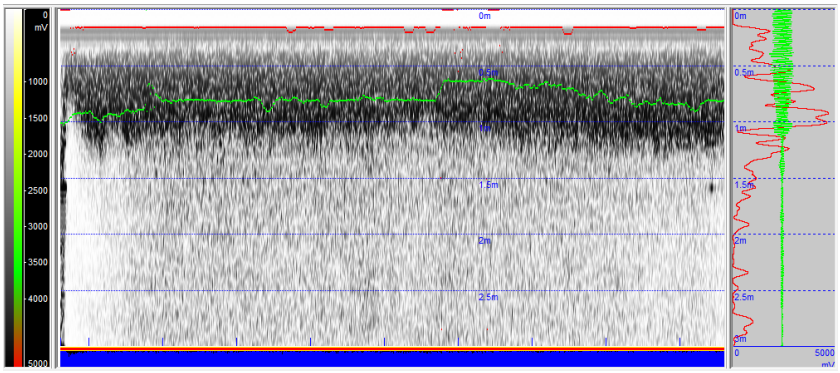

Figure E.4: Test 1: echo sounding profile made during the execution of run 1. v_t = 0.25 m/s, D_n = 35 mm, p_j = 0.51 bar, SOD_r = 10 mm, SOD_b = -60 mm, τ_b = 118.2 Pa.

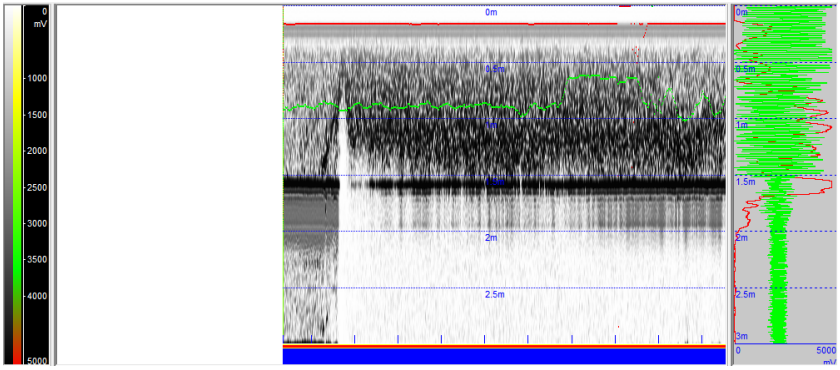

Figure E.5: Test 1: echo sounding profile made during the execution of run 2. v_t = 0.25 m/s, D_n = 35 mm, p_j = 0.52 bar, SOD_r = 10 mm, SOD_b = -60 mm, τ_b = 118.2 Pa.

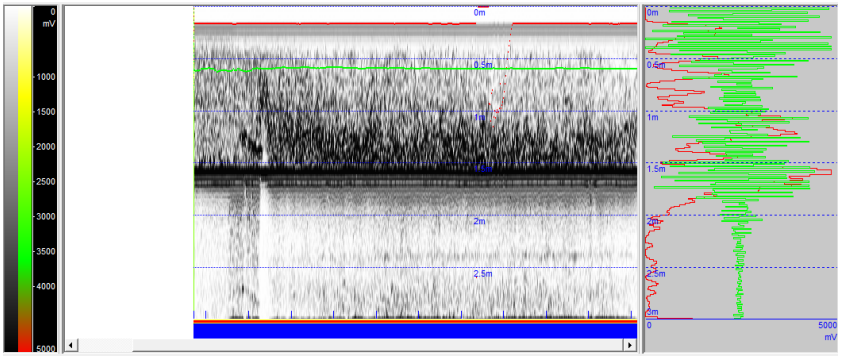

Figure E.6: Test 1: echo sounding profile made during the execution of run 3. v_t = 0.25 m/s, D_n = 35 mm, p_j = 0.53 bar, SOD_r = 50 mm, SOD_b = 10 mm, τ_b = 118.2 Pa.

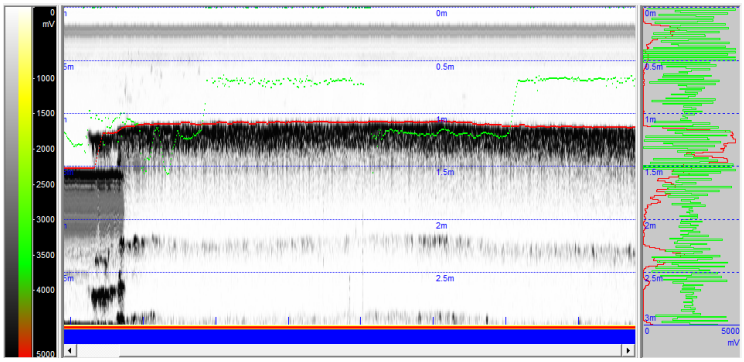

Figure E.7: Test 2: echo sounding profile made before the execution of run 1. v_t = 0.40 m/s, D_n = 35 mm, p_j = 0.51 bar, SOD_r = 70 mm, SOD_b = 70 mm, τ_b = 80.15 Pa.

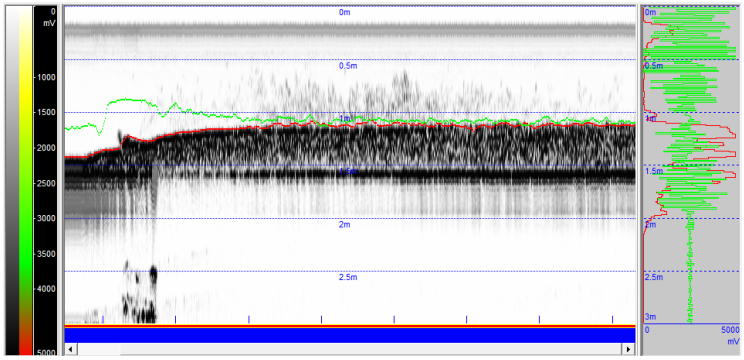

Figure E.8: Test 2: echo sounding profile made before the execution of run 2. v_t = 0.40 m/s, D_n = 35 mm, p_j = 0.50 bar, SOD_r = 70 mm, SOD_b = 140 mm, τ_b = 80.15 Pa.

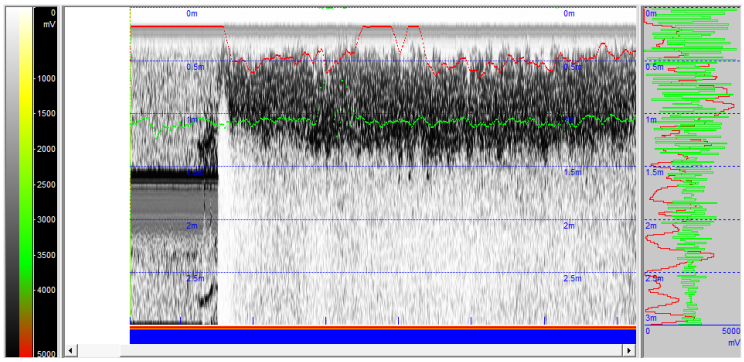

Figure E.9: Test 2: echo sounding profile made during the execution of run 1. v_t = 0.40 m/s, D_n = 35 mm, p_j = 0.51 bar, SOD_r = 70 mm, SOD_b = 70 mm, τ_b = 80.15 Pa.

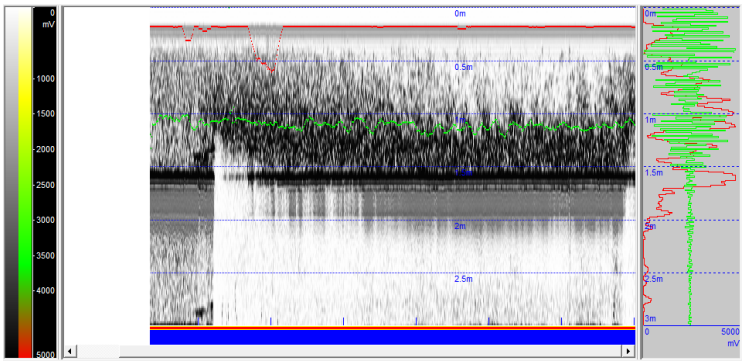

Figure E.10: Test 2: echo sounding profile made during the execution of run 2. v_t = 0.40 m/s, D_n = 35 mm, p_j = 0.50 bar, SOD_r = 70 mm, SOD_b = 140 mm, τ_b = 80.15 Pa.

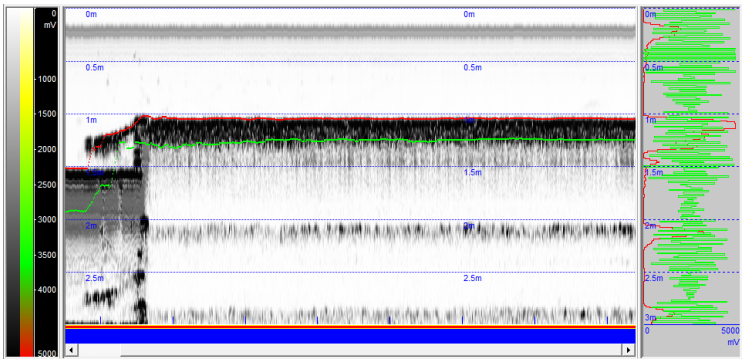

Figure E.11: Test 3: echo sounding profile made before the execution of run 1. v_t = 0.40 m/s, D_n = 20 mm, p_j = 1.06 bar, SOD_r = 10 mm, SOD_b = -10 mm, τ_b = 156 Pa.

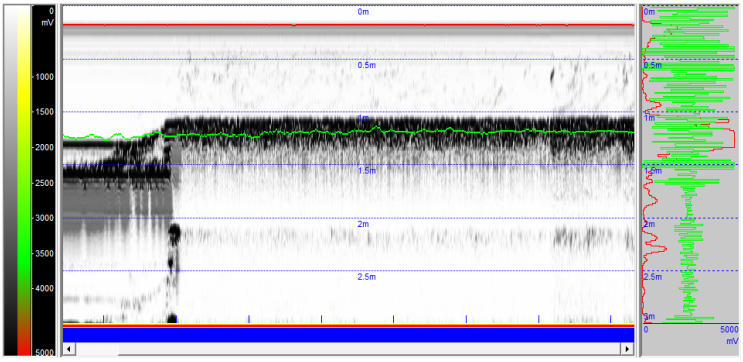

Figure E.12: Test 3: echo sounding profile made before the execution of run 2. v_t = 0.40 m/s, D_n = 20 mm, p_j = 1.05 bar, SOD_r = 10 mm, SOD_b = 0 mm, τ_b = 156 Pa.

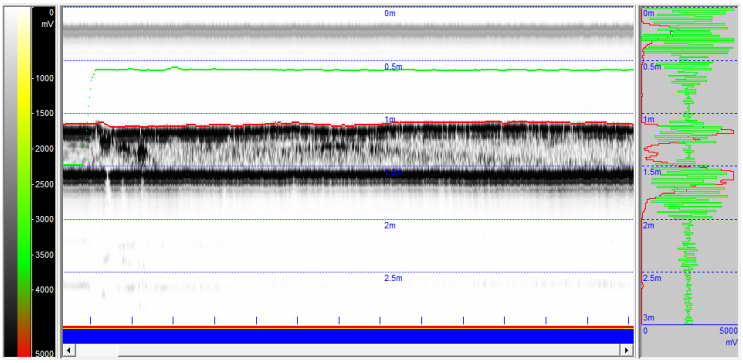

Figure E.13: Test 3: echo sounding profile made before the execution of run 3. v_t = 0.40 m/s, D_n = 20 mm, p_j = 1.03 bar, SOD_r = 10 mm, SOD_b = -30 mm, τ_b = 156 Pa.

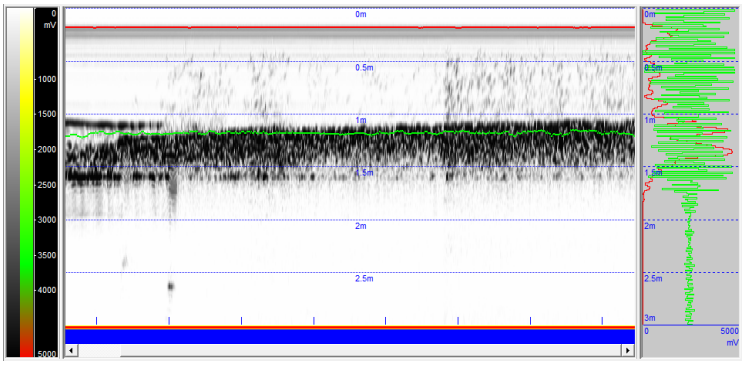

Figure E.14: Test 3: echo sounding profile made before the execution of run 4. v_t = 0.40 m/s, D_n = 20 mm, p_j = 1.02 bar, SOD_r = 60 mm, SOD_b = 60 mm, τ_b = 156 Pa.

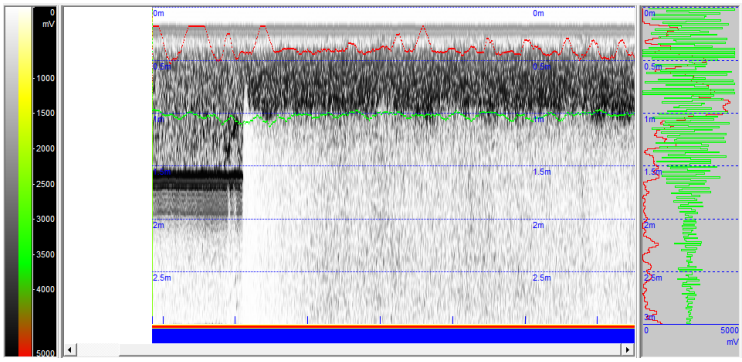

Figure E.15: Test 3: echo sounding profile made during the execution of run 1. v_t = 0.40 m/s, D_n = 20 mm, p_j = 1.06 bar, SOD_r = 10 mm, SOD_b = -10 mm, τ_b = 156 Pa.

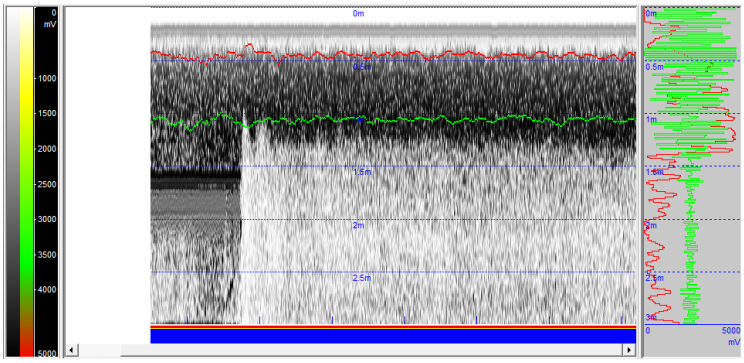

Figure E.16: Test 3: echo sounding profile made during the execution of run 2. v_t = 0.40 m/s, D_n = 20 mm, p_j = 1.05 bar, SOD_r = 10 mm, SOD_b = 0 mm, τ_b = 156 Pa.

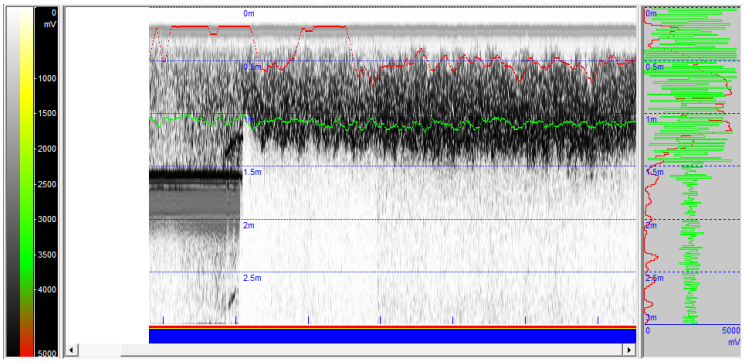

Figure E.17: Test 3: echo sounding profile made during the execution of run 3. v_t = 0.40 m/s, D_n = 20 mm, p_j = 1.03 bar, SOD_r = 10 mm, SOD_b = -30 mm, τ_b = 156 Pa.

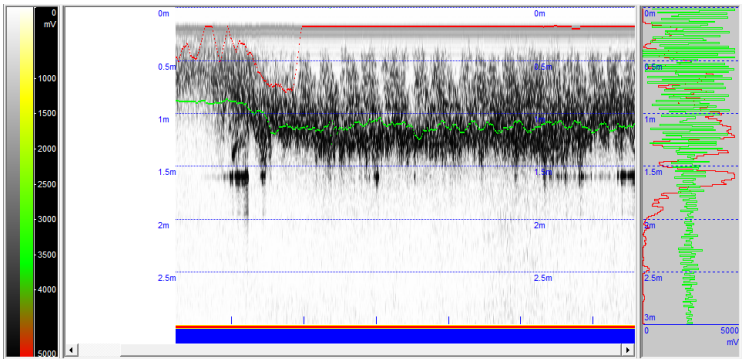

Figure E.18: Test 3: echo sounding profile made during the execution of run 4. v_t = 0.40 m/s, D_n = 20 mm, p_j = 1.02 bar, SOD_r = 60 mm, SOD_b = 60 mm, τ_b = 156 Pa.

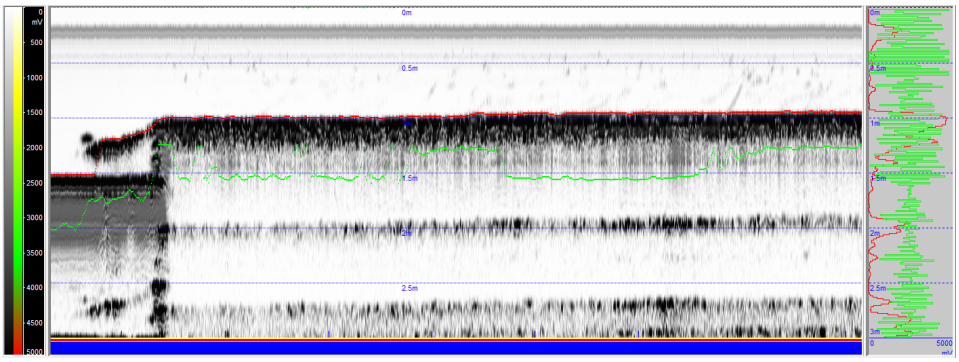

Figure E.19: Test 4: echo sounding profile made before the execution of run 1. v_t = 0.25 m/s, D_n = 20 mm, p_j = 1.02 bar, SOD_r = 10 mm, SOD_b = -60 mm, τ_b = 237.2 Pa.

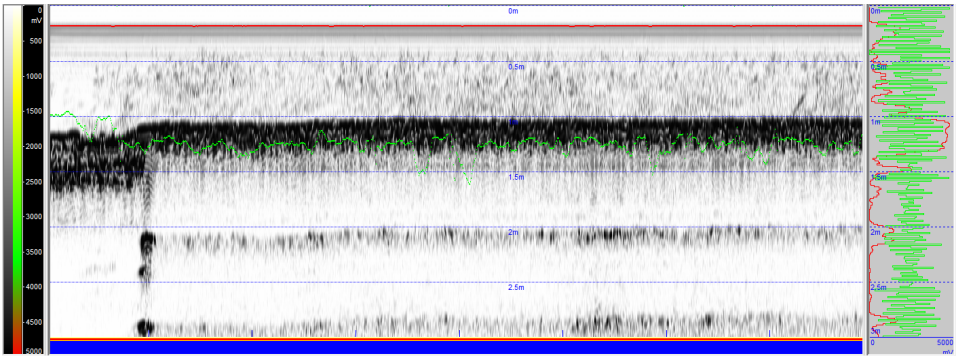

Figure E.20: Test 4: echo sounding profile made before the execution of run 2. v_t = 0.25 m/s, D_n = 20 mm, p_j = 1.04 bar, SOD_r = 10 mm, SOD_b = -50 mm, τ_b = 237.2 Pa.

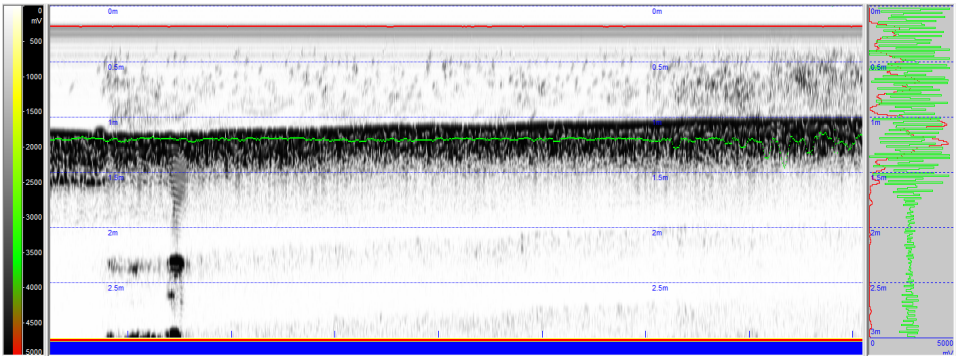

Figure E.21: Test 4: echo sounding profile made before the execution of run 3. v_t = 0.25 m/s, D_n = 20 mm, p_j = 1.02 bar, SOD_r = 10 mm, SOD_b = 20 mm, τ_b = 237.2 Pa.

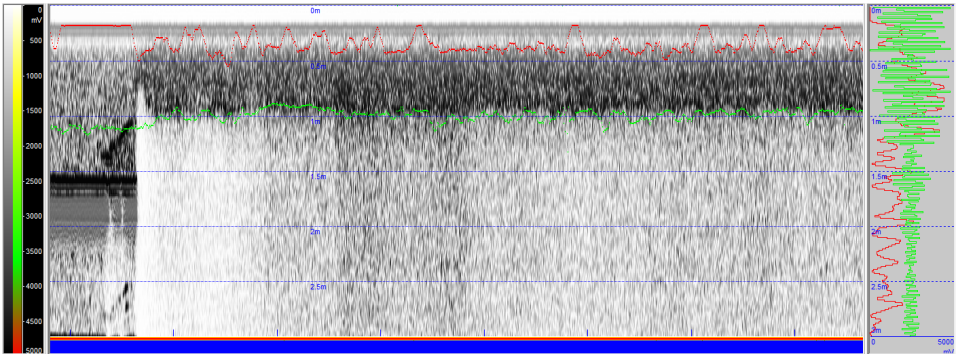

Figure E.22: Test 4: echo sounding profile made during the execution of run 1. v_t = 0.25 m/s, D_n = 20 mm, p_j = 1.02 bar, SOD_r = 10 mm, SOD_b = -60 mm, τ_b = 237.2 Pa.

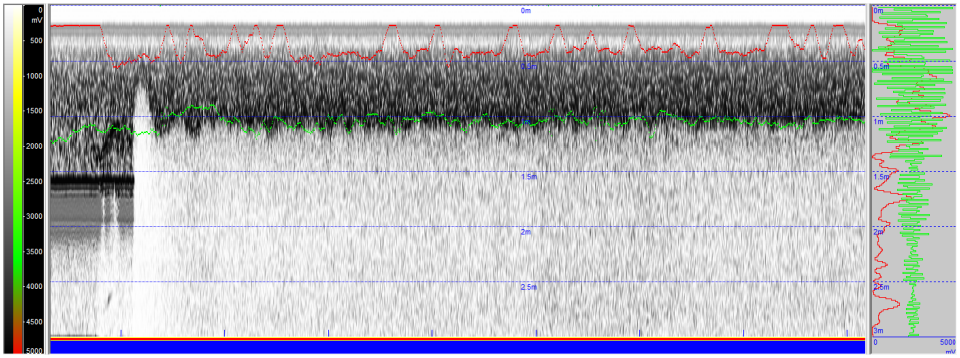

Figure E.23: Test 4: echo sounding profile made during the execution of run 2. v_t = 0.25 m/s, D_n = 20 mm, p_j = 1.04 bar, SOD_r = 10 mm, SOD_b = -50 mm, τ_b = 237.2 Pa.

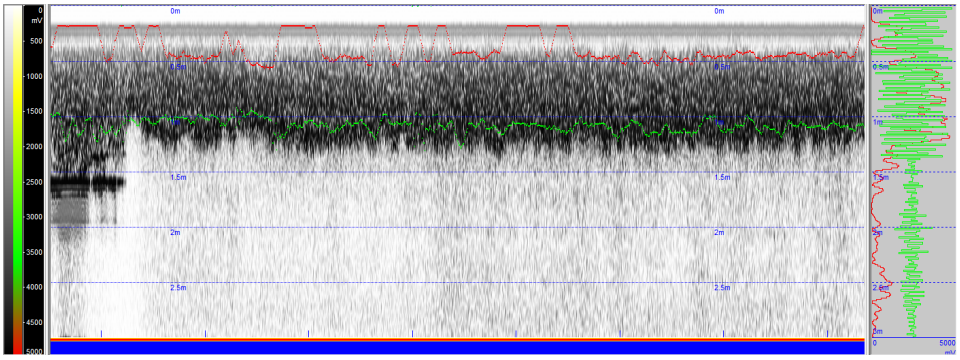

Figure E.24: Test 4: echo sounding profile made during the execution of run 3. v_t = 0.25 m/s, D_n = 20 mm, p_j = 1.02 bar, SOD_r = 10 mm, SOD_b = 20 mm, τ_b = 237.2 Pa.

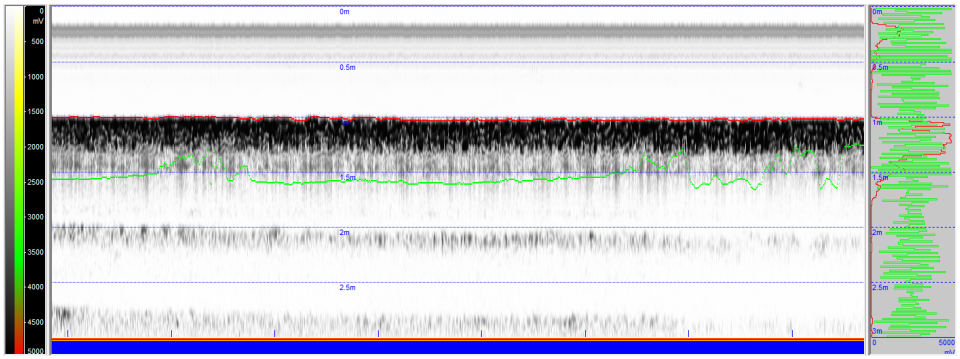

Figure E.25: Test 5: echo sounding profile made before the execution of run 1. v_t = 0.25 m/s, D_n = 20 mm, p_j = 0.50 bar, SOD_r = 10 mm, SOD_b = -10 mm, τ_b = 132.7 Pa.

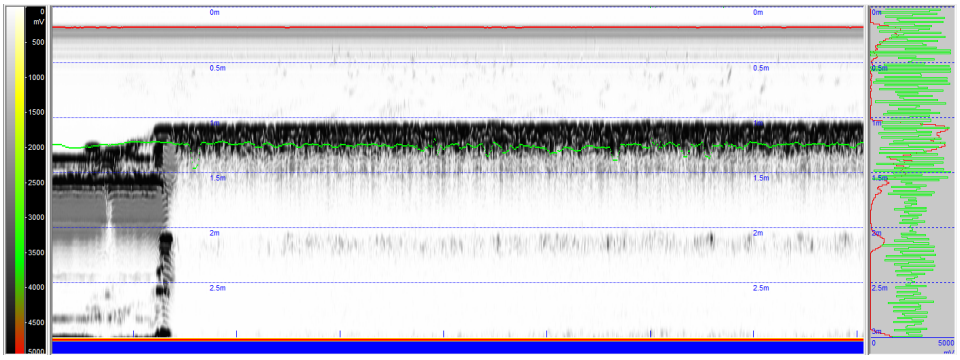

Figure E.26: Test 5: echo sounding profile made before the execution of run 2. v_t = 0.25 m/s, D_n = 20 mm, p_j = 0.51 bar, SOD_r = 10 mm, SOD_b = -20 mm, τ_b = 132.7 Pa.

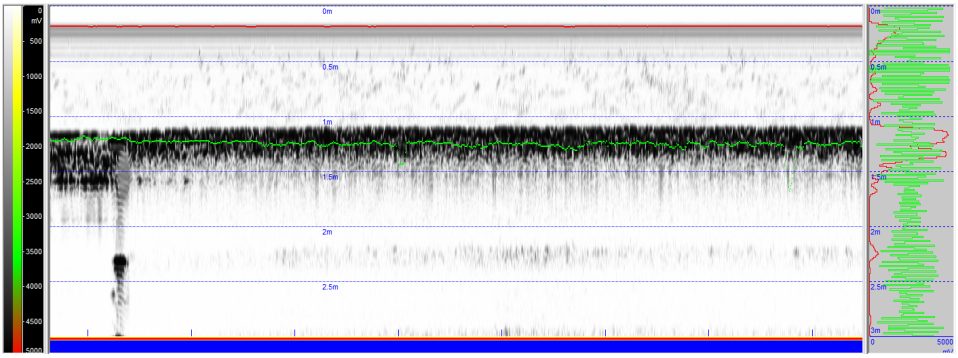

Figure E.27: Test 5: echo sounding profile made before the execution of run 3. v_t = 0.25 m/s, D_n = 20 mm, p_j = 0.51 bar, SOD_r = 10 mm, SOD_b = -50 mm, τ_b = 132.7 Pa.

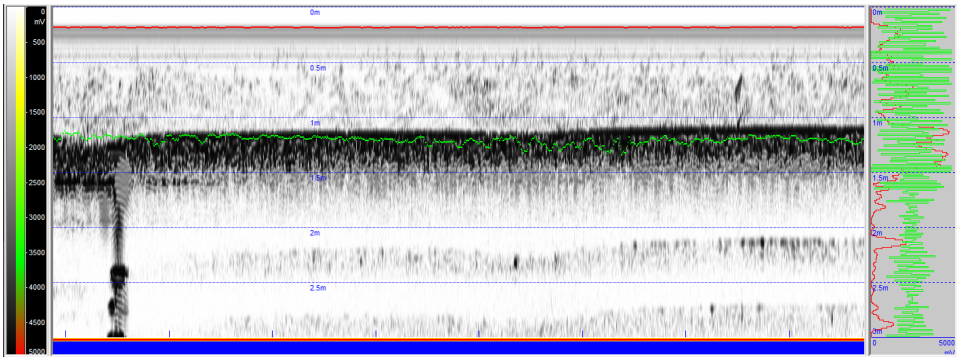

Figure E.28: Test 5: echo sounding profile made before the execution of run 4. v_t = 0.25 m/s, D_n = 20 mm, p_j = 0.50 bar, SOD_r = 60 mm, SOD_b = 10 mm, τ_b = 132.7 Pa.

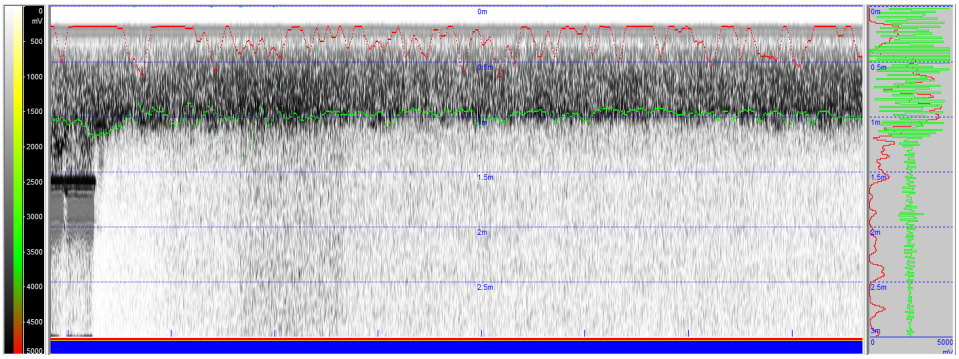

Figure E.29: Test 5: echo sounding profile made during the execution of run 1. v_t = 0.25 m/s, D_n = 20 mm, p_j = 0.50 bar, SOD_r = 10 mm, SOD_b = -10 mm, τ_b = 132.7 Pa.

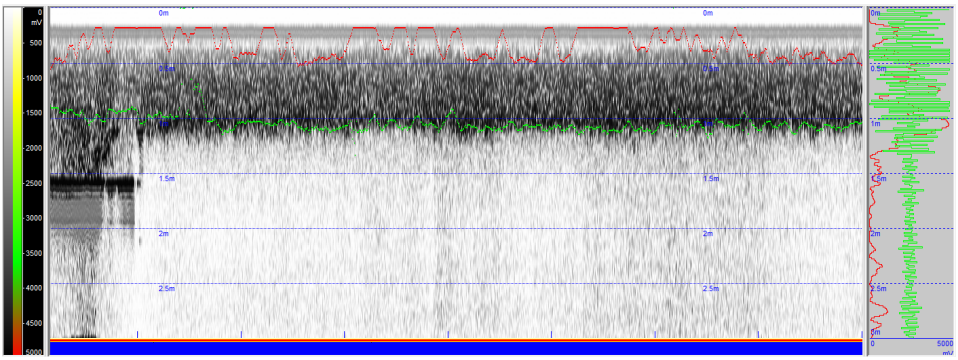

Figure E.30: Test 5: echo sounding profile made during the execution of run 2. v_t = 0.25 m/s, D_n = 20 mm, p_j = 0.51 bar, SOD_r = 10 mm, SOD_b = -20 mm, τ_b = 132.7 Pa.

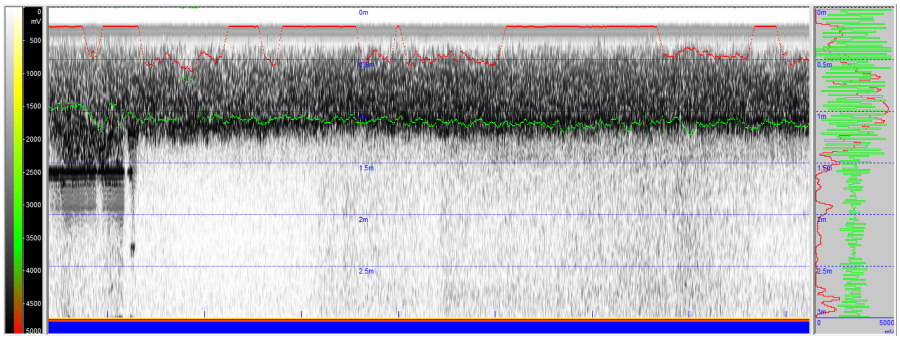

Figure E.31: Test 5: echo sounding profile made during the execution of run 3. v_t = 0.25 m/s, D_n = 20 mm, p_j = 0.51 bar, SOD_r = 10 mm, SOD_b = -50 mm, τ_b = 132.7 Pa.

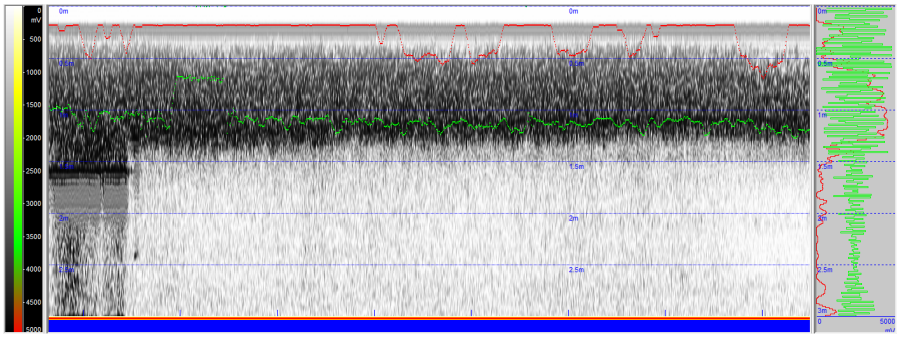

Figure E.32: Test 5: echo sounding profile made during the execution of run 4. v_t = 0.25 m/s, D_n = 20 mm, p_j = 0.50 bar, SOD_r = 60 mm, SOD_b = 10 mm, τ_b = 132.7 Pa.

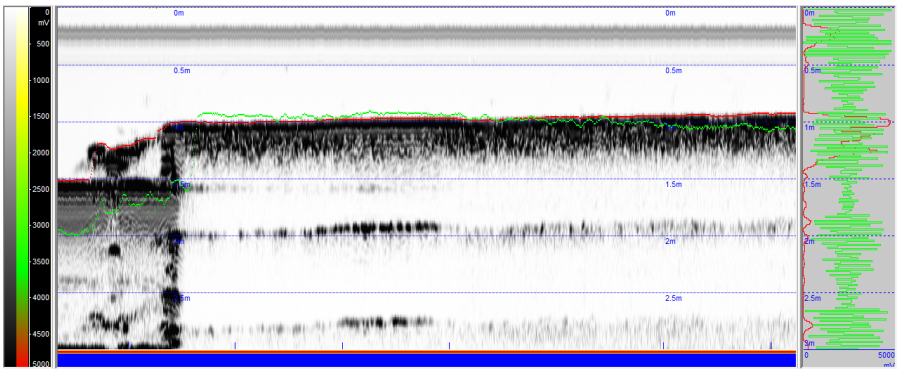

Figure E.33: Test 6: echo sounding profile made before the execution of run 1. v_t = 0.40 m/s, D_n = 20 mm, p_j = 1.00 bar, SOD_r = 300 mm, SOD_b = 220 mm, τ_b = 112.2 Pa.

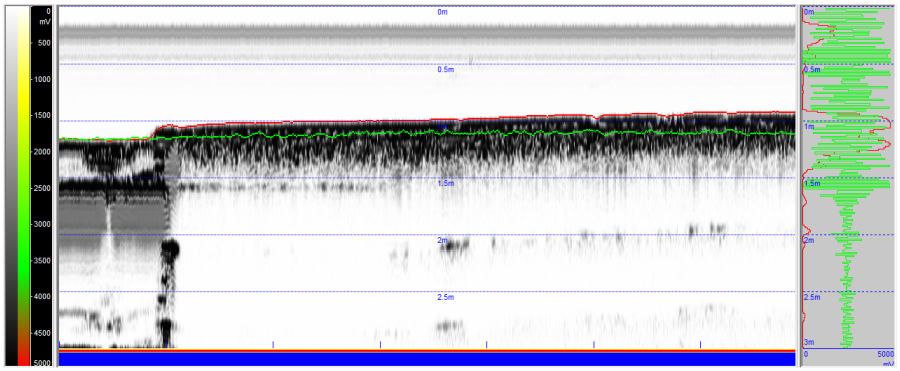

Figure E.34: Test 6: echo sounding profile made before the execution of run 2. v_t = 0.40 m/s, D_n = 20 mm, p_j = 1.06 bar, SOD_r = 300 mm, SOD_b = 230 mm, τ_b = 112.2 Pa.

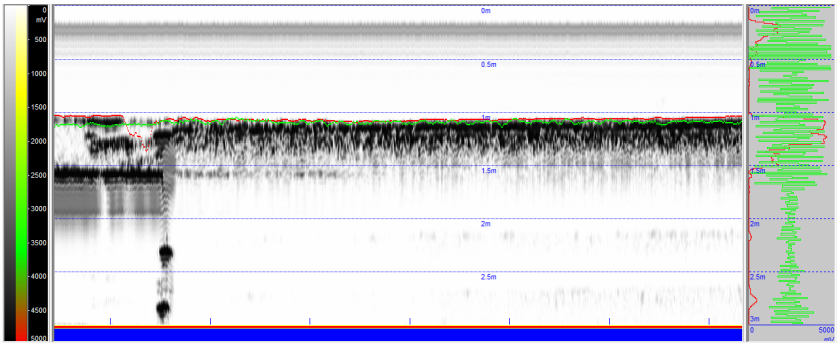

Figure E.35: Test 6: echo sounding profile made before the execution of run 3. v_t = 0.40 m/s, D_n = 20 mm, p_j = 1.06 bar, SOD_r = 60 mm, SOD_b = -40 mm, τ_b = 112.2 Pa.

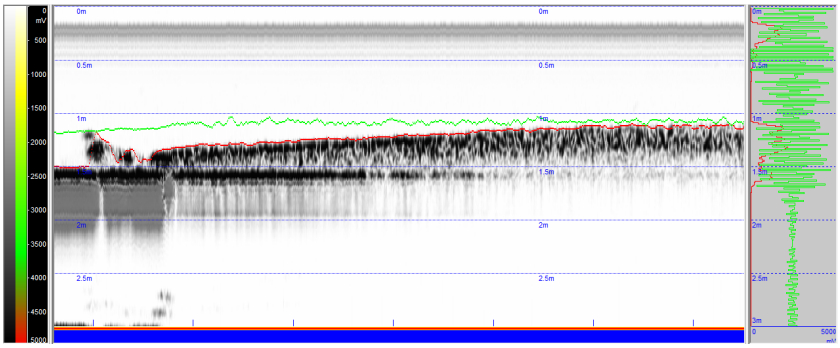

Figure E.36: Test 6: echo sounding profile made before the execution of run 4. v_t = 0.40 m/s, D_n = 20 mm, p_j = 1.04 bar, SOD_r = 300 mm, SOD_b = 260 mm, τ_b = 112.2 Pa.

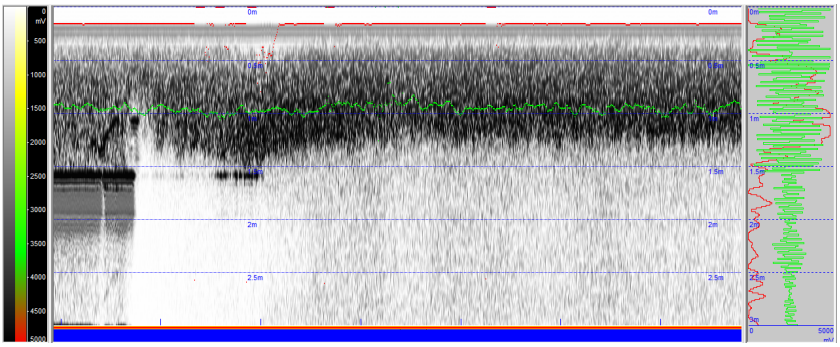

Figure E.37: Test 6: echo sounding profile made during the execution of run 1. v_t = 0.40 m/s, D_n = 20 mm, p_j = 1.00 bar, SOD_r = 300 mm, SOD_b = 220 mm, τ_b = 112.2 Pa.

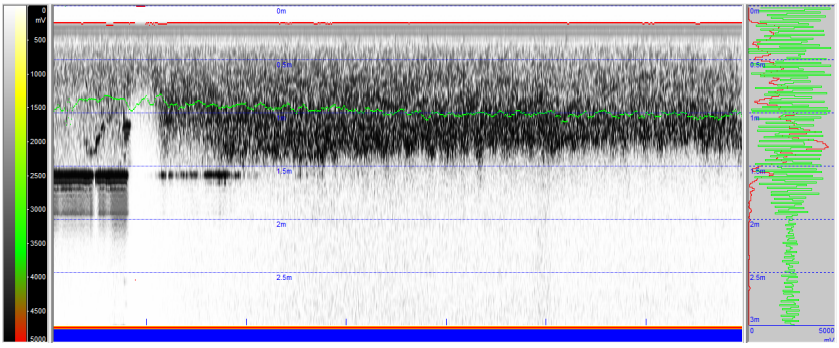

Figure E.38: Test 6: echo sounding profile made during the execution of run 2. v_t = 0.40 m/s, D_n = 20 mm, p_j = 1.06 bar, SOD_r = 300 mm, SOD_b = 230 mm, τ_b = 112.2 Pa.

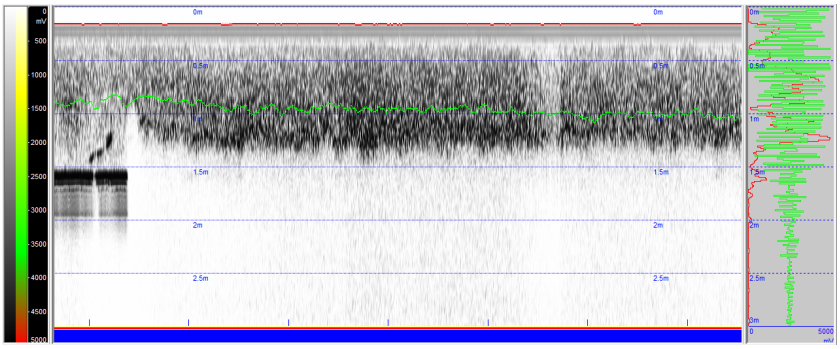

Figure E.39: Test 6: echo sounding profile made during the execution of run 3. v_t = 0.40 m/s, D_n = 20 mm, p_j = 1.06 bar, SOD_r = 60 mm, SOD_b = -40 mm, τ_b = 112.2 Pa.

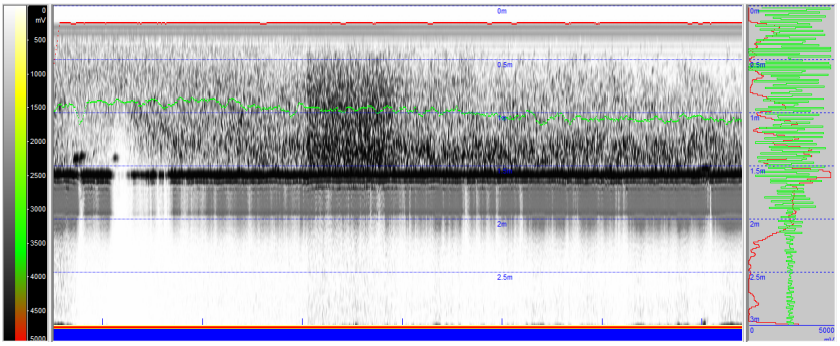

Figure E.40: Test 6: echo sounding profile made during the execution of run 4. v_t = 0.40 m/s, D_n = 20 mm, p_j = 1.04 bar, SOD_r = 300 mm, SOD_b = 260 mm, τ_b = 112.2 Pa.